Exhaust aftertreatment modeling for efficient calibration in diesel passenger car applications

Original
Exhaust aftertreatment modeling for efficient calibration in diesel passenger car applications / Rafigh, Mahsa. - (2017).

Publisher:
Politecnico di Torino

Published
DOI:10.6092/polito/porto/2675368

Doctoral Dissertation
Doctoral Program in Energy Engineering (29th Cycle)

Exhaust Aftertreatment Modeling for Efficient Calibration in Diesel Passenger Car Applications

By

Mahsa Rafigh

******

Supervisor(s):
Professor Federico Millo

Doctoral Examination Committee:
Professor Angelo Onorati, Referee, Politecnico di Milano, Italy
Professor Zissis Samaras, Referee, Aristotle University, Thessaloniki, Greece

Politecnico di Torino
2017

Declaration

I hereby declare that, the contents and organization of this dissertation constitute my own original work and does not compromise in any way the rights of third parties, including those relating to the security of personal data.

Mahsa Rafigh

2017

* This dissertation is presented in partial fulfillment of the requirements for **Ph.D. degree** in the Graduate School of Politecnico di Torino (ScuDo).

I would like to dedicate this thesis to my loving parents

Acknowledgment

This thesis would not have been possible without the inspiration and support of a number of wonderful individuals: my thanks and appreciation to all of them for being part of this journey and making this thesis possible.

I owe my deepest gratitude to my dear supervisor Professor Federico Millo. Without his enthusiasm, encouragement, support and continuous optimism this thesis would hardly have been completed.

I express my warmest gratitude to my PhD scholarship sponsor, “GM Global Propulsion Systems – Torino S.r.l.”, specially Eng Ken Friis Hansen, Eng. Paolo Ferreri, Dr. Euardo Barrientos, Eng. Emilie Reynier, Dr. Francesco Pesce, Eng. Marcello Rimondi and Eng. Isadora Ricci, who guided me with their experience

My gratitude is also extended to “Gamma Technologies LLC, IL, USA” aftertreatment group members for sharing their valuable expertise, knowledge and support that has immensely influenced this research. Heartfelt thanks goes to Dr Syed Wahiduzzaman, my supervisor at Gamma Technologies, for his intellectual guidance and patient motivation. In addition, I would like to thank my friends at Gamma Technologies Inc., Ryan Dudgeon, Jonathan Brown, Dominik Artukovic and Santhosh Gundlapally, for kindly providing frequent support, step-by-step guidance and resources.

I would like to show my appreciation to Dr Dick Blint from “N2Kinetics Research, MI, USA” for providing valuable feedback and suggestions throughout this research.

I would also like specially acknowledge Eng. Josh Pihl at “Oak Ridge National Laboratory, TN, USA”, Eng. Peter Dittman at “ACA – Center for Automotive Catalytic Systems, RWTH Aachen University, Germany” and Professor Debora Fino at “Chemical Department of Politecnico di Torino” for making it possible to carry out this work based on their knowledge in experimental activities and providing experimental data.

I am also thankful to my colleagues: Andrea Piano, Sabino Caputto, Giulio Boccardo, Alessandro Zanelli, Claudio Cubito, Francesco Sapio, Luciano Rolando, Daniele Porcu, Pranav Arya and Giuseppe Di Pierro at “e3 - Engines, Energy and Environment laboratory at Politecnico di Torino” for their friendship and support, and for creating a cordial working environment.

Finally, my deep and sincere gratitude to my family for their continuous and unparalleled love and support and for educating me with aspects from both arts and sciences, for unconditional support and encouragement to pursue my interests, even when the interests went beyond boundaries of language, field and geography. I am forever indebted to my dad and mom for giving me the opportunities and experiences that have made me who I am. They selflessly encouraged me to explore new directions in life and seek my own destiny. I am grateful to my sister and my brother for always being there for me as a friend. Last, but certainly not least, huge thanks and appreciation go to Mohsen who has been by my side throughout last years, living every single minute of it, being a constant source of strength and inspiration during difficulties and happiness. Through his patience, help and unwavering belief in me, I have been able to complete this long dissertation journey.

This journey would not have been possible without their warm love, continued patience, and endless support, and I dedicate this milestone to them.

Publications

Parte del lavoro descritto in questa tesi è stato anche preventivamente pubblicato in:

Part of the work described in this thesis was also previously published in the following publications:

1. F. Millo, M. Rafigh, M. Andreata, T. Vlachos, P. Arya, P. Miceli, Impact of high sulfur fuel and de-sulfation process on a close-coupled diesel oxidation catalyst and diesel particulate filter, Fuel. (2017) 1–10. doi:10.1016/j.fuel.2017.01.006.

2. F. Millo, M. Rafigh, S. Wahiduzzaman, R. Dudgeon, Calibration of a Global Kinetic Mechanism Based on Synthetic Gas Bench Experiments for a Lean NOx Trap Catalyst for Automotive Applications, THIESEL Conf. Thermo-Fluid Dyn. Process. Direct Inject. Engines. (2016).

3. F. Millo, M. Rafigh, D. Fino, P. Miceli, Application of a global kinetic model on an SCR coated on Filter (SCR-F) catalyst for automotive applications, Fuel. (2016). doi:10.1016/j.fuel.2016.11.082.

4. M. Rafigh, R. Dudgeon, J. Pihl, S. Daw, R. Blint, S. Wahiduzzaman, Development of a Global Kinetic Model for a Commercial Lean NOx Trap Automotive Catalyst Based on Laboratory Measurements, Emiss. Control Sci. Technol. (2016). doi:10.1007/s40825-016-0049-8.

5. Millo, F., Rafigh, M., "Modelling of Aftertreatment Devices for NOx Emissions Control in Diesel Engines", After-treatment systems for diesel engines, SAENA Workshop, June 2016.

6. F. Millo, M. Andreata, M. Rafigh, D. Mercuri, C. Pozzi, Impact on vehicle fuel economy of the soot loading on diesel particulate filters made of different substrate materials, Energy. 86 (2015) 19–30. doi:10.1016/j.energy.2015.03.076.

Abstract

Interest in utilizing advanced lean-burn gasoline and diesel engines has increased in the last decades due to their reduced greenhouse gas emissions and increased fuel economy. One impediment to the increasing use of these engines, however, is the need to develop corresponding catalytic systems for controlling pollutant emissions. In particular, although still far from the fuel neutral United States (US) approach, European (EU) legislation limits for Nitrogen Oxides (NO_x) emissions are becoming more and more severe and also type approval procedures are going to radically change with the introduction of Worldwide harmonized Light vehicles Test Cycle (WLTC) and Real Driving Emission (RDE) tests. Considering that test bench and chassis dyno experimental campaigns are costly and require a vast use of resources for the generation of data; therefore, reliable and computationally efficient simulation models are essential in order to identify the most promising technology mix to satisfy emission regulations and fully exploit advantages of diesel and lean-burn gasoline when minimizing the side effect of their emissions. Therefore, the aim of this work is to develop reliable models of the individual aftertreatment components and to calibrate the kinetic parameters based on experimental measurements which can be further used as a virtual test rig to evaluate the effectiveness of each technology in terms of reducing pollutant emissions.

In the current work, a brief introduction regarding the passenger car emissions, regulations and control technologies, including in-cylinder control techniques and aftertreatment systems, is provided in Chapter 1. In addition, simulation modelling approaches for aftertreatment applications are discussed. More details about specific aftertreatment components are discussed in the next chapters. As an example, the modeling of a Selective Catalytic Reduction coated on Filter (SCR-F), on the basis of Synthetic Gas Bench (SGB) reactor data is presented in Chapter 2; focusing, in particular, on estimation of ammonia storage capacity, NO_x conversion and soot reduction due to passive regeneration. LNT is analyzed in Chapter 3, focusing on the reactor-scale Synthetic Gas Bench (SGB) experiments and calibration of the 1D simulation model for two case studies with the aim to characterize Oxygen Storage Capacity (OSC), NO_x Storage and Reduction (NSR) and light-off. The calibrated 1D simulation model is thereafter validated, in Chapter 4, for one of the case studies using engine-out emissions, mass flowrate and temperature traces over Worldwide harmonized Light vehicles Test Cycle (WLTC) as the boundary condition for the inlet of LNT for full-size component. Afterwards, the LNT model calibrated in Chapter 3 is, in Chapter 5, further reduced and linearized with reasonable assumptions to be used as a plant-model with very low computational requirement and in real time applications such as Electronic Control Unit (ECU)/ Hardware-in-the-Loop (HiL) systems. Finally, after discussing NO_x control systems in previous chapters, modeling of Diesel Oxidation Catalyst (DOC), which plays a fundamental role not only for the CO and HC conversion, but also for promoting the oxidation of NO into NO_2, is discussed in Chapter 6.

It is worth noting that depending on the complexity of the kinetic model, different optimization tools are implemented for the calibration; as an example, Brent method is used for calibration of SCR-F kinetic model, likewise, Genetic Algorithm (GA) is used for the calibration of the DOC kinetic parameters; however, for more complex kinetic schemes like LNT both manual and automatic optimization is required to evaluate the most suitable reaction pathways and kinetic parameters.

Accordingly, after development of the kinetic model for each aftertreatment component and validation of the full-scale model, further investigations could be

devoted to combining the models in order to simulate the whole aftertreatment system and assess the performance over different driving cycles.

Contents

List of Figures

List of Tables

Abbreviations

CFD	Computational Fluid Dynamics
CLD	Chemi-Luminescence Detector
CPU	Central Processing Unit
cpsi	cells per square inch
DOC	Diesel Oxidation Catalyst
DoE	Design of Experiments
DPF	Diesel Particulate Filter
ECU	Electronic Control Unit
EGR	Exhaust Gas Recirculation
FTIR	Fourier Transform Infrared
GA	Genetic Algorithm
HC	Hydrocarbon
HiL	Hardware-in-the-Loop
LNT	Lean NO_x Trap
NEDC	New European Driving Cycle
NMHC	Non-Methane Hydrocarbon
NO_x	Nitrogen Oxides
NSC	NO_x Storage Catalyst
NSR	NO_x Storage and Reduction

ODE	Ordinary Differential Equation
ORNL	Oak Ridge National Lab
OSC	Oxygen Storage Capacity
PDE	Partial Differential Equation
PGM	Platinum Group Metals
PM	Particulate Matter
RDE	Real Driving Emission
SGB	Synthetic Gas Bench
SCR	Selective Catalytic Reduction
SCR-F	Selective Catalytic Reduction coated on Filter
SR	Steam Reforming
TPD	Temperature Programmed Desorption
TPR	Temperature Programmed Reduction
TWC	Three Way Catalyst
WGS	Water Gas Shift
WLTC	Worldwide harmonized Light vehicles Test Cycle
XRF	X-Ray Fluorescence

Symbols

α_i^T	Stoichiometric coefficient vector of species *i*
$\alpha_{\theta_k}^T$	Stoichiometric coefficient vector of site *k*
ΔG	Change in Gibbs free energy
ΔH_j	Enthalpy of reaction *j* [J/mole]
Δt	Time step [s]
δ_c	Effective thickness of washcoat [m]
δ_w	Effective thickness of wall [m]
ε	Void fraction of the reactor
Θ_i	Active site expression for reaction *i*
θ^{eq}	Equilibrium coverage
θ_k	Coverage of site *k*
λ_f	Thermal conductivity of the bulk gas [W/(m.K)]
λ_w	Thermal conductivity of the wall [W/(m.K)]
ρ_f	Gas phase density [kg/m3]
ρ_f	Wall density [kg/m3]
$\Psi_{NO_x}^{cap}$	NO_x storage capacity
A_i	Pre-exponent multiplier of Arrhenius function for reaction i
C_0	Total molar concentration [mole/m3]

C_i	Concentration of species i [mole/m3]
$C_{meas,i}$	Concentration of species i from measurement [mole/m3]
C_s	Active site density per reactor volume [moleactive site/m3]
$C_{sim,i}$	Concentration of species i from simulation [mole/m3]
C_{pf}	Heat capacity of fluid (gas) [J/(kg.K)]
C_{pw}	Heat capacity of wall [J/(kg.K)]
D_h	Hydraulic diameter of the channel [m]
D_s	Effective diffusivity of a species in washcoat [m2/s]
dx	Sub-volumes length [m]
$E_{a,i}$	Activation energy of Arrhenius function for reaction i [J/mole]
F_{obj}	Objective function
G	Inhibition term
h	Convection heat transfer coefficient [W/(m2.K)]
I_i	Inhibition function for reaction i
f	Friction factor
$K_{eq,NO}$	Equilibrium constant of NO oxidation reaction
$K_{eq,WGS}$	Equilibrium constant of water gas shift reaction
k_i	Kinetic constant of reaction i
k_{me}	External mass transfer coefficient [m/s]
Mw	Molecular mass [g/mole]
Nu	Nusselt number

$n_{i,stored}$	Number of stored moles of species i [mole]
$\dot{n}_{i,in}$	Inlet molar flow rate of species i [mole]
$\dot{n}_{i,out}$	Outlet molar flow rate of species i [mole]
p	Pressure [Pa]
Pe	Peclet number
R	Universal gas constant [J/(mole.K)]
R_{Ω}	One fourth of the channel hydraulic diameter [m]
r_j	Reaction rate of reaction j or species j [mole/(m3.s)]
S	Surface area per reactor volume [1/m]
Sh	Sherwood number
T_f	Fluid (gas) phase temperature [K]
T_S	Solid phase temperature [K]
t	Time [s]
u	Velocity [m/s]
w	Weighting factor
X_{fm}	Species mole fraction vector in the bulk gas [mole/(mole$_{tot}$.m^3)]
X_{wc}	Species mole fraction vector in the washcoat [mole/(mole$_{tot}$.m^3)]
x	Axial position [m]
y	Length co-ordinate along washcoat direction

Parte del lavoro descritto in questo capitolo è stato anche preventivamente pubblicato in:

Part of the work described in this chapter was also previously published in the following publications:

1. M. Rafigh, R. Dudgeon, J. Pihl, S. Daw, R. Blint, S. Wahiduzzaman, Development of a Global Kinetic Model for a Commercial Lean NOx Trap Automotive Catalyst Based on Laboratory Measurements, Emiss. Control Sci. Technol. (2016). doi:10.1007/s40825-016-0049-8.

Chapter 1

Introduction

1.1 Passenger car emissions and control technologies

Diesel engines utilization in passenger car applications is beneficial thanks to lower greenhouse gas emissions and improved fuel economy; however, controlling the pollutant emissions including CO, HC, Nitrogen Oxides (NO_x) and Particulate Matter (PM) becomes more challenging with the upcoming stringent emission regulations. Therefore, advanced aftertreatment technologies and in-cylinder control strategies, such as Exhaust Gas Recirculation (EGR) for NO_x control, are necessary in order to reduce the emissions below the limit defined by regulations [1,2].

Moreover, type approval procedures are going to radically change with the introduction of Worldwide harmonized Light vehicles Test Cycle (WLTC) and Real Driving Emission (RDE) tests, expanding the emission relevant area to higher loads and speeds, as shown Figure 1.

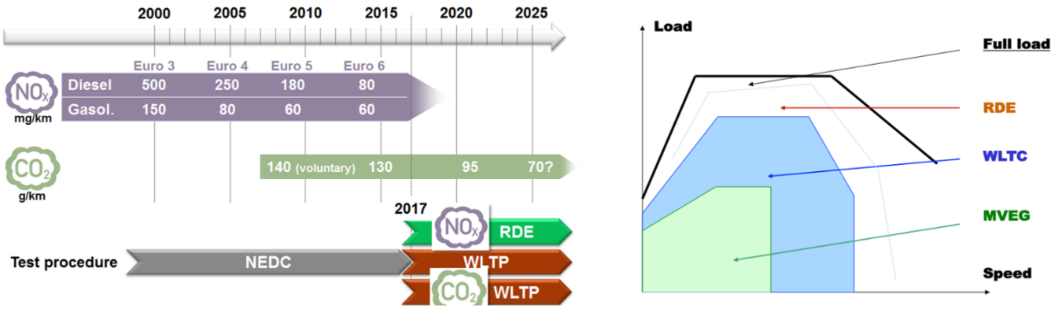

Figure 1. Emission Regulations and type-approval procedures [3]

More in detail, differently from conventional gasoline engines, the emissions of which are controlled by means of Three Way Catalysts (TWC), the lean environment requires more complex and advanced aftertreatment systems in order to clean diesel and lean-burn gasoline engines' exhaust. In particular, the main aftertreatment components which are generally used for emission control of diesel engines can be listed as follows:

- **Diesel Oxidation Catalyst (DOC):** consists of Platinum Group Metals (PGM) to reduce CO and HC emissions [4] and to convert NO to NO_2, which is beneficial for downstream aftertreatment components [5]. DOC can also contain trapping materials, as zeolites, which can trap HC at low temperature, to subsequently release them after the light-off temperature has been reached in order to improve cold start HC reduction efficiency [6–8].
- **Diesel Particulate Filter (DPF):** used for the trapping of PM. It is worth noting that PM accumulated on the filter needs to be periodically removed by means of regeneration events to recover the filtering capacity of the DPF [9–11].
- **Selective Catalytic Reduction (SCR):** used for NO_x emission reduction via NH_3 through SCR reactions over a wide temperature range. Ammonia is provided to the system through urea injection into the exhaust line before catalyst entrance [5,12], for active systems. Although, in passive SCR systems NH_3 produced as a by-product in upstream aftertreatment systems, such as LNT, is used for NOx reduction in passive SCR [13].
- **Lean NO_x Trap (LNT):** used for NO_x emission control through periodic NO_x adsorption and reduction which operate on the principle of lean/rich cyclic processes [14–16]. The adsorption/desorption of NO_x on the trapping component, for instance BaO, during the lean phase results in the formation of nitrates and nitrites on the catalyst surface. When the active trapping sites are saturated, a short rich phase is started by injecting a reducing agent such as H_2, CO, or HC, by means of fuel post-injection.

It is worth mentioning that in order to comply with existing and future emission regulations combinations of the abovementioned components can be implemented such as using LNT upstream of an SCR coated on Filter (SCR-F), used for NO_x and PM reduction simultaneously [13,17,18]. Some aftertreatment architecture examples are depicted in Figure 2.

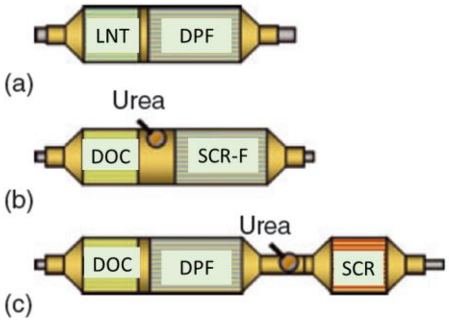

Figure 2. a) Coupled LNT and DPF; b) coupled DOC and SCR-F; c) Coupled DOC, DPF and SCR [19]

1.2 Simulation approaches for modelling and calibration of aftertreatment systems

Advanced engine and aftertreatment technologies in new generation automotive applications have been developed with the aim of improvements in terms of fuel economy and minimizing pollutant emissions. As a result, the attraction towards using computationally efficient and at the same time reliable simulation tools in automotive applications has been increasing over the last decades. Such models, when calibrated, can be exploited for design and optimization purposes, control strategies and sensitivity analysis of different parameters providing benefits in terms of cost.

1.2.1 Simulation model assumptions

In particular, automotive application modelling approaches can be classified in three main groups depending on the level of complexity of the system in terms of kinetic, heat transfer and flow models, as illustrated in Figure 3.

1. **White-box models:**
   Detailed 2D and 3D Computational Fluid Dynamics (CFD) models are used to study complex phenomena taking into account the non-homogeneity of flow and thermal field. In addition, in reactor analysis, detailed kinetic models in convection-diffusion reaction systems are considered in order to accurately evaluate all physical and chemical characteristics. Since simplifications are avoided, on one hand, the model provides a high level of accuracy; on the other hand, it includes a huge number of differential equations and therefore it requires substantial computational power to be solved. For this reason, these white-box models are mainly practical for design purposes, geometry optimizations and offline analysis. Several

examples of aftertreatment white-box modellings such as, DPF [20], SCR [21,22] and LNT [23] applications are reported in literature.

2. **Black-box models:**
   In this category, using linearized dynamics and more algebraic equations provides the possibility to solve the system in real time applications for control purposes with extremely low computational effort, such as the work presented in [24]. However, it is noteworthy that in the case of strong nonlinearity, such as having complex reaction kinetic mechanisms, the model accuracy drops significantly.

3. **Grey-box models:**
   Reduced 1D or 0D models and in particular simplified kinetics in the case of reactor modelling result in an acceptable compromise between accuracy and computational cost required for engine and aftertreatment applications [25–27]. Grey-box models have been widely used in aftertreatment systems [28], including SCR reactor modelling for control applications [29], DPF soot loading and regeneration effect on engine performance [11].

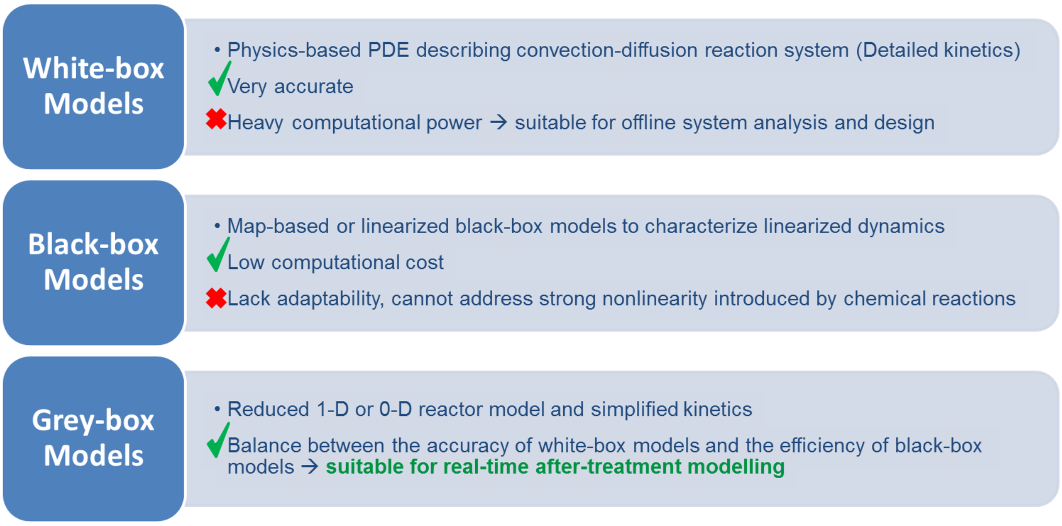

Figure 3. Summary of simulation modelling approaches for engine and aftertreatment systems

Considering the above-mentioned advantages of grey-box models in terms of accuracy and Central Processing Unit (CPU) hours in aftertreatment applications, in the present work the simulations were performed using grey-box model via commercially available 1D CFD software, GT-SUITE, based on the following assumptions:

- Any non-homogeneity and non-uniformity of flow field and thermal field in a defined cross-section is neglected.

- Only variations in the flow field direction along the catalyst length (*x*) are considered, such that the catalyst brick is divided into several sub-volumes with length *dx*, as shown in Figure 4.

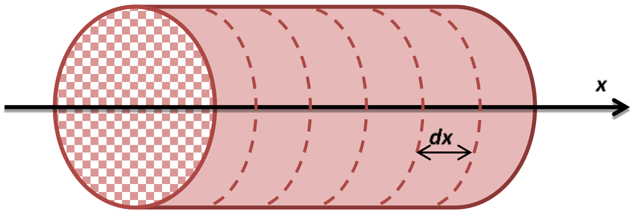

Figure 4. Discretization of the component along the catalyst axis

- Quasi-steady approximation can be applied, since the residence time of the gas in the reactor compared to other time scales is short.
- Global kinetic mechanism for the reactions is considered.
- Since the reaction rates are controlled by external mass transfer (i.e., fluid to wall) at high temperatures, a two-phase model (gas and solid phase) is used.
- Ideal gas equation is assumed for the gas phase.
- Although GT-SUITE allows to model the washcoat pore diffusion, for the sake of simplicity the washcoat pore diggusion resistance is neglected, which can be lumped into kinetic parameters.
- Since the transverse Peclet, defined as the ratio between bulk motion (advective) transport over the diffusive transport, $Pe = \frac{uR_\Omega^2}{LD_f}$, is smaller than 0.1 [30],fully-developed laminar flow through channels can be assumed.

Figure 5-a depicts a schematic view of typical components used in aftertreatment modelling, while the GT-SUITE model interface is shown in Figure 5-b. The inlet condition can be either imposed, in stand-alone applications, or be connected to an engine model. Pipes or flow junctions named as “flowsplits” are implemented in order to connect the flow to the catalyst inlet and outlet. The catalyst outlet parameters will be calculated according to the inlet condition, governing reactions which are imposed through a reaction template and geometric data entered into the catalyst brick.

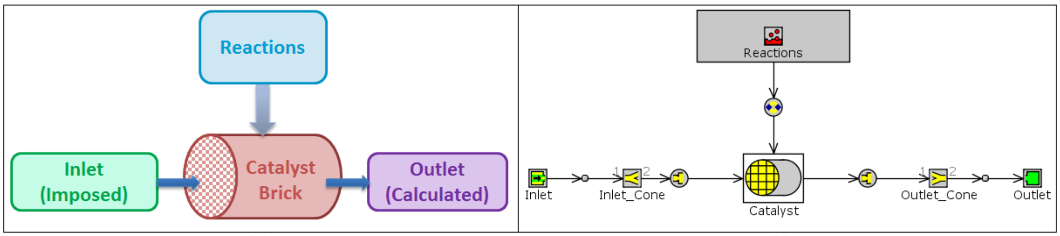

(a) (b)

Figure 5. Typical components used in aftertreatment modelling: (a) Schematic view, (b) GT-SUITE model interface

1.2.2 Model governing equations

The reactor modelling can be categorized in two main groups, as represented in [29].

1. Heat and mass transport in the reactor (internal and external diffusion, convection and conduction heat transfer)
2. Kinetics (chemical reactions)

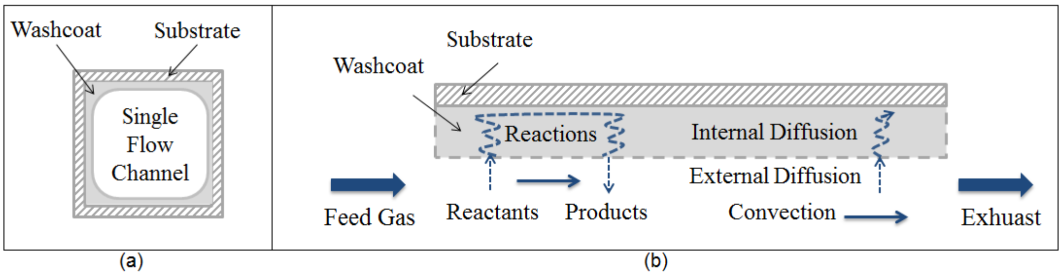

Figure 6. Physical and chemical processes occurring in a monolith channel [29]: (a) cross sectional view, (b) axial view

The main governing equations [16,29,31] are listed in the following sequence.

- Continuity equation, represented by Equation 1:

$$\frac{\partial}{\partial x}(\rho_f u) = 0 \tag{1}$$

In which:

- x is the axial position [m]
- ρ_f is the gas phase density [kg/m^3]
- u is the velocity [m/s]

- Momentum equation, represented by Equation 2:

$$\varepsilon \frac{\partial p}{\partial x} + \varepsilon \rho_f u \frac{\partial u}{\partial x} = -Sf \frac{1}{2} \rho_f u^2 \tag{2}$$

In which:

- ε is the void fraction of the reactor
- p is pressure [Pa]
- S is the surface area per reactor volume [1/m]
- f is the friction factor

- The solid phase and gas phase energy balances, Equation 3:

$$\begin{cases} Solid:\ \delta_w \rho_w C_{pw} \dfrac{\partial T_s}{\partial t} = \delta_w \lambda_w \dfrac{\partial^2 T_s}{\partial x^2} + h\left(T_f - T_s\right) - \delta_c \displaystyle\sum_{j=1}^{nrct} \Delta H_j r_j \\ Gas:\ \rho_f C_{pf} \dfrac{\partial T_f}{\partial t} = -u\, \rho_f C_{pf} \dfrac{\partial T_f}{\partial x} - \dfrac{h}{R_\Omega}\left(T_f - T_s\right) \end{cases} \tag{3}$$

In which:

- δ_c and δ_w are the effective thickness of washcoat and wall, respectively [m]
- ρ_w is the wall density [kg/m^3]
- C_{pf} and C_{pw} is the heat capacity of gas and wall, respectively [J/(kg.K)]
- T_s and T_f are the solid and gas phase temperatures, respectively [K]
- λ_w is the thermal conductivity of the wall [W/(m.K)]
- h is the convection heat transfer coefficient [W/(m^2.K)]
- ΔH_j is the enthalpy of reaction j [J/mole]
- r_j is the reaction rate of reaction j [mole/(m^3.s)]
- R_Ω is one fourth of the channel hydraulic diameter [m]

- Species balance equations, Equation 4:

$$\begin{cases} Solid:\ \dfrac{\partial X_{fm_i}}{\partial t} = -u \dfrac{\partial X_{fm}}{\partial x} - \dfrac{k_{me}}{R_\Omega}\left(X_{fm} - X_{wc}|_{y=0}\right) \\ Gas:\ \varepsilon \dfrac{\partial X_{wc_i}}{\partial t} = \dfrac{1}{C_0} \alpha_i^T r + D_s \dfrac{\partial^2 X_{wc_i}}{\partial y^2} \end{cases} \tag{4}$$

- i is the species type
- X_{wc} and X_{fm} are the species mole fraction vector in the washcoat and in the bulk gas, respectively [mole/(mole$_{tot}$.m^3)]
- k_{me} is the external mass transfer coefficient [m/s]
- y is the length co-ordinate along washcoat direction
- C_0 is the total molar concentration [mole/m^3]
- α_i^T is the stoichiometric coefficient vector of species i
- D_s is the effective diffusivity of a species in washcoat [m^2/s]
- r is the reaction rate matrix [mole/(m^3.s)]
-

- Site balance equation, Equation 5:

$$\begin{cases} \dfrac{\partial \theta_k}{\partial t} = \dfrac{1}{C_s} \alpha_{\theta_k}^T r \\ \displaystyle\sum_k \theta_k = 1 \qquad for\ each\ site \end{cases} \tag{5}$$

Where:

- k is the site type
- θ_k is the coverage of site k
- C_s is the active site density per reactor volume [$\text{mole}_{\text{active site}}/\text{m}^3$]
- $\alpha_{\theta_k}^T$ is the stoichiometric coefficient vector of site k

It is noteworthy that mass and heat transfer coefficients are calculated based on the assumption of fully-developed laminar flow through a single channel as reported in Equation 6.

$$\begin{cases} h = Nu \dfrac{\lambda_f}{D_h} \\ k_{me_i} = Sh \dfrac{\rho_f D_{s_i}}{D_h} \end{cases} \tag{6}$$

Where:

- Nu is the Nusselt number
- $\lambda_f$is the thermal conductivity of the bulk gas [W/(m.K)]
- D_h is the hydraulic diameter of the channel [m]
- Sh is the Sherwood number

Finally, concerning the kinetics modelling, the Arrhenius form function is used to evaluate the reaction rates which mainly depend on the temperature of the solid phase, local gas concentration in the washcoat and available active sites, as reported in Equation 7.

$$\begin{cases} k_i = A_i \exp\left(-\dfrac{E_{a,i}}{RT_s}\right) \\ r_i = k_i \dfrac{\Theta_\text{i} C_i}{I_i} \end{cases} \tag{7}$$

- $k_i$is the kinetic constant
- A_i is the pre-exponent multiplier of Arrhenius function for reaction *i*
- $E_{a,i}$is the activation energy of Arrhenius function for reaction *i* [J/mole]
- R is the universal gas constant and equal to 8.314 [J/(mole.K)]
- Θ_i is the active site expression for reaction *i*
- C_i is the species concentration expression for reaction *i* [mole/m^3]

- I_i is the inhibition function for reaction i

The equations expressed in this section are used as the basis for the modelling of aftertreatment systems in grey-box models such as the model embedded in GT-SUITE.

1.2.3 Model calibration approach

Regarding aftertreatment modelling and calibration, after definition of suitable kinetic model, the kinetic parameters expressed in Equation 7, should be calibrated. In order to find the optimized kinetic parameters an objective function, representing the absolute cumulative error between measured and simulated concentration of trace species at the outlet of the catalyst component, is defined. Optimization of the objective function can be carried out through different methods:

- Manual or trial and error: generally used when kinetic modelling requires deep knowledge of kinetics, such as application in Lean NO_x Trap (LNT) modelling [16], and may results in local minimum.
- Design of Experiments (DoE): which includes an initial exploration of the variables domain by running the full test matrix and therefore it is time consuming; however they can provide insight about the sensitivity of the model outputs to the parameters. These methods are not efficient in kinetic models calibration, however they are commonly used in combustion modelling [32,33].
- Numerical methods: using linear or quadratic programming, such as application in DOC modelling [34]. This method requires an initial guess and may result in local minimum.
- Direct search methods: which are based on iterative algorithms, such as discrete-grid bisection, moving along a certain direction to reach minimum and are suitable for smooth and continuous objective functions and requires suitable initial guess, an example of the application can be found in [35].
- Explorative Methods: which implies a systematic exploration of the variables domain resulting in global minimum and can be used for complex and non-linear systems, such as Genetic Algorithm (GA).

In the following sections, depending on the number of parameters and requirements of the defined kinetic scheme, suitable calibration procedure and optimization tool is adopted.

Parte del lavoro descritto in questo capitolo è stato anche preventivamente pubblicato in:

Part of the work described in this chapter was also previously published in the following publications:

1. F. Millo, M. Rafigh, D. Fino, P. Miceli, Application of a global kinetic model on an SCR coated on Filter (SCR-F) catalyst for automotive applications, Fuel. (2016). doi:10.1016/j.fuel.2016.11.082.

Chapter 2

Selective Catalytic Reduction Coated on Filter (SCR-F)

2.1 Introduction to SCR

Selective Catalytic Reduction (SCR) catalysts are one of the technologies for controlling NO_x emissions applicable over a wide range of temperatures by using ammonia as an active intermediate for NO_x reduction. Ammonia is provided to the system through urea decomposition which is injected into the exhaust line upstream of the catalyst, for active systems. NO_x reduction with ammonia is mainly controlled by the three SCR reactions expressed in Equation 8, which are usually referred as standard, fast and slow SCR. The SCR reaction kinetics highly depend on temperature and NO_2/NO_x ratio [36,37].

$$\begin{cases} Standard: & 4NH_3 - Z + 4NO + O_2 \rightarrow 4N_2 + 6H_2O + 4Z \\ Fast: & 2NH_3 - Z + NO + NO_2 \rightarrow 2N_2 + 3H_2O + 2Z \\ Slow: & 4NH_3 - Z + 3NO_2 \rightarrow 3.5N_2 + 6H_2O + 4 \end{cases} \tag{8}$$

Recently, Selective Catalytic Reduction (SCR) catalysts [38] coated on Diesel Particulate Filters (DPF) [39], often referred to as SCR-Fs, have been introduced for automotive applications due to capability of reducing NO_x and PM simultaneously, as depicted in Figure 7. Moreover, as a result of combining different aftertreatment components, in SCR-F technology, reduced packaging volume and cost [40], in addition to lower thermal capacity [41] and faster warm-up [18] for automotive applications are obtained.

Several studies have been carried out on SCR-F applications and modeling. As an example, Schrade et al. [42] developed a global kinetic model based on Synthetic Gas Bench (SGB) experimental data. Colombo et al. [43], transferred an existing SCR kinetic model into the wall of a DPF to assess the impact of soot on DeNOx activity and also SCR coating effect on soot conversion efficiency. Another SCR-F model was developed by Watling et al. [40], through the combination of an SCR kinetic model of a flow-through monolith and a physical model of a coated DPF, assuming that SCR coating does not affect soot oxidation kinetics.

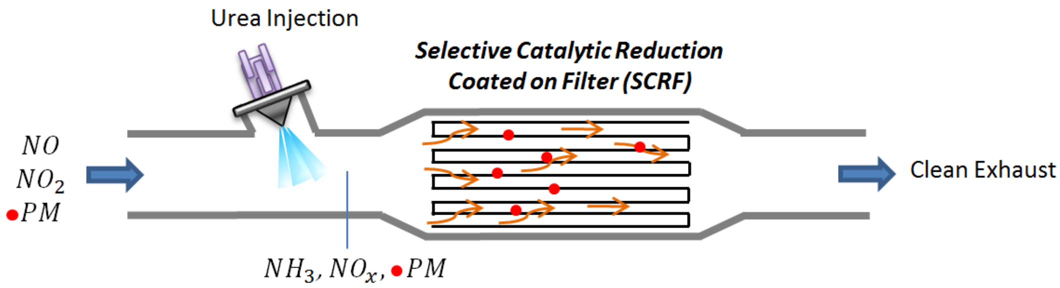

Figure 7. SCR-F operating principle

In this chapter the performance of a Silicon Carbide Cu/zeolite SCR-F device for controlling NO_x emissions for automotive diesel applications was analyzed, with the aim to investigate its catalytic properties and to build a simulation model of the aftertreament device capable of predicting ammonia storage capacity, NO_x conversion efficiency and soot conversion due to passive regeneration.

2.2 Experimental set-up

The experimental activity was performed at ACA – Center for Automotive Catalytic Systems of the RWTH Aachen University through a Synthetic Gas Bench (SGB), as it is shown in Figure 8-a. The sample is put into an isothermal cylindrical reactor which was placed in a furnace and the gases were mixed from compressed gas cylinders using mass flow controllers. The reactor core sample has a diameter around 18 mm and a length around 178 mm. As depicted in Figure 8-b two thermocouples, 0.5 mm diameter each, are mounted in the gas flow upstream, TUS, and downstream, TDS, of the sample. Moreover, the temperatures at the sample central channel inlet, T1, middle (3 radial positions, T2, T4, T5), and outlet, T3, have also been measured. An example of inlet and outlet gas temperatures for some tests is presented in Figure 9 confirming the assumption of isothermal condition (not presence of external heat loss) due to negligible temperature difference between inlet and outlet, even for the soot loaded sample in which passive soot regeneration occurs.

Gas concentration measurements were performed with a multicomponent Fourier Transform Infrared (FTIR) with 1 Hz sampling frequency. Moreover, lambda evaluation was performed via Lambdasonde (UEGO) and calculation from feed gas.

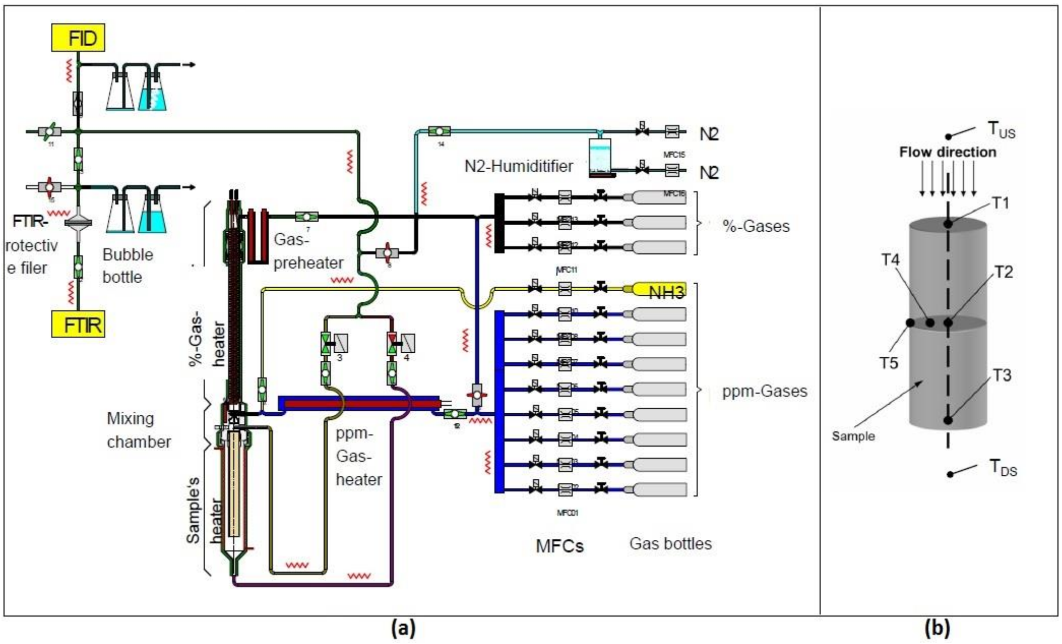

Figure 8. Experimental setup: schematic view Synthetic Gas Bench (SGB) (a) and thermocouple locations on the lab scale sample (b)

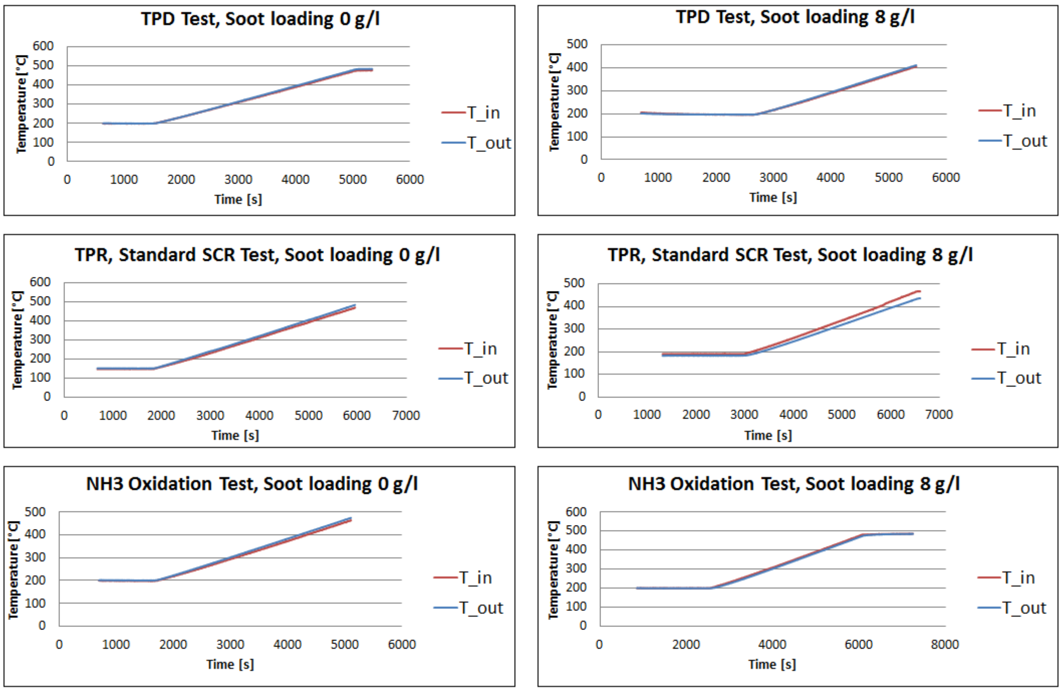

Figure 9. Example of inlet and outlet gas temperatures for soot loaded and soot free samples

The lab-scale samples were obtained from a full-scale monolith (the main characteristics of which are reported in Table 1). The catalyst sample is a Si/C washcoated with Cu/zeolite with a cell density of 300 cells per square inch (cpsi) and wall thickness of 0.012 inch (equivalent to 0.3 mm).

Table 1. Characteristics of the full-scale catalytic component

Characteristic	**Unit**	**Value**
Substrate material	-	Cordierite
Cell density	cpsi	300
Wall thickness	mm, (in)	0.3, (0.012)
Dimensions (short dia. x long dia. x length)	mm x mm x mm	137.16 x 137.16 x 177.8

Soot loading has been performed with a small displacement Yanmar diesel generator engine under constant load conditions by using the soot filter canning shown in Figure 3-b for parallel loading of up to 8 samples. The conditioning was done in oven at 200 °C for a duration of 1 hour.

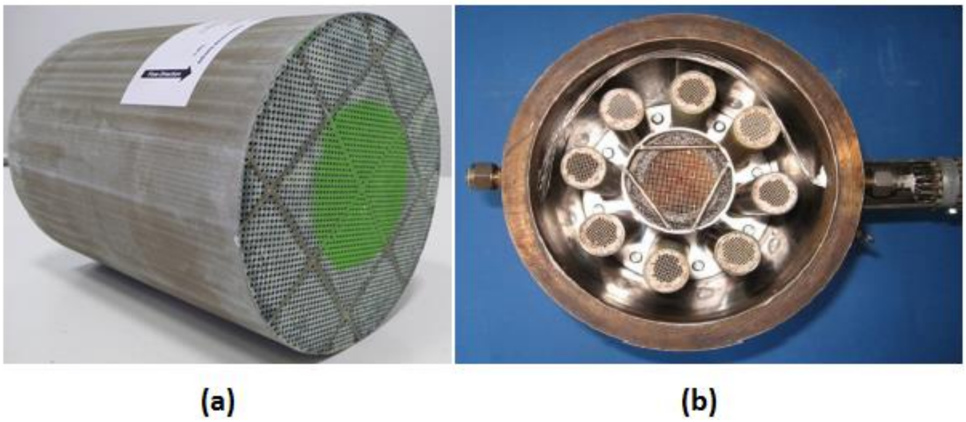

Figure 10. SCR-F samples; (a) full-scale monolith, (b) canning used for soot loading of samples

Two different soot loadings were tested in this work, 0 and 8 g/l respectively. Soot distribution was assumed uniform throughout the sample.

2.3 Test protocols

The test protocol includes 3 main steps performed on both soot-free and soot-loaded samples:

1. NO Oxidation test
2. Temperature Programmed Desorption (TPD) test
3. Temperature Programmed Reduction (TPR) test

2.3.1 NO oxidation test

Considering that SCR reactions depend on the NO_2/NO_x ratio, it is important to characterize the NO oxidation reaction. This test is therefore carried out with the inlet batch composition reported in Table 2, for two different standard space velocities, 30000 and 60000 1/hr, and the temperature is ramped up from 100 to 430 °C with a constant rate of 5 K/min. Reference temperature and pressure for the measurement of space velocity are 273.15 K and 101325 Pa, respectively.

Table 2. Inlet gas composition for NO oxidation test (concentrations on volume basis)

Species	**Concentration**
NO [ppm]	400
O_2 [%]	10
CO_2 [%]	5
H_2O [%]	5
N_2	Balance

2.3.2 Temperature Programmed Desorption (TPD) test

TPD test is utilized to obtain ammonia storage capacity versus temperature and consists of two main parts. In the present work, tests were carried out using a space velocity of 60,000 1/hr [44]. Reference temperature and pressure for the measurement of space velocity are 273.15 K and 101325 Pa, respectively.

During the first phase, named NH_3 adsorption, a mixture of gases with the composition reported in Table 3 is introduced into the catalyst while keeping the inlet temperature at a constant level, referred to as adsorption temperature, T_{ads}. This phase is continued until equilibrium coverage is reached so that the inlet NH_3 concentration is equal to the outlet one and the adsorption sites are saturated, as shown in Figure 11. The test is repeated for 3 different adsorption temperatures, 150, 200 and 250 °C.

Table 3. Inlet gas composition for TPD experiment (concentrations on volume basis)

Species	**NH_3 Adsorption Phase**	**T ramp phase**
NH_3 [ppm]	500	-
H_2O [%]	10	10
N_2	Balance	Balance

In the second phase, named temperature ramp phase, after stopping ammonia injection at the inlet, the inlet gas temperature in increased linearly with a constant rate of 5 K/min; hence, giving the possibility to characterize ammonia desorption as a function of temperature.

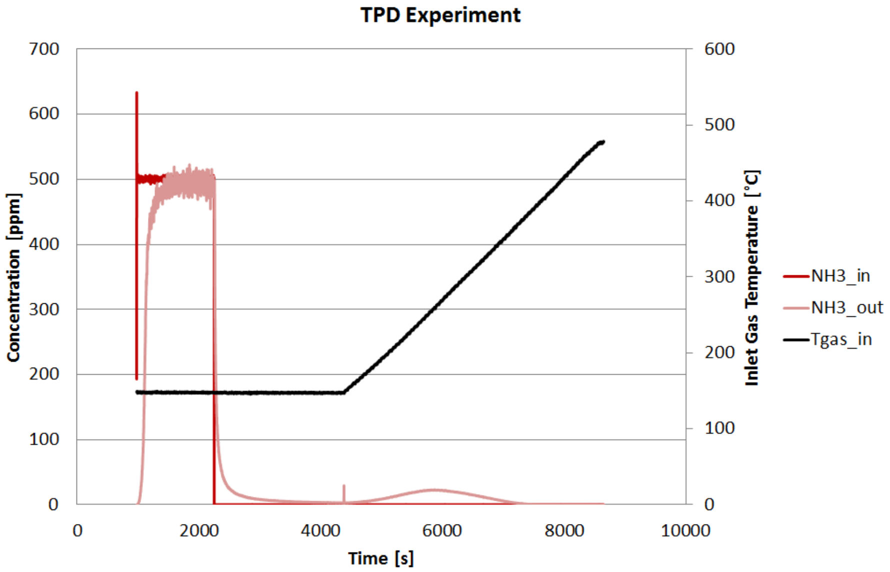

Figure 11. Measured NH_3 traces at inlet and outlet of catalyst sample during TPD test

2.3.3 Temperature Programmed Reduction (TPR) test

TPR test is performed similarly to TPD, at the same space velocity, with the aim to characterize NH_3 oxidation, standard, slow and fast SCR reactions using different NO_2/NO_x ratios [44]. The NH_3 adsorption phase is identical to the TPD one, with the inlet composition reported in Table 3. Subsequently, the temperature ramp phase is repeated for 4 different inlet batch conditions as reported in Table 4.

Table 4. Inlet gas composition for TPR experiment (concentrations on volume basis)

Species	**NH_3 Ads. Phase**	**T Ramp Phase**			
		NH_3 oxidation	Standard SCR	$NO_2/NO=1$	$NO_2/NO=2$
NH_3 [ppm]	500	-	-	-	-
NO [ppm]	-	-	100	50	33.33
NO_2 [ppm]	-	-	-	50	66.67
O_2 [%]	-	10	10	10	10
H_2O [%]	10	10	10	10	10
N_2	Balance	Balance	Balance	Balance	Balance

2.4 Simulation model and kinetics calibration

The SCR-F model was built for the reactor-scale sample, i.e. for a cylinder of 18.5 mm diameter and a length of 164.5 and 100 mm, for soot-free and soot-loaded samples, respectively, using the commercially available 1D fluid-dynamic simulation code GT-SUITE, developed by Gamma Technologies Inc. The 1D simulation model is based on the assumptions discussed in Chapter 1.2.

The reaction model is a global-type surface reaction series using Turnover Number reaction rate format in which the rate expression is entered with implied unit of [mole/s/moles of active sites] [31]. It incorporates the ammonia adsorption/desorption, NO and ammonia oxidation and NO_x reduction reactions via ammonia, named SCR reaction model. The reaction rates can be expressed by general form of Arrhenius term as shown in Equation 7.

Thanks to a proper test protocol characterization, the reaction model can be calibrated independently. The reactions are listed in Table 5. The calibration parameters include the zeolite site density in addition to pre-exponent multiplier and activation energy of each reaction.

The calibration is started from adsorption/desorption reaction focusing on TPD test experimental data. In this step, Reaction 1 and Reaction 2 are calibrated. The optimization is performed using the automatic optimizer of GT-SUITE, Brent method, with the aim to minimize the objective function defined as the absolute cumulative error between simulation and experimental concentration of products, in this case ammonia, as expressed in Equation 9.

$$F_{obj} = \frac{1}{t_{end}} \int_0^{t_{end}} abs(product_{sim} - product_{meas})dt \tag{9}$$

The next step is dedicated to calibration of the NO oxidation reaction, Reaction 3. It is important to note that at higher temperatures NO_2 can be decomposed to NO and O_2; therefore, the reverse reaction is considered using the equilibrium constant calculated on the basis of thermodynamics and Gibbs free energy, as expressed in Equation 10.

$$K_{eq} = \exp\left(-\frac{\Delta G}{RT}\right) \tag{10}$$

For global reaction modeling, a linear approximation of the change in Gibbs free energy with respect to temperature is sufficient [31].

Afterwards, SCR reactions are calibrated according to TPR measurements. Moreover, it has been observed, [42,45], that at low temperatures when NO_2 is present, NH_4NO_3 is formed via Reaction 8, which is then decomposed at higher temperatures through Reaction 9.

Table 5. Global kinetic reactions on the washcoat layer

#	Model	Rate Expression
1	$NH_3 + Z \rightarrow NH_3 - Z$	$k_1 C_{NH_3} \theta_Z$
2	$NH_3 - Z \rightarrow NH_3 + Z$	$k_2 \theta_{NH_3-Z}$
3	$NO + 0.5O_2 \leftrightarrow NO_2$	$k_3 (C_{NO} C_{O_2}^{0.5} - C_{NO_2}/K_{eq})$
4	$4NH_3 + 3O_2 \rightarrow 2N_2 + 6H_2O$	$k_4 C_{NH_3} C_{O_2}$
5	$4NH_3 - Z + 4NO + O_2 \rightarrow 4N2 + 6H2O + 4Z$	$k_5 C_{NO} \theta_{NH_3-Z}^2$
6	$2NH_3 - Z + NO + NO_2 \rightarrow 2N2 + 3H2O + 2Z$	$k_6 C_{NO} C_{NO_2} \theta_{NH_3-Z}$
7	$4NH_3 - Z + 3NO_2 \rightarrow 3.5N_2 + 6H_2O + 4Z$	$k_7 C_{NO_2} \theta_{NH_3-Z}$
8	$NO_2 + 2NH_3 + Site \rightarrow NH_4NO_3\text{-}Site + N_2 + H_2O$	$k_8 C_{NH_3} C_{NO_2} \theta_{site}$
9	$NH_4NO_3\text{-}Site \rightarrow NO_2 + NH_3 + 0.5H_2O + 0.25O_2 + Site$	$k_9 \theta_{NH_4NO_3-site}$

After calibration of soot free sample kinetics, experimental measurement for the 8 g/l soot loaded sample can be further used for the calibration of soot reactions over the soot cake layer, as shown in Table 6. It is noteworthy that kinetic parameters are calibrated according to CO and CO_2 traces detected downstream of the reactor as a result of passive soot regeneration.

Table 6. Global kinetic model on the soot cake layer

#	Model	Rate
10	$C + O_2 \rightarrow CO_2$	$k_{10} C_{O_2} C_C$
11	$C + 0.5O_2 \rightarrow CO$	$k_{11} C_{O_2} C_C$
12	$C + 2NO_2 \rightarrow CO_2 + 2NO$	$k_{12} C_{NO_2} C_C$
13	$C + NO_2 \rightarrow CO + NO$	$k_{13} C_{NO_2} C_C$

In order to decouple the effect of soot oxidation by O_2 and by NO_2, first, Reactions 10 and 11, which are soot oxidation by O_2, were calibrated according to TPR test data in which NO_2 is not present. Subsequently, Reactions 12 and 13 were calibrated using other TPR tests in which NO_2 was present in the inlet batch. It should be noted that the calibration of the SCR model is performed only based on the soot-free sample, and is then further validated for the soot-loaded component. The optimized kinetic parameters found for the reactions listed in Table 5 and Table 6 are reported in Table 7.

Table 7. Optimized kinetic parameters for the SCR-F global kinetic model

#	Pre-exponent Multiplier	Activation Energy [J/mol]
1	3.413	0
2	2.97E8	$118876(1 - 0.36\theta_{NH_3-Z})$
3	84.112	45483.6
4	1.68E11	144625.5
5	6.47E15	146941.9
6	4.99E15	107878.8
7	1.09E17	197178.1
8	3.32E5	0
9	9.09E5	62234.8
10	4.9E9	83144.9
11	2.9E8	74515.9
12	5E15	91459.4
13	8E12	66515.9

2.5 Results and discussion

A comparison between predicted and measured ammonia concentrations downstream of the catalyst component for 3 different adsorption temperature levels is shown in Figure 12. It can be observed that the instantaneous concentration traces coming from the simulation model follow measured data with acceptable accuracy both for the soot-free and the soot-loaded samples, especially during ramp-up phase which is of more interest due to SCR reactions.

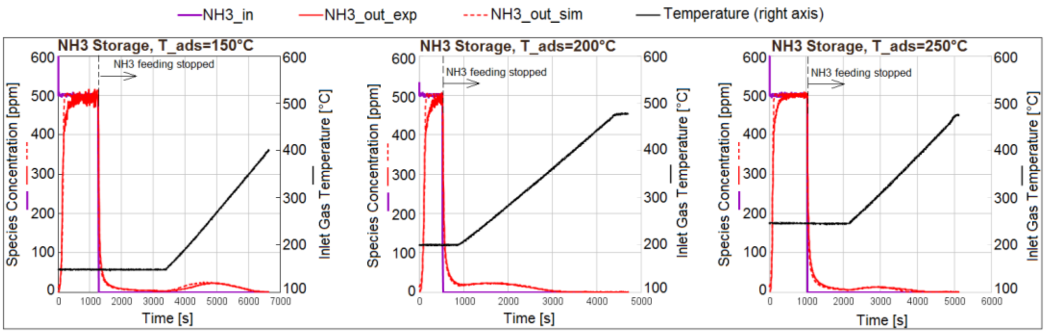

(a) Soot free sample

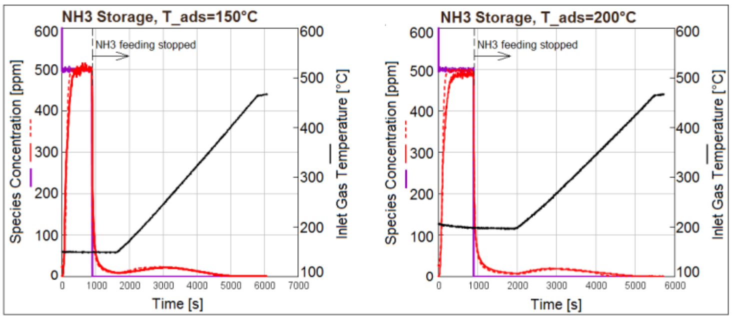

(b) Soot loaded sample 8 g/l

Figure 12. Predicted versus experimental ammonia concentration downstream of catalyst during TPD test; (a) soot free sample, (b) soot loaded sample 8 g/l. Temperature is plotted on the right axis and concentrations are plotted on the left axis (dashed line represents simulation result and full line refer to the measured value)

Moreover, NH_3 storage capacity as a function of temperature is shown in Figure 13. Linear decrease of NH_3 storage capacity is obtained by increasing temperature, with a maximum error of 6% between predicted and measured values.

Comparing soot-loaded and soot-free samples storage capacity, soot has a minor impact on ammonia storage capacity; however slight improvement on the storage capacity, specifically at T<250 °C, can be observed with the soot-loaded sample due to its higher geometric surface area, which is consistent with the study performed by Schrade et al. [42].

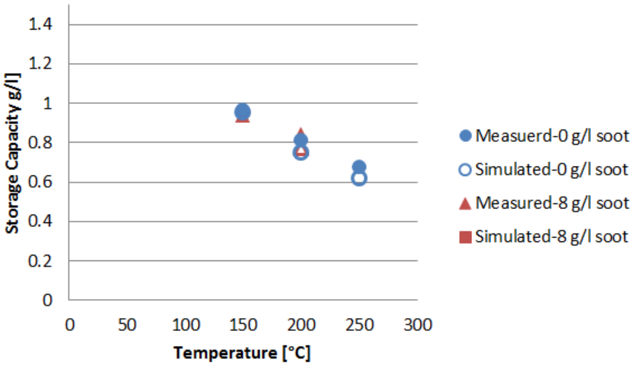

Figure 13. Ammonia storage capacity as a function of temperature

Considering NH_3 oxidation test, the instantaneous NH_3 traces at the outlet of the SCR-F component for 2 different adsorption temperatures, 150 and 200 °C, are shown in Figure 14. It can be observed that the simulation results are in good agreement with experimental data. As expected [40,45] ammonia oxidation will occur at temperatures around 350-400 °C; hence, the effect at such low temperatures, 250 °C, is not significant. Therefore, in order to obtain more information regarding ammonia oxidation, it is required to perform the test at higher temperatures. Moreover, it can be observed that NH_3 is only converted to N_2, since NO was not detected downstream of the catalyst during this experiment, although conversion to NO was reported in literature [40] at temperatures higher than 550 °C.

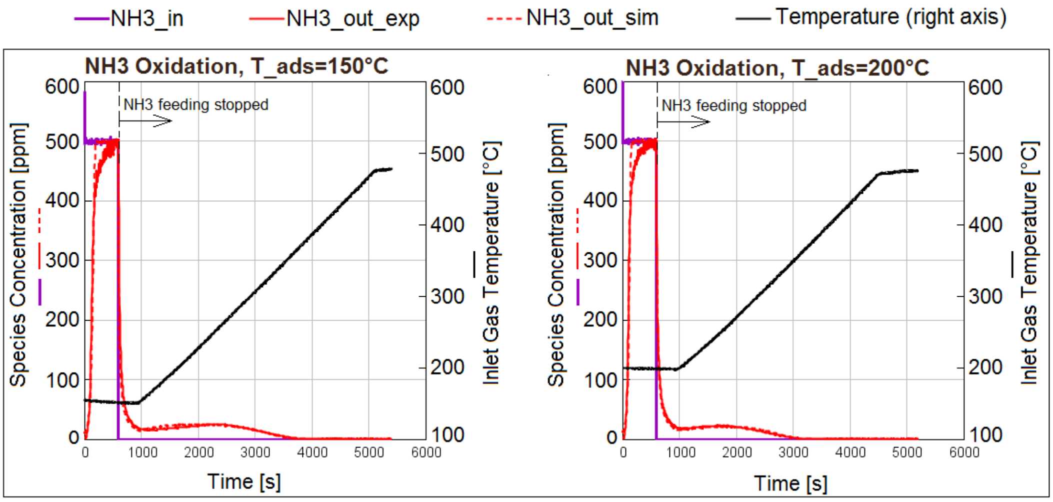

(a) Soot free sample

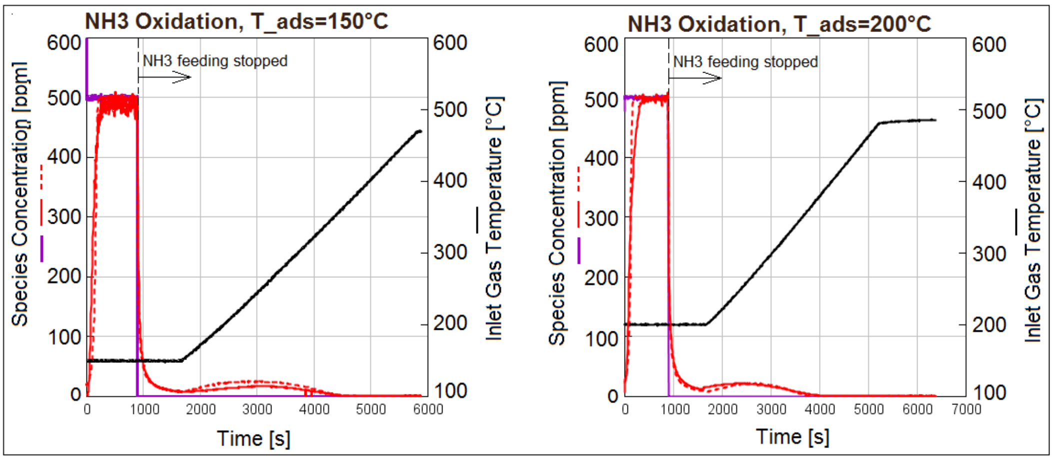

(b) Soot loaded sample 8 g/l

Figure 14. Predicted versus experimental ammonia concentration downstream of catalyst during TPR test, characterizing NH_3 oxidation; (a) soot free sample, (b) soot loaded sample 8 g/l. Temperature is plotted on the right axis and concentrations are plotted on the left axis (dashed line represents simulation result and full line refer to the measured value)

The results of NO oxidation test for the two tested space velocities, 30000 and 60000 1/hr, are depicted in Figure 15. It can be observed that at temperatures higher than 250 °C NO starts to be oxidized and converted to NO_2 and, as expected, the conversion is faster for lower space velocities, i.e. higher residence times. It is worth noting that the predicted results are in acceptable agreement with measured data.

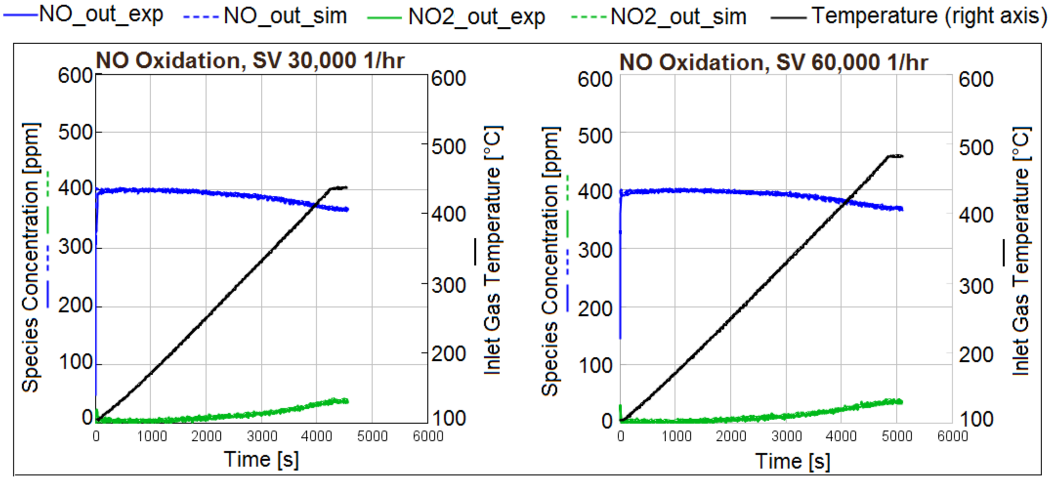

(a) Soot free sample

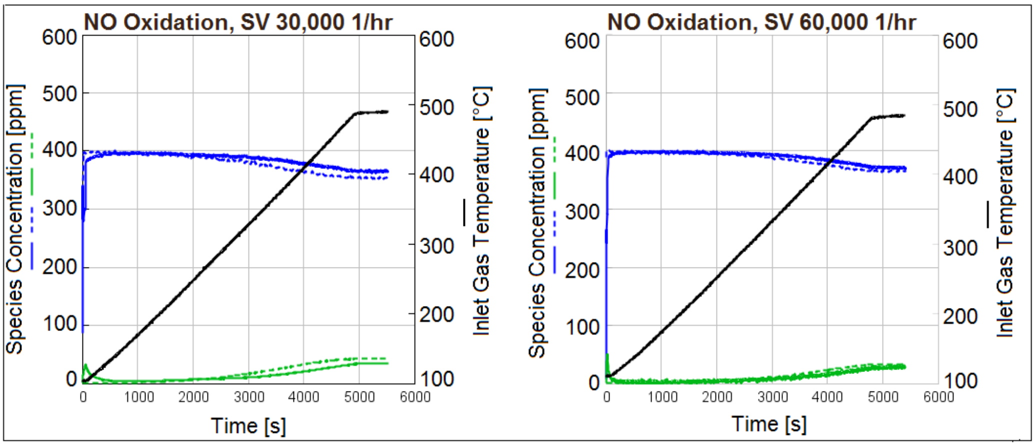

(b) Soot loaded sample 8 g/l

Figure 15. Predicted versus experimental ammonia concentration downstream of catalyst during NO oxidation test; (a) soot free sample, (b) soot loaded sample 8 g/l. Temperature is plotted on the right axis and concentrations are plotted on the left axis (dashed line represents simulation result and full line refer to the measured value)

As far as NO_x reduction with ammonia is concerned, it can be seen from Figure 16 that NO_x conversion is a function of temperature, NO_2/NO_x ratio and availability of the reductant. Focusing on Figure 16-a-A , representing the behavior of the soot free component in which only NO is present, NO_x conversion is increased initially due to increase in temperature; then, after reaching a maximum, it declines due to consumption of adsorbed ammonia; hence, unavailability of sufficient reductant overcomes the temperature effect resulting in decrease of NO conversion efficiency.

As it can be appreciated from Figure 16-a-B and Figure 16-a-C, at lower temperatures initially NO_2 concentrations drop: this can be related to the formation of NH_4NO_3 (according to [46,47]), which is decomposed at higher temperatures. Consequently, comparing different NO_2/NO ratio cases in Figure 16-a, it is observed that conversion of NO_2 is higher with respect to NO at low temperatures. This phenomenon is well-captured by the simulation model and an acceptable agreement between predicted and measured NO_x traces can be observed.

It is worth remarking that slow SCR, Reaction 7 in Table 5, takes place at higher temperatures; therefore, the effect may not be so visible at temperatures below 200 °C [48]. Moreover, at low temperatures [49,50] and low NO_2/NO_x [42] soot consumption by NO_2 is small: hence, NO_2/NO_x ratio is not altered, and as a consequence, NO_x conversion is not affected. On the other hand, at higher temperatures, depending on the inlet NO_2/NO_x ratio, soot can improve or deteriorate NO_x conversion efficiency due to local change in the NO_2/NO_x ratio through soot oxidation by NO_2 [40,51,52].

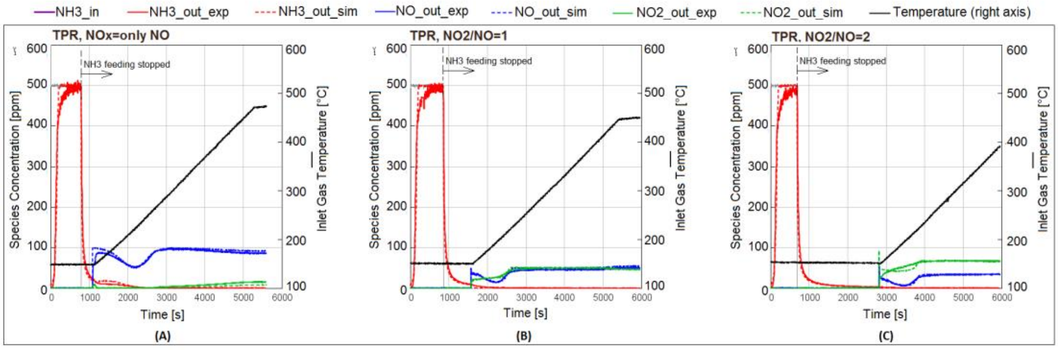

(a) Soot free sample

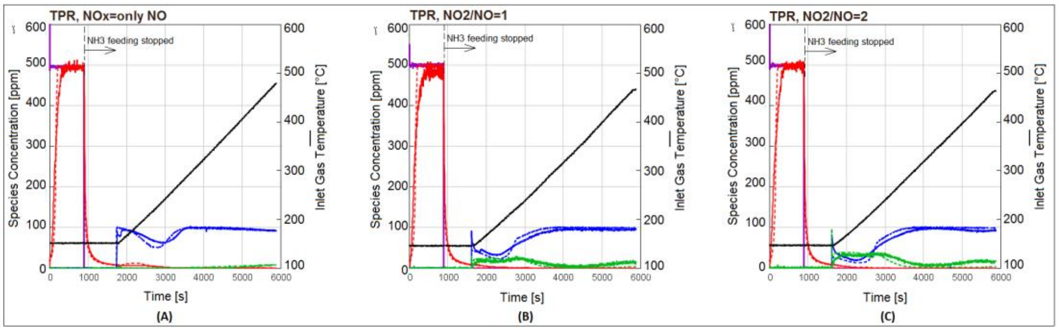

(b) Soot loaded sample 8 g/l

Figure 16. Predicted versus experimental NH_3, NO and NO_2 concentration downstream of catalyst during TPR test, characterizing NO_x conversion using different NO_2/NO ratios; (a) soot free sample, (b) soot loaded sample 8 g/l. Temperature is plotted on the right axis and concentrations are plotted on the left axis (dashed line represents simulation result and full line refer to the measured value)

Considering soot-loaded sample results, in Figure 16-b, when NO_2 is not present (Figure 16-b-A), NO outlet concentration is not affected by the presence of soot. However, when NO_2 is included in the inlet batch after ammonia is consumed, lower NO_2 and higher NO are detected due to soot regeneration, while the NO_x balance will not be affected, which is in agreement with the study performed by Marchitti et al. [52].

Furthermore, NO_x conversion efficiency as a function of temperature is depicted in Figure 17, in which simulated results follow the measured values with acceptable accuracy. As reported in literature [53,54], the maximum NO_x conversion is seen at equimolar NO and NO_2 composition, $NO/NO_2=1$. When the samples are soot-loaded, local NO_2/NO_x ratio will change; therefore, for $NO_2/NO=2$ higher NO_x conversion is detected for the soot-loaded sample compared with the soot-free one, due to consumption of NO_2 and production of NO as a result of passive soot regeneration, hence reducing the NO_2/NO ratio. On the other hand, at equimolar NO_2/NO a slight decrease is observed for the soot-loaded sample. Similar results regarding the effect of soot on SCR pathway have been reported by Tronconi et al. [55] and Marchitti et al. [52].

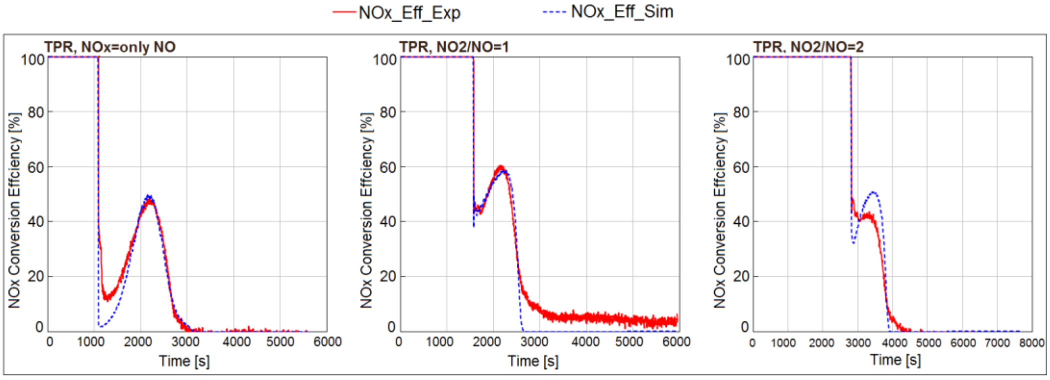

(a) Soot free sample

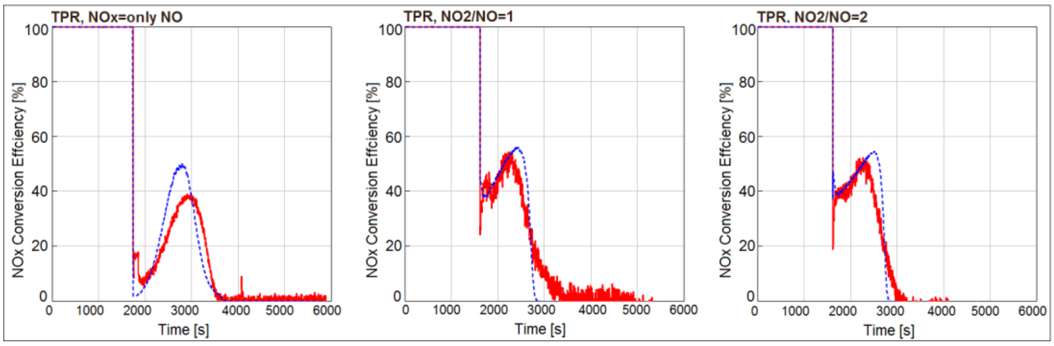

(b) Soot loaded sample 8 g/l

Figure 17. Predicted versus measured NO_x conversion efficiency during TPR test using different NO_2/NO ratios; (a) soot free sample, (b) soot loaded sample 8 g/l

Finally, total soot converted during TPR tests is estimated by stoichiometry using the amount of produced CO and CO_2 (Table 6) and considering that CO/CO_2

are not included in the inlet batch and are only formed as a results of soot conversion.). The mass of converted soot is calcutated by Equation 11 using the molecular mass of carbon, Mw_C.

$$soot\ converted\ [g] = Mw_C \int_{t_{start}}^{t_{end}} \left(\dot{n}_{CO,out} + \dot{n}_{CO_2,out}\right) dt \qquad (11)$$

The total soot converted in TPR experiemnts is shown in Figure 18. Because of the simplifying assumptions made concerning the soot characteristics and its distribution along the channel length (currently assumed to be uniform), combined with the complexity of soot chemical kinetics, some errors in terms of total soot converted predicted by the model have to be expected. Moreover, it can be observed that NO_2 can increase passive soot regeneration by about 50%, compared to the case in which only NO is present in the inlet batch.

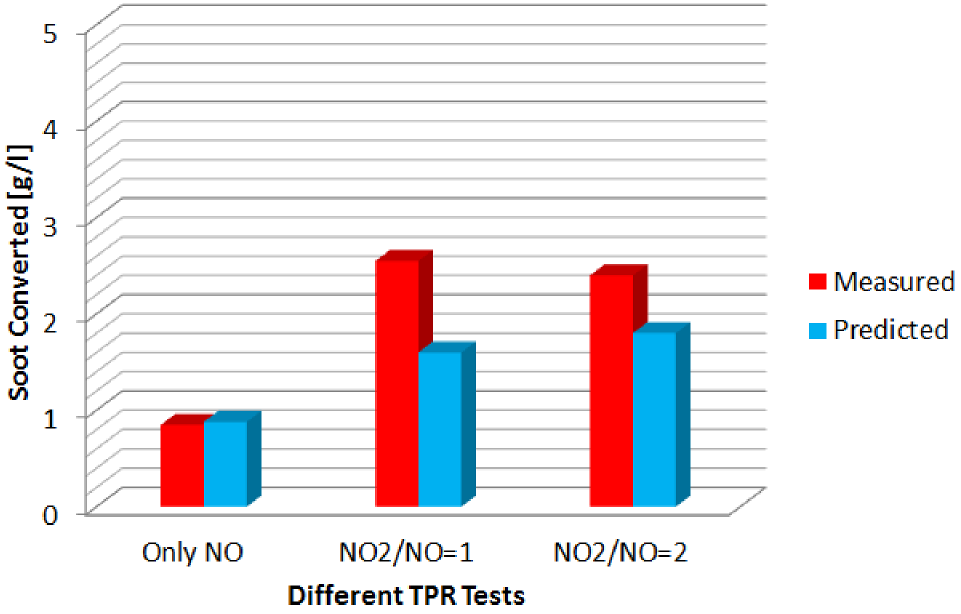

Figure 18. Soot converted during TPR experiment at different NO_2/NO_x ratios

Parte del lavoro descritto in questo capitolo è stato anche preventivamente pubblicato in:

Part of the work described in this chapter was also previously published in the following publications:

1. F. Millo, M. Rafigh, S. Wahiduzzaman, R. Dudgeon, Calibration of a Global Kinetic Mechanism Based on Synthetic Gas Bench Experiments for a Lean NOx Trap Catalyst for Automotive Applications, THIESEL Conf. Thermo-Fluid Dyn. Process. Direct Inject. Engines. (2016).

2. M. Rafigh, R. Dudgeon, J. Pihl, S. Daw, R. Blint, S. Wahiduzzaman, Development of a Global Kinetic Model for a Commercial Lean NOx Trap Automotive Catalyst Based on Laboratory Measurements, Emiss. Control Sci. Technol. (2016). doi:10.1007/s40825-016-0049-8.

Chapter 3

Lean NO$_x$ Trap (LNT)

3.1 Introduction to Lean NO$_x$ Trap

Lean NO$_x$ Trap (LNT), or also referred to as NO$_x$ Storage Reduction (NSR) catalysis [56] and NO$_x$ Storage Catalyst (NSC), is one of the lean-NO$_x$ reduction strategies proposed in the last decades [57,58]. LNT catalysts function by being cycled through a repetitive lean/rich process [14]. Initially, NO$_x$ is trapped by forming solid nitrates and nitrites on a component of the LNT surface (for example BaO) when the exhaust is lean (i.e., contains excess oxygen), Figure 19-a. The chemical mechanisms underlying the trapping process have been investigated by a number of authors [59,60].

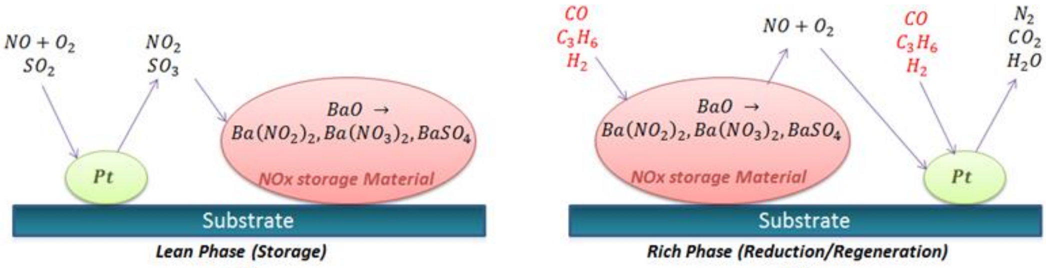

(a) (b)

Figure 19. Principle operation of Lean NO$_x$ Trap

Before the NO$_x$ absorbing sites become saturated, the catalyst is transitioned into a regeneration phase. In this phase, the catalyst is briefly exposed to a gas mixture with very low or no oxygen and containing relatively higher concentrations of H_2, CO, and HCs, thereby reducing the nitrates and nitrites to N_2, Figure 19-b.

The effect of different reductants on the NO_x conversion efficiency has been evaluated by several authors [61–63]. Al-Harbi et al. concluded [63] that when CO is used as the reductant, it reacts with water vapor via Water Gas Shift (WGS) to produce H_2, which can also act as a reductant. Recent studies such as that by Masdrag et al [64] have also demonstrated that unintended by-products such as NH_3 and N_2O (a greenhouse gas [65]) can be produced as well during regeneration, thereby emphasizing the importance of understanding the details of LNT kinetics. Typical LNT catalysts also contain precious metal components such as Pt, to promote storage and reduction.

3.1.1 NO_x Storage Mechanism

The mechanisms for NO and NO_2 storage on barium and ceria have historically been not well understood, thereby making them difficult to model. One difficulty arises from the ability of NO_x to store on many components commonly found in oxidation catalysts, including Ce [66] and K [67,68] in addition to Ba. Another difficulty is the non-monotonic relationship between measured NO_x storage capacity and temperature. The customary method to test species storage capacity on an exhaust aftertreatment catalyst is to feed a catalyst sample with a constant concentration of species until the catalyst storing capacity saturates and the outlet concentration is the same as the inlet concentration.

Many LNT studies report that the NO_x storage capacity increases with increasing temperature until around 300-350°C where it peaks, then decreases upon further increasing the temperature. Some studies have noted that 300-350°C is also the temperature range at which the reversible NO oxidation reaction most strongly favors NO_2 production, before thermodynamic equilibrium begins to favor NO again as the temperature is increased beyond that range. Many studies have concluded that NO_2 stores more easily to Ba/Pt sites and the NO_2/NO ratio plays an important role in the NO_x storage capacity [69,70]. Despite these more recent findings, mathematical models of NO_x storage on Ba/Pt sites have achieved mixed success. Some studies [71] report that mass transfer of stored species in the washcoat plays an important role in the overall NO_x storage behavior and this mechanism is not well understood.

The non-monotonic relationship between NO_x storage capacity and temperature, as well as the lack in understanding any potential mass transfer effects, has led some modelers to take a phenomenological approach to modeling NO_x storage on LNTs. Kočí et al. [70] used an equilibrium storage capacity approach, where the local stored NO_x coverage is subtracted from a temperature-dependent equilibrium coverage to determine adsorption rate. Similar approaches have been employed in [72–75]. With such an approach, adsorption reactions are defined as Equation 12 and Equation 13 with rate expression reported as Equation 14.

$$BaCO_3 + 2NO + 1.5O_2 \rightarrow Ba(NO_3)_2 + CO_2 \tag{12}$$

$$BaCO_3 + 2NO_2 + 0.5O_2 \rightarrow Ba(NO_3)_2 + CO_2 \tag{13}$$

$$r_i = k\Psi_{NO_x}^{cap} C_{NO_x} C_{O_2} \left(\theta_{NO_x}^{eq} - \theta_{NO_x}\right)^2 \tag{14}$$

where $\Psi_{NO_x}^{cap}$ is the storage capacity and $\theta_{NO_x}^{eq}$ is the temperature dependent equilibrium coverage, which would need to be fit to NO_x storage experiments. This modeling approach is a convenient one for ensuring a model follows NO_x storage capacity vs. temperature data and avoids the complex processes occurring on Ba/Pt sites, but it is a non-physical model with a couple different problems. First, this model ignores NO_x desorption from the surface. Although the rate expression in Equation 18 can be modified to include the sign of the difference inside the parentheses to make the reaction reversible, doing so would make the reverse reaction dependent on the NO_x and O_2 concentration, which is not physical. In addition, these reactions predict zero rates of adsorption in the absence of O_2, whereas the important disproportionation reaction as a storage pathway does not rely on O_2.

Nova et al. [56] tested NO_x storage on Pt/Al_2O_3, Ba/Al_2O_3, and $Pt\text{-}Ba/Al_2O_3$ samples and found NO_2 adsorption on Ba via the disproportionation reaction is more efficient than that of NO/O_2. The disproportionation reaction is a series of three steps, Equations 15, 16 and 17:

$$BaO + NO_2 \rightarrow BaO - NO_2 \tag{15}$$

$$BaO - NO_2 \rightarrow BaO_2 + NO \tag{16}$$

$$BaO_2 + 2NO_2 \rightarrow Ba(NO_3)_2 \tag{17}$$

whose net reaction is referred to as the single-step disproportion reaction, Equation 18:

$$BaO + 3NO_2 \rightarrow Ba(NO_3)_2 + NO \tag{18}$$

They also found that the main pathway for NO storage in the presence of O_2 was the formation of less stable Ba-nitrites that progressively transform on the surface to more stable Ba-nitrates. They found that increasing the number Pt-Ba neighboring sites increased NO_x breakthrough times and overall NO_x storage capacity. Chaugule et al. [69] measured NO_x storage on LNT samples with different Pt/Ba loadings at 300 °C and found each of these sites play an important role in both NO and NO_2 storage and the formation of stable Ba-nitrates. They found difficulty in describing NO_x storage with only one or perhaps two sites. Rather, Chaugule et al. [69] conclude that the following four sites (three functionally) describe NO_x storage on barium.

1. Ba vicinal to Pt (storage of NO_2 and/or NO using spilled over oxygen from Pt as the oxidant).
2. Ba uninfluenced by Pt (NO_2 disproportionation using NO_2 as the oxidant).
3. $Pt/\text{-}\gamma\text{-}Al_2O_3$ (NO oxidation and NO_2 decomposition).

4. γ-Al_2O_3 (negligible NO_x storage).

However, these sites are connected in a complex kinetic manner. Consequently, the kinetic interrelation of these sites provides a temperature dependent variation of the apparent NO_x storage capacity. We have successfully described that complex interaction with a three-site model.

Some modelers have applied a two-site approach to modeling NO_x storage on LNTs. Shwan et al. [76] developed a global kinetic shrinking core model to predict NO_x breakthrough during storage. The mechanism consisted of direct adsorption of NO_2 to nitrates and NO to nitrites, both of which were made reversible using equilibrium constants. Kromer et al. [71] also used a two site model with different adsorption rates to account for different time scales observed in NO_x storage and breakthrough data. They also concluded that a NO_x storage model must include direct storage of NO to properly predict NO outlet concentrations, instead of assuming only NO_2 adsorbstion after being generated from NO oxidation.

In the current study, a three-site global storage mechanism for both case study #1 and #2 is proposed, more details can be found in Section 1.2.

3.2 Lean NO_x Trap – Case Study 1

Experimental and numerical analysis was performed with a core sample from a LNT monolith (cordierite, 400 cpsi) from a lean burn gasoline passenger car equipped with a 2.0-liter, 4-cylinder direct-injection engine.

3.2.1 Experimental Set-up

The 7.5 cm-long, 2 cm- diameter core sample was extracted from a full-size component and inserted in a tube furnace, Lindberg Blue/M Mini-Mite, to control catalyst temperature which is connected to an automated flow reactor at Oak Ridge National Lab (ORNL) [77].

Temperature was measured upstream, axial midpoint and downstream of the component with 0.5 mm diameter type K, Omega Engineering thermocouples and Omega Engineering PX419-030AV pressure transducers were used to measure pressure. Mass flow controllers, MKS 1479A, were used for mixing the inlet gases from compressed cylinders and an FTIR spectrometer, MKS Multigas 2030HS, measured the gas concentration. An electronically actuated 4-way solenoid valve, Numatics Micro-air series, was utilized for switching between lean/rich conditions. Schematic view of experimental set-up is shown in Figure 20. It is important to note that a GT-SUITE model of the flow system was created to correct the synchronization between inlet and outlet concentration measurements. Therefore, the experimental data used in the model are corrected to consider the effect of the transient and dynamic behavior of flow and measurement devices.

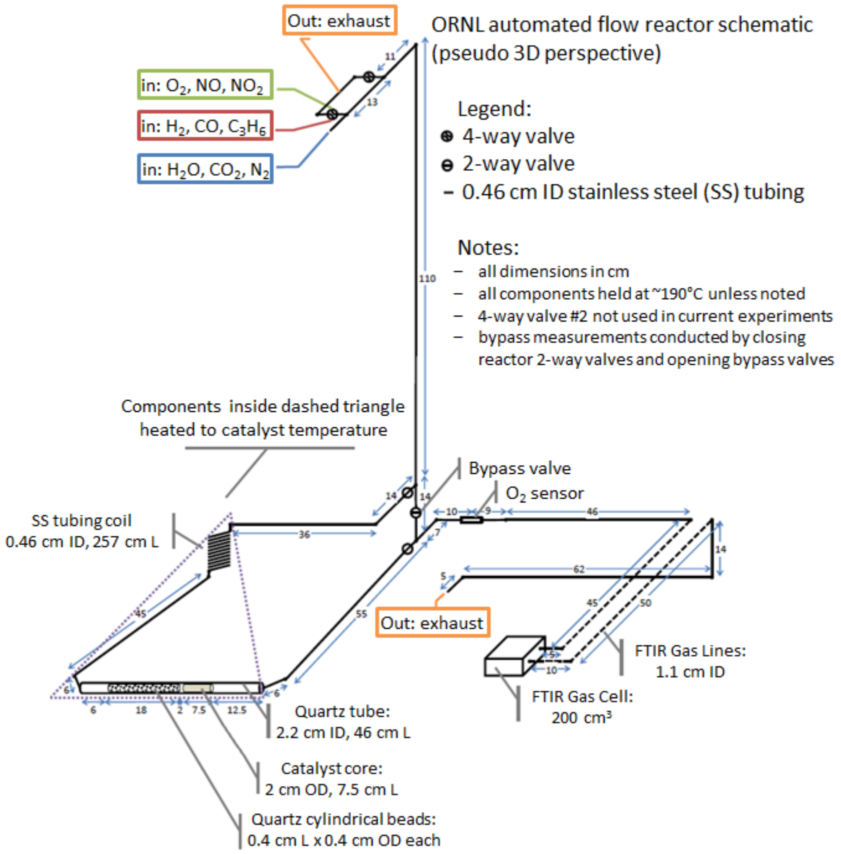

Figure 20. Schematic of the reactor system for LNT case study #1

A composition analysis, performed at ORNL, on the washcoat is summarized in Table 8. The sample washcoat thickness was measured to be 0.18 mm at the side.

Table 8. Composition analysis of the washcoat of LNT case study #1

Element	Loading (g/L)
Ba	19.98
Ce	55.51
Zr	4.32
La	2.45
Pt/Pd/Rh (1:0.31:0.12)	3.52
K	0.04
Sr	0.39
Na	0.07

3.2.2 Test protocols

Synthetic Gas Bench (SGB) test protocols are defined with the aim to decouple the effects of different mechanisms, by feeding the catalyst sample with controlled species concentrations, flow rates and temperatures, thus facilitating the model calibration process. In this context, three types of experiments are defined according to CLEERS LNT protocol [78] with the aim to characterize oxygen and NO_x storage and reduction. It should be noted that the study is not focused on light-off behavior and the main goal is focsed on the detection of suitable kinetic scheme for NO_x storage and reduction. The isothermal tests are performed at constant mass flow rate of 0.23 g/s and at five different constant temperature levels ranging from 150 °C to 550 °C, spaced equally in 1/T [K^{-1}] in order to improve resolution of the Arrhenius rate constants, resulting in 150, 209, 286, 393 and 550 °C.

3.2.2.1 Oxygen Storage Capacity (OSC)

Thanks to the presence of ceria on the washcoat layer, the LNT demonstrates oxygen storage capacity. Ceria loading promotes water gas shift reaction activity and therefore favors H_2 formation under rich conditions [79–81] which facilitates catalyst regeneration. The OSC test includes a lean phase that oxygen is stored on ceria, 60 seconds, which is followed by a rich phase, 30 seconds, in which the reductant CO will reduce the stored oxygen and cleans-off the surface. The test is repeated for 30 cycles at different temperature levels. It is worth noting that before each constant temperature experiment, the sample was regenerated with H_2 at 550°C. The inlet feed composition based on volume is reported in Table 9.

Table 9. Inlet gas composition for OSC tests in volume basis for LNT case study #1

Species	Lean Mixture	Rich Mixture
CO[ppm]	0	10000
O_2 [%]	10	0
CO_2 [%]	5	5
H_2O [%]	5	5
N_2	Balance	Balance

3.2.2.2 NO_x Storage and Reduction (NSR)

NO_x adsorption/desorption and its reduction are characterized by means of NSR experiments which is composed of a lean phase in which NO_x is stored on barium sites. Due to variation of NO_x storage capacity with temperature, depending on the temperature level the duration of lean phase varies, such that full saturation of the component is achieved. Therefore, longer exposure times, up to 45 minutes, at lower temperatures and shorter exposure times, as short as 5 minutes, are adopted.

At the end of the storage steps, the NO and O_2 feedings were shut off and the catalyst was either allowed to isothermally desorb the stored NO_x, or it was exposed to a reductant to characterize the kinetics of NO_x release and reduction injecting different reductants, H_2, CO and C_3H_6 (representative of HCs), separately. The inlet gas feed is reported in Table 10 in volume basis. It is worth mentioning that the reductant concentrations were selected such that NO_x reduction potential constant is held constant, i.e. 111 ppm of C_3H_6 can reduce the same quantity of NO_x as 1000 ppm H_2 based on reaction stoichiometries.

Table 10. Inlet gas composition for NO_x reduction experiments in volume basis

Species	Lean	Rich, H_2	Rich, CO	Rich, HC
Reductant [ppm]	0	1000	1000	111
O_2 [%]	10	0	0	0
CO_2 [%]	5	5	5	5
H_2O [%]	5	5	5	5
NO [ppm]	287	0	0	0
NO_2 [ppm]	13	0	0	0
N_2	Balance	Balance	Balance	Balance

3.2.3 Kinetic model development and calibration guideline

A global reaction model comprised of three parts was derived for this study: oxygen storage and reduction, NO_x storage, and reduction of stored NO_x. The specific reaction rates or the turnover number rate (R_i) is expressed in units of mol/mol-site/sec, where mol-site is the active site density participating in the reaction. There are five total sites participating in the reaction: ceria, three different barium sites, and Platinum Group Metals (PGM). A PGM site density of 2 mol/m^3 was chosen based on the PGM loading, Pt/Pd/Rh ratio, and assuming a 10% dispersion, and the pre-exponent multipliers for PGM reactions were calibrated around this value. The other site densities were calibrated in tandem with the pre-exponent multipliers to match measurement data. Unless otherwise noted, all rates were assumed to be first order with respect to each reactant concentration. The Arrhenius expression was chosen for the form of the kinetic rates, Equation 7.

The calibration was largely performed manually and with Arrhenius plots, although at times an objective function was constructed to calculate the cumulative error over time between measurement and model prediction, which was then minimized with an optimizer. The calibration is started from storage experiments. Considering that the experiments include several isothermal steps, kinetic parameters can be obtained using Arrhenius approach. Therefore, prior to explanation of step by step calibration guideline, Arrhenius approach is described.

3.2.3.1 Arrhenius Approach for finding kinetic parameters

The Arrhenius approach can be implemented when calibrating several cases in which in each case the inlet temperature is constant. Considering the Arrhenius expression, Equation 7, in each case when the temperature is constant the reaction constant k_i remains unchanged. As a result, each isothermal case can be calibrated separately without taking into account the activation energy; hence, for each temperature step a constant number for k_i is obtained and a plot of $\ln(k_i)$ as a function of $\frac{1}{T}$ can be made using the calibrated points.

Considering Equation 19, by fitting a line passing through the datasets, the pre-exponent multiplier and activation energy can be calculated as shown in Figure 21.

$$Ln(k_i) = Ln(A_i) - \frac{E_{a,i}}{R} \times \frac{1}{T} \tag{19}$$

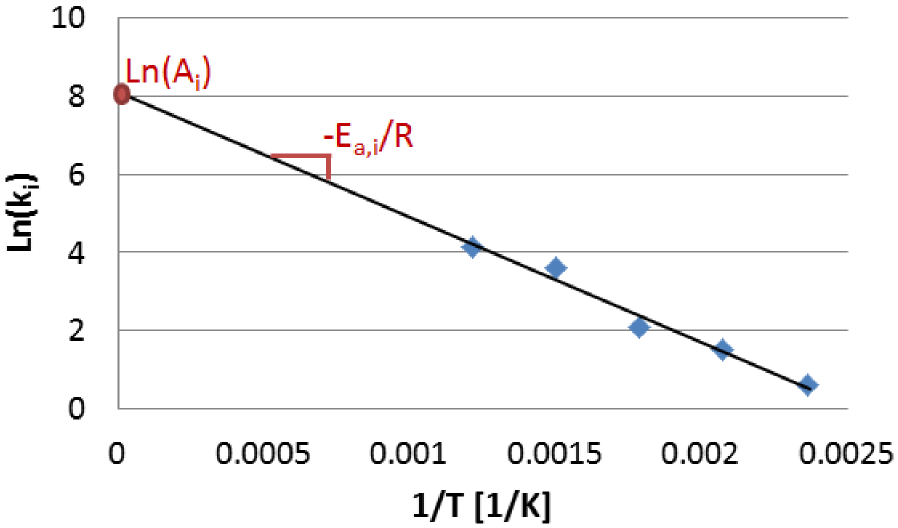

Figure 21. Arrhenius plot for finding pre-exponent multiplier and activation energy

3.2.3.2 Oxygen Storage and Reduction

The reaction model and optimized kinetic parameters of the OSC test includes Water Gas Shift (WGS) reaction on the precious metal, storage of oxygen and its reduction via CO, H_2 and C_3H_6 on ceria sites, as reported in Table 11 and Table 12, respectively:

Table 11. WGS and oxygen storage and reduction reactions for LNT case study #1

#	Reaction	Rate Expression
1	$H_2O + CO \xleftrightarrow{K_{eq,WGS}} CO_2 + H_2$	$r_1 = \dfrac{k_1 C_{CO} C_{H_2O} - \dfrac{C_{CO_2} C_{H_2}}{K_{eq,WGS}}}{G_1}$
2	$Ce_2O_3 + 0.5O_2 \rightarrow 2CeO_2$	$r_2 = \dfrac{k_2 C_{O_2}(\theta_{Ce_2O_3}^{eq} - \theta_{Ce_2O_3})}{G_2}$
3	$2CeO_2 + CO \rightarrow Ce_2O_3 + CO_2$	$r_3 = k_3 C_{CO} \theta_{CeO_2}$
4	$2CeO_2 + H_2 \rightarrow Ce_2O_3 + H_2O$	$r_4 = k_4 C_{H_2} \theta_{CeO_2}$
5	$2CeO_2 + \frac{1}{9}C_3H_6 \rightarrow Ce_2O_3 + \frac{1}{3}\ H_2O + \frac{1}{3}CO_2$	$r_5 = k_5 C_{C_3H_6} \theta_{CeO_2}$

$$G_1 = \left(1 + 1.8\exp\left(\frac{487}{T}\right) C_{CO} + 275\exp\left(\frac{-215}{T}\right) C_{C_3H_6}\right)^2 \left(1 + 0.00061\exp\left(\frac{9715}{T}\right) C_{CO}^2 C_{C_3H_6}^2\right)\left(1 + 5.55E6\exp\left(\frac{-6206.9}{T}\right) C_{NO}\right)$$

$$G_2 = 1 + 1E12\exp\left(\frac{-14000}{T}\right) C_{NO}$$

Table 12. Kinetic parameters obtained for OSC characterization of LNT case study #1

#	Pre-Exponent Multiplier	Activation Energy (J/mol)
1	$3.24E6$	61000
2	0.1	0
3	3.2	$1800(1 - 0.9\theta_{CeO_2})$
4	12.6	$2900(1 - 0.7\theta_{CeO_2})$
5	0.06	$1800(1 - 0.9\theta_{CeO_2})$

The model was developed starting from calibration of WGS, Reaction #1. Water gas shift equilibrium constant is obtained according to thermodynamics using Gibbs free energy, $K_{eq,WGS} = Aexp\left(-\frac{\Delta G}{RT}\right)$, in which the change in Gibbs free energy of the reaction can be considered a quadratic function of temperature [31], Equation 20.

$$K_{eq,WGS} = exp\left(-\frac{(-41000 + 44.2T - 0.0056T^2)}{RT}\right) \tag{20}$$

The reaction rate of WGS can be estimated by Equation 21:

$$r_1 = \boldsymbol{A_1}\exp(-\frac{\boldsymbol{E_{a1}}}{RT})\frac{C_{CO}C_{H_2O} - \frac{C_{CO_2}C_{H_2O}}{K_{eq,WGS}}}{G_1} \tag{21}$$

It should be noted that all the reactions taking place on the precious metal are inhibited by Voltz type inhibition functions (named G_1), Equation 22, which consider the effect of NO, CO and C_3H_6 competition.

$$\begin{aligned} G_1 = &\left(1 + A_{G1,1}exp\left(\frac{-Ta_{G1,1}}{T}\right)C_{CO} + A_{G1,2}exp\left(-\frac{Ta_{G1,2}}{T}\right)C_{C_3H_6}\right)^2 \\ &\times\left(1 + A_{G1,3}exp\left(-\frac{Ta_{G1,3}}{T}\right)C_{CO}^2C_{C_3H_6}^2\right) \\ &\times\left(1 + A_{G1,4}exp\left(-\frac{Ta_{G1,4}}{T}\right)C_{NO}\right) \end{aligned} \tag{22}$$

In this stage preliminary values found in the literature can be used for the Voltz type inhibition function and can be further modified if required.

The reaction parameters in this step include the pre-exponent multiplier $\boldsymbol{A_1}$ and the activation energy $\boldsymbol{E_{a1}}$. In order to find the optimized calibration parameters, Arrhenius approach, resulting in Figure 22, is implemented starting from the lowest temperature and moving step to step to higher temperatures with the goal to match the steady amount of H_2 during the regeneration (O_2 reduction) phase during the rich duration at 286°C and 393°C, since at the lower temperatures negligible H_2 is produced, and the reaction is expected to be at or near thermodynamic equilibrium at 550°C, Figure 23.

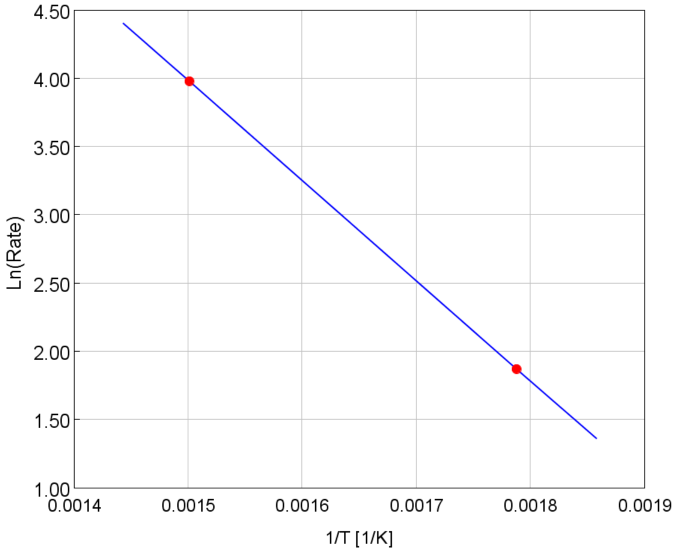

Figure 22. Arrhenius plot for WGS calibration, Linear fit: ln(Rate) = -7336.6(1/T) +14.99

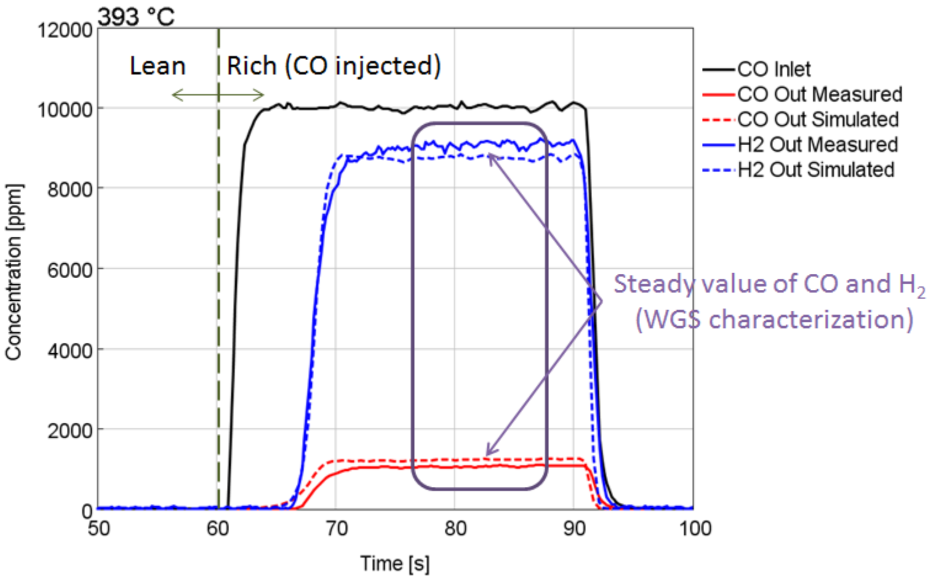

Figure 23. Calibration of OSC experiment considering water gas shift reaction

In order to calibrate the oxygen storage and reduction reactions, it is required to compute the oxygen storage capacity. The measured CO and H_2 outlet fractions for one cycle of the oxygen storage and reduction experiments are shown in Figure 24. Inlet CO fraction is also included; the time between the beginning of the inlet CO feed and when CO and H_2 exit the reactor indicates the amount of stored O_2. This dead time during which no CO or H_2 break through increases monotonically as temperature increases. Further, because the rate of the reduction reactions between CO/H_2 and stored oxygen are expected to increase with increasing temperature, the trend between dead time and temperature indicates the O_2 storage capacity increases with increasing temperature. This observation was also reported in [82] where zirconia containing oxygen storage materials have an exponential growth in storage above 300 °C, Figure 25.

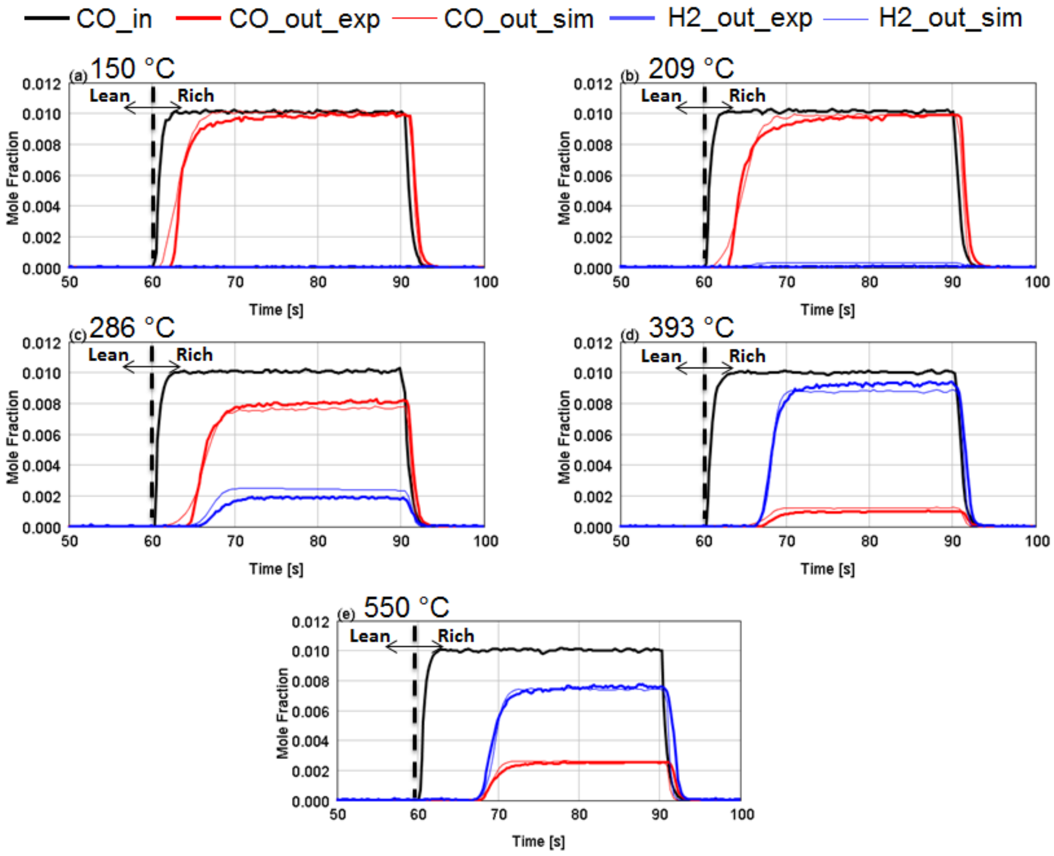

Figure 24. Measured CO (red) and H_2 (blue) outlet concentration for one cycle of the oxygen storage and reduction experiments at (a) 150°C, (b) 209°C, (c) 286°C, (d) 393°C, (e) 550°C.

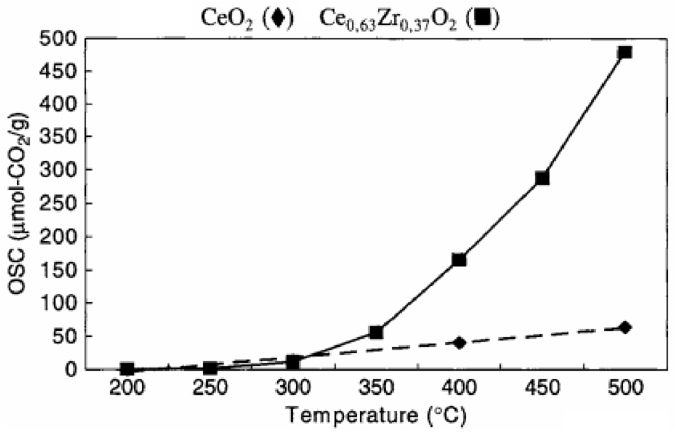

Figure 25. Evolution of oxygen storage [82]

Therefore, the data in Figure 24 was analyzed to determine the O_2 storage capacity, which was calculated by considering a mole balance on the reactor starting with the introduction of the rich feed and ending when steady-state had been reached. The number of stored O_2 moles was calculated by Equation 23:

$$n_{O2,stored} = \frac{1}{2} \int_{t_{start}}^{t_{end}} \left(\dot{n}_{CO,in} - (\dot{n}_{CO,out} + \dot{n}_{H_2,out})\right) dt \tag{23}$$

In which

- $n_{O_2,stored}$ is the number of stored oxygen moles
- $\dot{n}_{CO,in}$ and $\dot{n}_{CO,out}$ is the molar flow rate of inlet and outlet CO, respectively [mole/s]
- $\dot{n}_{H_2,out}$ is the molar flow rate of outlet H_2 [mole/s]

The factor of 1/2 comes from the stoichiometry of the CO and H_2 reduction reactions. The calculated results are depicted in Figure 26.

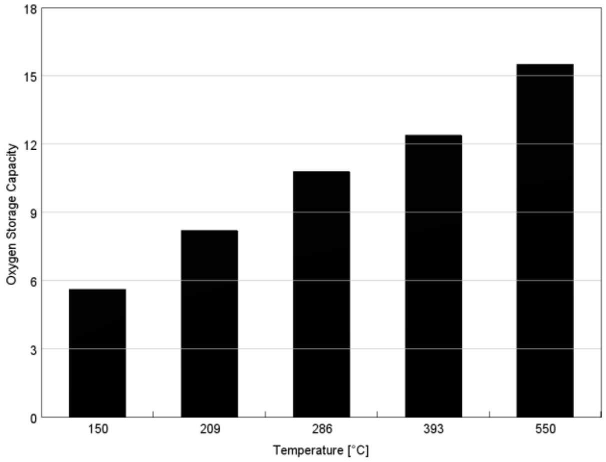

Figure 26. Calculated O_2 storage capacity in moles per unit reactor volume

In order to account for the increasing O_2 storage capacity with increasing temperature, temperature dependence of the OSC was implemented by using a maximum equilibrium coverage equation. When the data in Figure 26 is converted to number of necessary storage sites and divided by a single constant site density, the result is an equilibrium coverage. The single constant site density was eventually calibrated to the measured data in Figure 24, and the resulting temperature-dependent equilibrium coverage equation took the form of Equation 24. In addition, the expression was implemented in the model to disallow the adsorption rate from being negative, thereby neglecting any potential O_2 desorption.

$$\theta_{Ce_2O_3}^{eq} = 1 - \frac{339}{T} \tag{24}$$

The form for this equation was chosen after plotting the O_2 storage capacity vs. 1/T, as shown in Figure 27. Plotting the data this way and using a linear fit is useful because as temperature increases indefinitely, the storage capacity reaches a limit as indicated by the y-intercept.

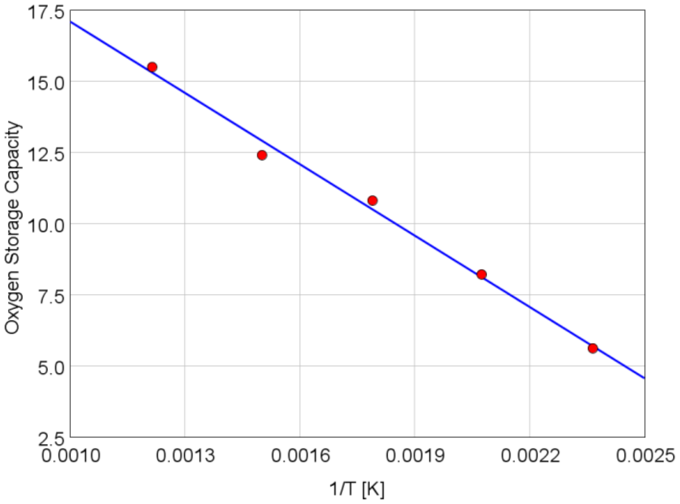

Figure 27. Oxygen storage capacity [mole] per unit reactor volume vs. 1/T [K], with linear fit y = -9839/T + 25.4

Further, because oxygen was fed at an excess concentration of 10%, it was not possible to use the measured concentration data to extract kinetic information for the O_2 adsorption reaction. Instead of calibrating it, its non-activated rate was set to be sufficiently fast to avoid imposing an unnecessary burden on the solver to satisfy the O_2 experiments and the NO_x reduction calibration.

The O_2 reduction reactions, ceria site density, and constant found in Equation 24 were calibrated according to the breakthrough of the CO and H_2 concentration during the lean (O_2 storage) phase at all temperatures as shown in Figure 28. Although O_2 reduction with C_3H_6 was not tested, this reaction would be needed for the NO_x reduction model, so its rate constants were originally set equal to those of CO reduction, but the pre-exponent multiplier was later decreased to accommodate the NO_x reduction model development. The resulting model shows adequate CO and H_2 reduction of stored O_2 in Figure 24.

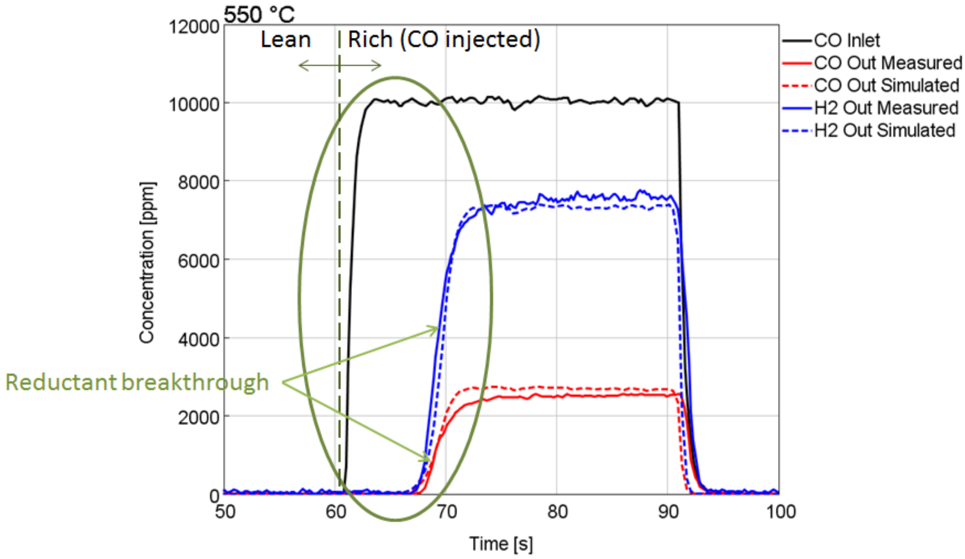

Figure 28. Calibration of OSC test considering oxygen storage and reduction over ceria

3.2.3.3 NO$_x$ Storage

As previously discussed in Section 3.1 the complex NO$_x$ storage phenomena cannot be modeled using a single storage site due to their complex kinetic behavior non-monotonic relationship between measured NO$_x$ storage capacity and temperature. Accordingly, a three-site model is developed in this study which is consistent with the model proposed by Chaugule et al. [69].

Figure 29 shows the NO and NO$_2$ profiles for NO$_x$ storage experiments with 300 ppm NO$_2$ and 10% O$_2$ in the feed gas. The NO$_2$ and O$_2$ were shut-off at 30 minutes for 150°C and 45 minutes for 209°C. It can be seen that the NO$_x$ storage capacity has not been saturated even after 45 minutes because the outlet NO and NO$_2$ concentrations are still increasing. The plots also include a curve for calculated NO that would result if all NO$_2$ were to store via the single step disproportionation reaction. The theoretical NO curve shows that at 150°C, initial NO storage is lower than the experimental one during the first 10 minutes, and as time progresses, the actual NO outlet concentration approaches the theoretical one. At 209°C, the trend is similar, although the theoretical NO profile meets the actual one much earlier in the experiment and matches it for the remainder of the lean duration. These results confirm the importance of the disproportionation reaction as the dominant pathway for NO$_2$ storage on a Ba site with larger density. Additionally, at both temperatures, the time at which the theoretical NO curve does not match the actual one indicates NO has an appreciable storage pathway that prevents NO$_x$ breakthrough for the first 2-3 minutes, during which all NO$_x$ is stored and none escapes the outlet of the reactor. This suggests that the steady state balance between the three sites varies with temperature. The 150°C results also show the actual NO outlet concentration is greater than the theoretical curve. The main implication of this observation is that the disproportionation reaction has to be modeled using the three individual steps of Equations 15, 16 and 17 instead of the overall reaction Equation 18 to sufficiently match this portion of the NO outlet concentration. Finally, insignificant desorption occurs when the inlet NO_x is shut off, which suggests formation of stable Ba-nitrates even at these lower temperatures.

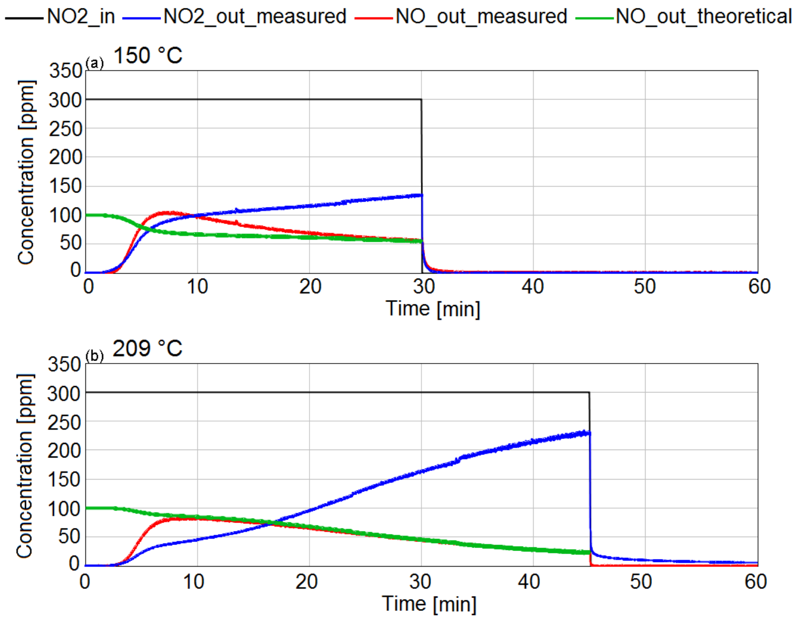

Figure 29. Measured NO and NO_2 outlet concentrations for NO_x adsorption and desorption with 300 ppm NO_2 in the feed gas, at 150°C (a) and 209°C (b). Green line shows the theoretical NO outlet concentration if all NO_2 stores via the single step disproportionation reaction

Figure 30 shows the measured NO and NO_2 profiles for NO_x storage experiments with 300 ppm NO, 10% O_2, 5% CO_2, 5% H_2O and balanced N_2. After storage sites are saturated with NO_x, NO and O_2 flows are stopped allowing to better characterization of isothermal NO_x desorption; these times occur at 30 minutes for 150°C, 45 minutes for 209°C, , 30 minutes for 286°C, 15 minutes for 393°C, and 5 minutes for 550°C. The experiment at 209°C was run for the longest duration; even after 45 minutes, the profiles have not reached steady-state by the end of the lean feed duration. The profiles at the other four temperatures appear to reach steady-state before the inlet NO is shut off. The plots in Figure 30 suggest a complex system of NO_x storage. At 150°C both NO and NO_2 profiles reach steady-state after 8-10 minutes, and moderate desorption profiles from both species are seen after NO is shut off, suggesting both species store with low storage capacity to the same relatively small capacity site at this lowest temperature. At 209°C, two storage rates are seen in both the NO and NO_2 profiles as the slopes of outlet NO and NO_2 concentration change around 5-7 minutes. These profiles suggest storage on two different sites at two different rates. The profiles also suggest that both NO and NO_2 continue to store on this larger capacity site, albeit at a relatively slow rate, until the end of the lean feed duration. In addition, the storage to the smaller capacity site in the first 5-7 minutes is likely the same site on which storage occurs at 150°C. This hypothesis is supported because the breakout time is similar at both temperatures, although the time is somewhat longer at 209°C. Furthermore, because the slope changes around 5-7 minutes at 209°C occur sooner than the saturation time of 7-10 minutes at 150°C, less NO_x can store at this smaller site at 209°C compared to 150°C. This observation suggests either the desorption rate at 209°C is larger than at 150°C, a mechanism slows the adsorption process, or the stored species are weaker at 150°C and stronger at 209°C. Given that no desorption profiles appear at 209°C, the first hypothesis is unlikely.

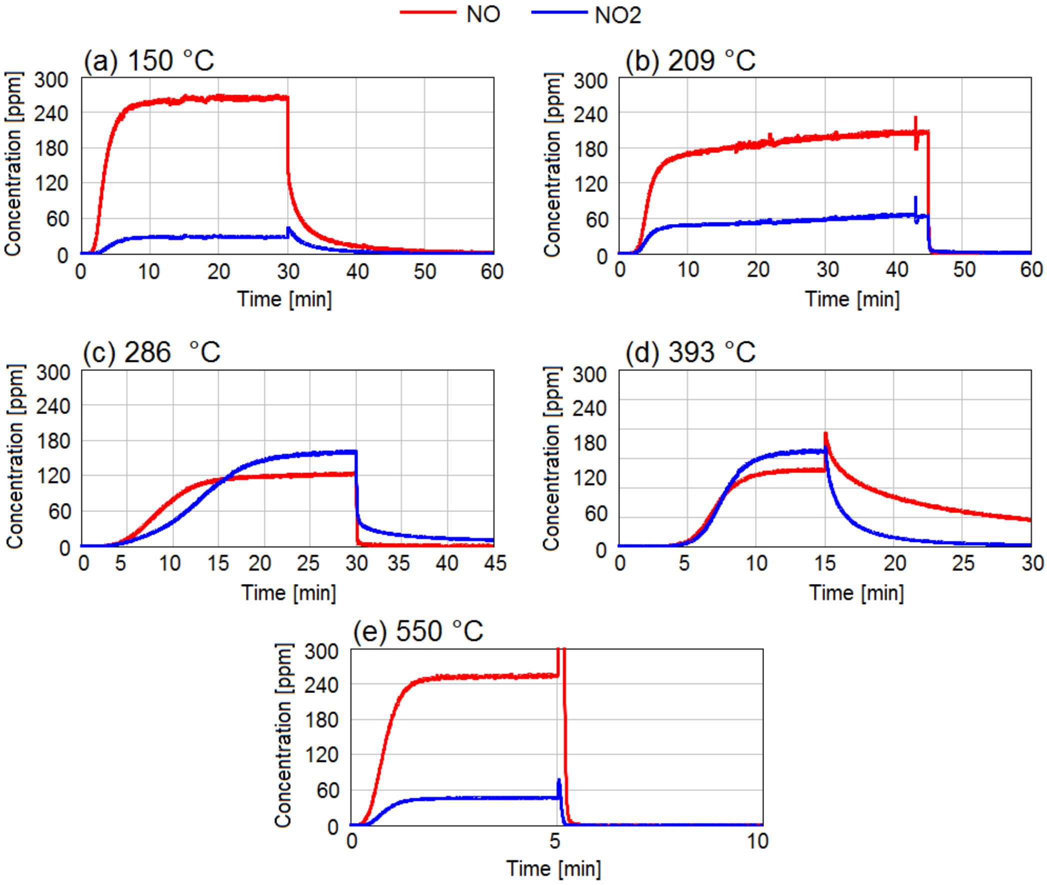

Figure 30. Measured NO (red) and NO_2 (blue) profiles from storage and release experiments with 300 ppm NO, 10% O_2 in the feed gas at (a) 150°C, (b) 209°C, (c) 286°C, (d) 393°C, and (e) 550°C. Not shown in (e) is the NO profile peak of 2800 ppm.

Moreover, at 286°C, the delay in the profiles reaching steady-state shows a large increase in the NO_x storage capacity. Figure 30-c suggests NO and NO_2 storing to two different sites as the change in their profile slopes occur at different times, although their breakout times are the same. It can also be seen that, just prior to NO shut off, the rate of increase in the outlet concentration profiles may still be slowly increasing. The sum of NO and NO_2 concentrations at the end of the storage duration is 290 ppm; it's unknown whether both species will increase further so their sum is equal to the inlet concentration value of 300 ppm or whether both have reached steady-state and 10 ppm is converted. 286°C shows reappearance of desorption profile for NO_2 after NO is shut off, whereas NO shows no desorption.

At 393°C, NO and NO_2 breakout times are the same and their profiles progress to steady-state in tandem. Given that they reach steady-state much sooner than what is shown at 286°C, and given the large desorption profiles after NO is shut off, storage capacity at this temperature is degraded by larger desorption rates. A similar trend is seen at 550°C in Figure 30-e, where the storage capacity is much less than at 393°C, and the strong increase in outlet NO concentration when inlet NO is shut off indicates strong desorption rates.

Data in Figure 29 and Figure 30 were used to calculate the NO_x storage capacity using Equation 25, where t_{end} represents the end of the lean duration, and those results are reported in Figure 31. Consistent with other studies having reported LNT NO_x storage when feeding NO [70,74], the storage capacity vs. temperature trend shows a bell shape with the largest storage capacity occurring in the middle temperature range, with less storage occurring at 550°C than at 150°C. It can also be seen that the storage capacity is more than three times higher at 150°C when NO_2 is fed to the reactor compared to feeding NO. The largest storage capacity occurs at 209°C when feeding NO_2.

$$n_{NO_x,stored} = \int_0^{t_{end}} \left(\dot{n}_{NO_x,in} - \dot{n}_{NO_x,out}\right) dt \tag{25}$$

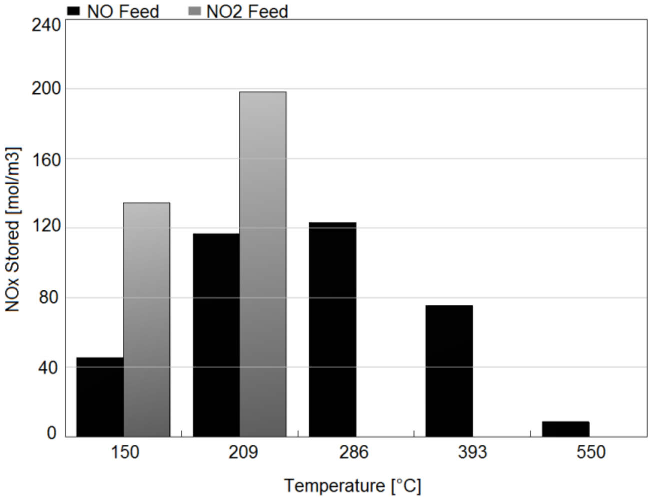

Figure 31. NO_x stored per unit reactor volume for experiments fed with NO (black) and NO_2 (gray).

The NO_x storage model was first developed by considering NO oxidation. Many studies have modeled NO oxidation using detailed kinetics where the adsorption and desorption of NO, O_2, and NO_2 on PGM sites are modeled. Because the objective of this study was to develop a computationally faster running global reaction mechanism, reversible NO oxidation is treated as reaction on PGM sites, where an equilibrium constant was calculated from thermodynamic equilibrium based on the Gibbs free energy, as defined in Equation 26.

$$K_{eq,NO} = 1.5 \times 10^{-4} \exp\left(\frac{6864}{T}\right) \tag{26}$$

The NO oxidation rate constants were calibrated to achieve the NO_2/NO_x ratios that were achieved at or near steady-state at the low and mid temperatures for the experiments with NO in the feed. Those NO_2/NO_x ratios are shown in Figure 32, which also includes the equilibrium ratio based on the equilibrium constant and the inlet O_2 volume fraction of 10%. It is clear that the NO_2/NO_x ratios at 393°C and 550°C are at chemical equilibrium, which is why the lower temperatures were used to calibrate the NO oxidation reaction.

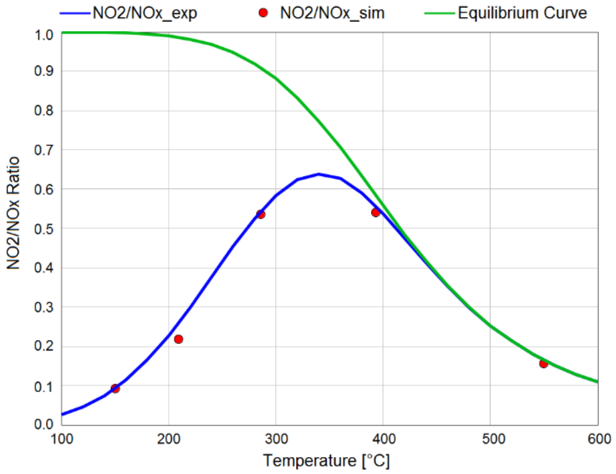

Figure 32. Steady-state NO_2/NO_x ratios from experiments with NO inlet feed (red) compared with NO oxidation model prediction (blue), and equilibrium (green).

The NO_x storage model and optimized kinetic parameters are contained in Table 13 and Table 14 which consists of adsorption and desorption on three different barium sites. Although it is possible that the NO_x storage at the lowest temperature includes storage to ceria [83], for the purpose of developing a predictive model, the actual components on which NO_x stores are inconsequential. For this reason, all three vacant barium coverages are modeled in the form BaO, and the three sites are differentiated by Ba^{I}, Ba^{II}, and Ba^{III}. The calibrated barium site densities are given in Table 15. In this step, since the number of reactions is higher with respect to OSC test, it is more difficult to decouple the effect of each reaction; hence, the reactions are not calibrated one by one, but a group of reactions should be calibrated at the same time. It is worth noting that primarily a more complex kinetic scheme was considered which included a higher number of reactions (more than 50) and after a sensitivity analysis based on rate comparison the final reduced model, presented in this section, was developed which includes 40 reactions.

Model calibrated predictions for NO and NO_2 for the seven storage experiments are shown in Figure 33. Reactions with barium site Ba^I have the largest site density and uses the single-step disproportionation reaction to match the data with NO_2 fed to the reactor. It may be of interest that using the 3-step disproportion pathway for storage on Ba^I allows a better match to the data with NO_2 fed to the reactor, but the single step pathway was selected to reduce the complexity of the mechanism. Storage on this site is minimal at 150°C when NO is fed to the reactor, but becomes more significant at 209°C and 286°C when the NO oxidation reaction creates more NO_2. NO storage on Ba^I is also needed to prevent initial breakthrough during the runs with NO_2 feed. Storage on Ba^{II} characterizes the unstable storage of NO as barium nitrite at 150°C, which strongly desorbs when inlet NO is shut off. Barium nitrites on this site transition to barium nitrates at 209°C which are more stable and do not desorb at this temperature.

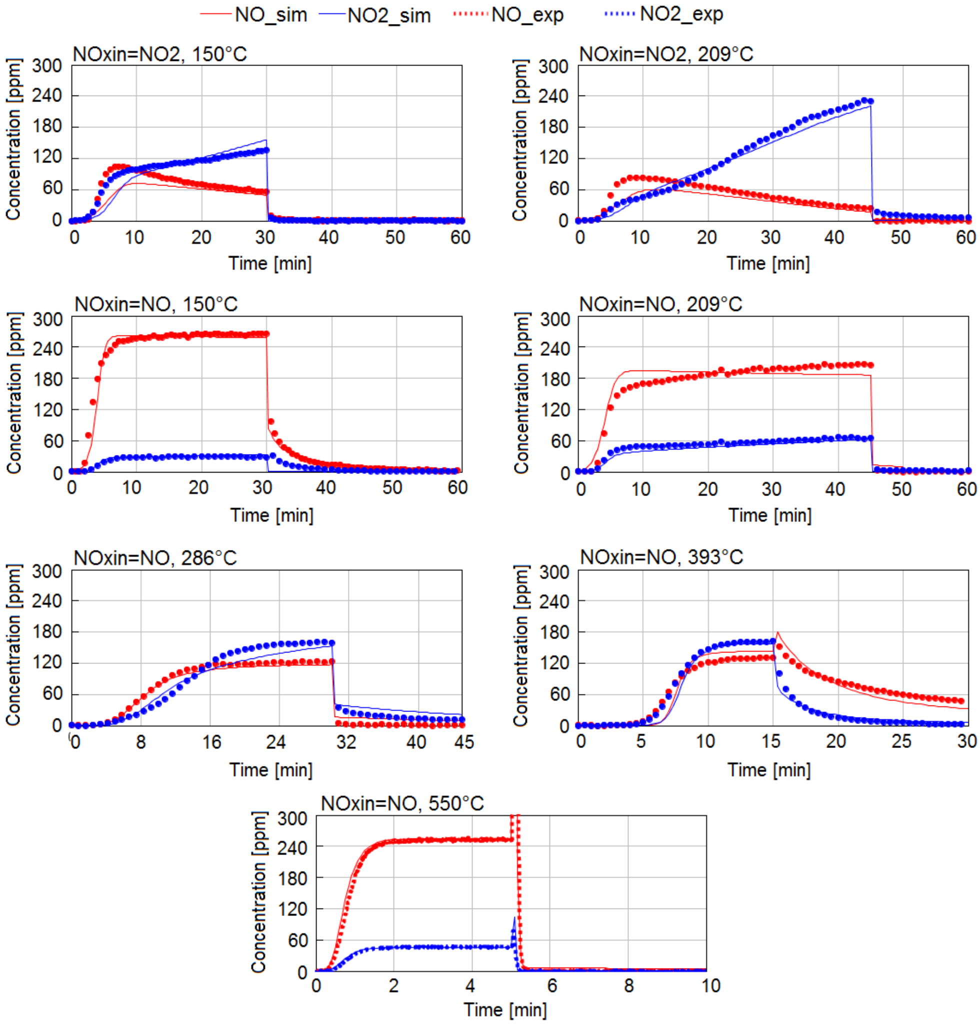

Figure 33. Model predictions (solid lines) of NO (red) and NO_2 (blue) outlet concentrations during NO_x storage compared to measurement (dotted lines) for LNT case study #1.

At 286°C, the storage capacity increases and the data in Figure 33 suggest the introduction of a third site, represented by Ba^{III}. However, a mechanism was needed to account for the increased storage at this temperature compared to the lower temperatures. The data suggests that storage to this third site might be inhibited by the presence of NO at the lower temperatures, thereby preventing a visible effect. For this reason, NO and NO_2 storage to this third site were modeled with an NO inhibition term with Arrhenius form which appears to be necessary to describe the competition between this site and Ba^{I} site for NO. The inhibition term can be assumed as Equation 27, in which parameter *factor* has an Arrhenius form:

$$G = 1 + [factor]C_{NO} \tag{27}$$

In order to remove the effect of the mentioned reaction on temperatures lower than 286 °C, it is required to find the “minimum” value for *factor* (as a constant) such that the lower temperature cases results are un-affected by the introduction of the mentioned reaction. It is stated “minimum”; since as parameter *factor* becomes higher the inhibition term tends to infinity; thus resulting in a zero reaction rate. Therefore, for a better calibration, it is required to find the smallest value. Afterwards, the “maximum” value for parameter *factor* is found such that at temperatures higher than 286 °C, for example 393 ℃, the experimental data are matched with predictions. Finally, the Arrhenius plot is sketched for 193 and 247 ℃ considering the corresponding values for *factor* and the pre-exponent multiplier and the activation temperature is found for the inhibition function.

The summary of the mentioned calibration procedure for this example is expressed in Figure 34.

Figure 34. Summary of calibration of an inhibition term for an example in which a reaction should be considered for temperatures higher than 286 °C and should be deactivated for lower temperatures (temperature steps as: 150, 209, 286, 393 and 550 °C)

Table 13. NO oxidation and NO$_x$ storage reactions for LNT case study #1

#	Reaction	Rate Expression
6	$NO + 0.5O_2 \rightarrow NO_2$	$r_6 = k_6 \frac{C_{NO}C_{O_2}^{0.5} - \frac{C_{NO_2}}{K_{eq,NO}}}{G_1}$
7	$Ba^IO + 3NO_2 \rightarrow Ba^I(NO_3)_2 + NO$	$r_7 = \frac{k_7 C_{NO_2}\theta_{Ba^IO}}{G_3}$
8	$Ba^I(NO_3)_2 \rightarrow Ba^IO + 2NO_2 + 0.5O_2$	$r_8 = k_8\theta_{Ba^I(NO_3)_2}$
9	$Ba^{II}O + 3NO_2 \rightarrow Ba^{II}(NO_3)_2 + NO$	$r_9 = k_9 C_{NO_2}\theta_{Ba^{II}O}$
10	$Ba^{II}O + 2NO + 0.5O_2 \rightarrow Ba^{II}(NO_2)_2$	$r_{10} = k_{10}C_{NO}C_{O_2}\theta_{Ba^{II}O}$
11	$Ba^{II}(NO_2)_2 \rightarrow Ba^{II}O + 2NO + 0.5O_2$	$r_{11} = k_{11}\theta_{Ba^{II}(NO_2)_2}$
12	$Ba^{II}(NO_2)_2 + O_2 \rightarrow Ba^{II}(NO_3)_2$	$r_{12} = k_{12}C_{O_2}\theta_{Ba^{II}(NO_2)_2}$
13	$Ba^{II}(NO_3)_2 \rightarrow Ba^{II}O + 2NO_2 + 0.5O_2$	$r_{13} = k_{13}\theta_{Ba^{II}(NO_3)_2}$
14	$Ba^{III}O + 2NO + 1.5O_2 \rightarrow Ba^{III}(NO_3)_2$	$r_{14} = \frac{k_{14}C_{NO}C_{O_2}\theta_{Ba^{III}O}}{G_4}$
15	$Ba^{III}O + 2NO_2 + 0.5O_2 \rightarrow Ba^{III}(NO_3)_2$	$r_{15} = \frac{k_{15}C_{NO_2}C_{O_2}\theta_{Ba^{III}O}}{G_5}$
16	$Ba^{III}(NO_3)_2 \rightarrow Ba^{III}O + 2NO + 1.5O_2$	$r_{16} = k_{16}\theta_{Ba^{III}(NO_3)_2}$
17	$Ba^{III}(NO_3)_2 \rightarrow Ba^{III}O + 2NO_2 + 0.5O_2$	$r_{17} = k_{17}\theta_{Ba^{III}(NO_3)_2}$

$$G_3 = 1 + 1.19\times10^{-20}\exp(22121/T)\,C_{NO}$$

$$G_4 = 1 + 2.26\times10^{-4}\exp(10190/T)\,C_{NO}$$

$$G_5 = 1 + 9.2\times10^{-13}\exp(20740/T)\,C_{NO}$$

Table 14. Kinetic parameters obtained for NO oxidation and NO_x storage reactions of LNT case study #1

#	Pre-exponent Multiplier	Activation Energy [J/mol]
6	5.25E4	39400
7	0.2	0
8	5.83E14	190100
9	3.1	0
10	1.2	0
11	0.032	$21400(1 - 0.7\theta_{Ba^{II}(NO_2)_2})$
12	1480	66200
13	2E12	185000
14	15	0
15	12	0
16	1.12E16	257000
17	1.4E7	133000

Table 15. Site densities used in the turnover number based reaction model for LNT case study #1

Site	Site Density [mol/m^3]
PGM	2.0
Ce	109
Ba^{I}	60
Ba^{II}	14
Ba^{III}	16

The final NO_x storage mechanism developed for this study is illustrated in Figure 35. In summary, three barium sites with different site densities are required to describe the behaviour of the system regarding NO_x storage at different temperature levels. Specifically, the site densities of Ba^{I} and Ba^{II} in addition to the reactions taking place on them are characterized focusing on the low temperature experiments, 150 and 209°C. Afterwards, site density of Ba^{III} and the kinetic parameters of the reactions taking place on Ba^{III} are calibrated according to medium to high temperature measurements. In addition, an NO inhibition term is required to be defined and characterized such that the results of lower temperature cases (150 and 209°C) are preserved.

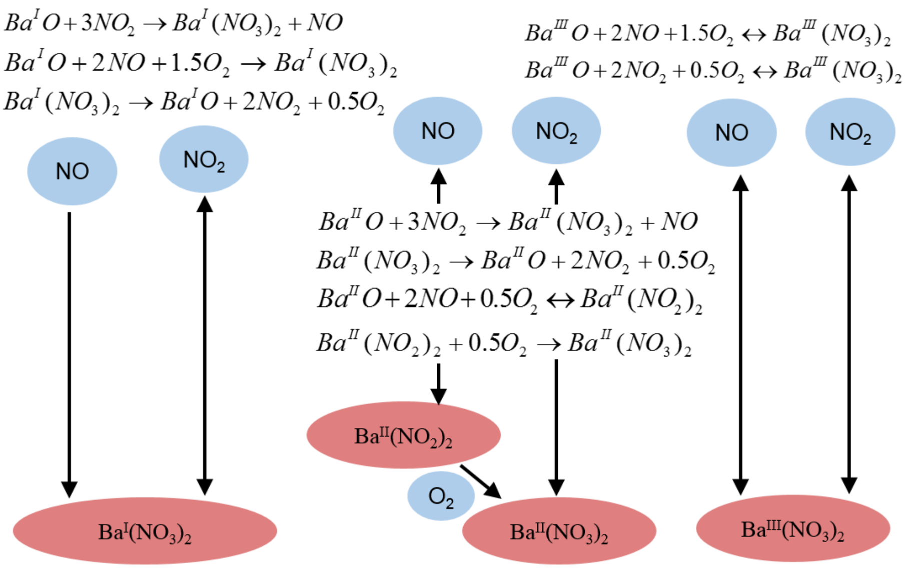

Figure 35. Schematic of NO_x storage sites and pathways developed

3.2.3.4 NO_x Reduction

The lean part of the NO_x reduction experiments is identical to the NO_x storage experiments. However, at the end of the storage phase, one of the reductants (H_2, CO, or C_3H_6) is introduced to recover the storage capacity of the catalyst which was previously saturated with stored NO_x in the form of nitrates and nitrites during the lean phase [62,84].

N_2O and NH_3 are by-products of the NO_x regeneration [76,85,86]. There are several global NO_x reduction mechanisms reported in the literature that include different combinations of reductants and potential product species. Güthenke et al. [72] used a global kinetic model in which the reductant reacted with stored NO_x and produced N_2 and gaseous NO_x which could be further reduced to N_2 over the precious metal. Kočí et al. [70,74] developed another global kinetic model in which NH_3 was generated primarily by reduction of stored NO_x with H_2 and was further acting as an active intermediate to reduce the remaining stored or released NO_x, which could explain the delayed ammonia release [87]. The previous models did not give any information about the nitrous oxide production, while in a more advanced model, Kočí et al. [75] proposed a reaction step in which N_2O was another byproduct of reaction of NH_3 with stored NO_x. Although ammonia oxidation through stored oxygen could also lead to nitrous oxide formation, it was demonstrated that ammonia oxidation is more selective to nitrogen formation [88]. This pathway in [88] gives the possibility to predict nitrous oxide production before ammonia breakthrough [75,76,89], which is the aim of the model proposed in the present study. An example of the complex evolution of products during regeneration is shown in Figure 36, which includes the measured outlet concentrations of NO_x, H_2, NH_3 and N_2O at 150 °C when hydrogen is used as the primary reductant. Upon the switch to rich conditions at 1800 seconds, NO and N_2O are released from the catalyst. The outlet concentrations of these species decrease, and eventually NH_3 breakthrough is observed as they drop to zero. Finally, H_2 breaks through as the NH_3 concentration decreases. An accurate regeneration model must capture all of these features.

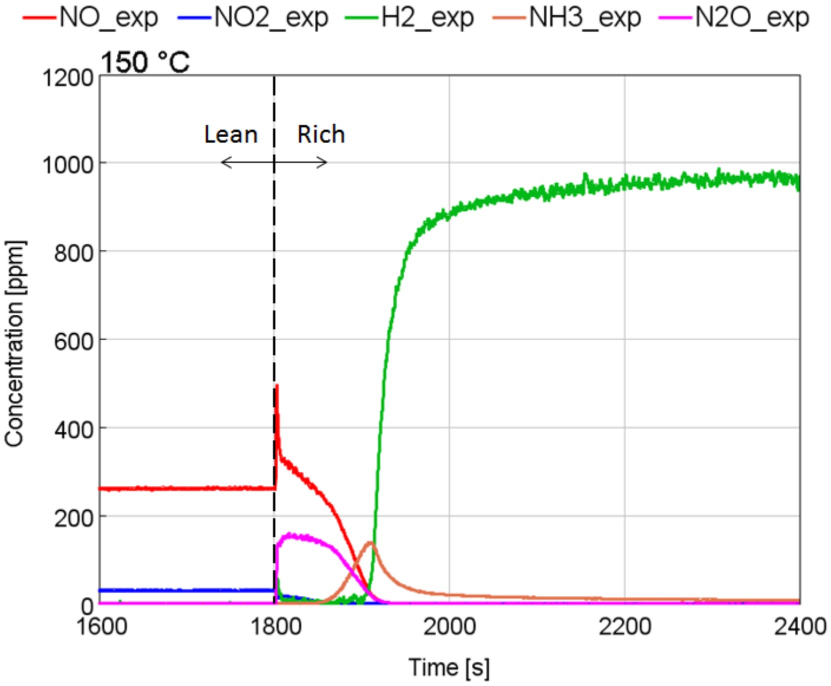

Figure 36. Experimental outlet concentration of NO_x, H_2, NH_3 and N_2O during LNT regeneration by H_2 at 150 °C for LNT case study #1

A NO_x reduction model is presented in Table 16 and Table 17. In the current model reductants (H_2, CO and C_3H_6) react with stored NO_x on the three barium sites and produce gaseous NO or N_2. Furthermore, when H_2 is the primary reductant, ammonia is produced through reduction of barium nitrates with H_2 and acts as a secondary reductant and cleans stored NO_x from barium sites resulting in gaseous NO, N_2 and N_2O. It is important to note that due to the presence of CO_2 and H_2O in the inlet feed, water gas shift and steam reforming reactions are important inclusions to the model.

Table 16. NO_x Reduction reaction on barium sites for LNT case study #1

#	Reaction	Rate Expression
18	$Ba^{II}(NO_3)_2 + \frac{10}{3}NH_3 \rightarrow Ba^{II}O + \frac{8}{3}N_2 + 5H_2O$	$r_{18} = k_{18}C_{NH_3}\theta_{Ba^{II}(NO_3)_2}$
19	$Ba^{I}(NO_3)_2 + 8H_2 \rightarrow Ba^{I}O + 2NH_3 + 5H_2O$	$r_{19} = k_{19}C_{H_2}\theta_{Ba^{I}(NO_3)_2}$
20	$Ba^{II}(NO_2)_2 + 6H_2 \rightarrow Ba^{II}O + 2NH_3 + 3H_2O$	$r_{20} = k_{20}C_{H_2}\theta_{Ba^{II}(NO_2)_2}$
21	$Ba^{III}(NO_3)_2 + 8H_2 \rightarrow Ba^{III}O + 2NH_3 + 5H_2O$	$r_{21} = k_{19}C_{H_2}\theta_{Ba^{III}(NO_3)_2}$
22	$Ba^{II}(NO_2)_2 + NH_3 \rightarrow Ba^{II}O + 1.5N_2O + 1.5H_2O$	$r_{22} = k_{22}C_{NH_3}\theta_{Ba^{II}(NO_2)_2}$
23	$Ba^{II}(NO_2)_2 + \frac{2}{5}NH_3 \rightarrow Ba^{II}O + \frac{12}{5}NO + \frac{3}{5}H_2O$	$r_{23} = k_{23}C_{NH_3}\theta_{Ba^{II}(NO_2)_2}$
24	$Ba^{II}(NO_2)_2 + 2NH_3 \rightarrow Ba^{II}O + 2N_2 + 3H_2O$	$r_{24} = k_{24}C_{NH_3}\theta_{Ba^{II}(NO_2)_2}$
25	$Ba^{III}(NO_3)_2 + \frac{6}{5}NH_3 \rightarrow Ba^{III}O + \frac{16}{5}NO + \frac{9}{5}H_2O$	$r_{25} = k_{25}C_{NH_3}\theta_{Ba^{III}(NO_3)_2}$
26	$Ba^{I}(NO_3)_2 + 5CO \rightarrow Ba^{I}O + 5CO_2 + N_2$	$r_{26} = k_{26}C_{CO}\theta_{Ba^{I}(NO_3)_2}$
27	$Ba^{II}(NO_3)_2 + 5CO \rightarrow Ba^{II}O + 5CO_2 + N_2$	$r_{27} = k_{27}C_{CO}\theta_{Ba^{II}(NO_3)_2}$
28	$Ba^{III}(NO_3)_2 + 5CO \rightarrow Ba^{III}O + 5CO_2 + N_2$	$r_{28} = k_{28}C_{CO}\theta_{Ba^{III}(NO_3)_2}$
29	$Ba^{II}(NO_2)_2 + CO \rightarrow Ba^{II}O + CO_2 + 2NO$	$r_{29} = k_{29}C_{CO}\theta_{Ba^{II}(NO_2)_2}$
30	$Ba^{I}(NO_3)_2 + \frac{5}{9}C_3H_6 \rightarrow Ba^{I}O + \frac{5}{3}CO_2 + \frac{5}{3}H_2O + N_2$	$r_{30} = k_{30}C_{C_3H_6}\theta_{Ba^{I}(NO_3)_2}$
31	$Ba^{I}(NO_3)_2 + \frac{1}{3}C_3H_6 \rightarrow Ba^{I}O + CO_2 + H_2O + 2NO$	$r_{31} = k_{31}C_{C_3H_6}\theta_{Ba^{I}(NO_3)_2}$

32	$Ba^{III}(NO_3)_2+\frac{5}{9}C_3H_6\rightarrow Ba^{III}O+\frac{5}{3}CO_2+\frac{5}{3}H_2O+N_2$	$r_{32}=k_{32}C_{C_3H_6}\theta_{Ba^{III}(NO_3)_2}$
33	$Ba^{III}(NO_3)_2+\frac{1}{3}C_3H_6\rightarrow Ba^{III}O+CO_2+H_2O+2NO$	$r_{33}=k_{33}C_{C_3H_6}\theta_{Ba^{III}(NO_3)_2}$

Table 17. PGM reactions participating in NO_x reduction for LNT case study #1

#	**Reaction**	**Rate Expression**
34	$NH_3+\frac{3}{2}NO\rightarrow\frac{5}{4}N_2+\frac{3}{2}H_2O$	$r_{34}=\frac{k_{34}C_{NH_3}C_{NO}}{G_1}$
35	$CO+NO\rightarrow CO_2+\frac{1}{2}N_2$	$r_{35}=\frac{k_{36}C_{CO}C_{NO}}{G_1}$
36	$NO_2+\frac{4}{3}NH_3\rightarrow\frac{7}{6}N_2+2H_2O$	$r_{36}=\frac{k_{36}C_{NO_2}C_{NH_3}}{G_1}$
37	$CO+\frac{1}{2}NO_2\rightarrow CO_2+\frac{1}{4}N_2$	$r_{37}=\frac{k_{37}C_{CO}C_{NO_2}}{G_1}$
38	$C_3H_6+3H_2O\rightarrow 3CO+6H_2$	$r_{38}=\frac{k_{38}C_{C_3H_6}C_{H_2O}}{G_1}$
39	$C_3H_6+9NO\rightarrow 3CO_2+3H_2O+\frac{9}{2}N_2$	$r_{39}=\frac{k_{39}C_{C_3H_6}C_{NO}}{G_1}$
40	$C_3H_6+18NO\rightarrow 3CO_2+3H_2O+9N_2O$	$r_{40}=\frac{k_{40}C_{C_3H_6}C_{NO}}{G_1}$

The optimized kinetic parametes found through calibration are reported in Table 18.

Table 18. Kinetic parameters for NO_x Reduction reactions of LNT case study #1

#	**Pre-exponent Multiplier**	**Activation Energy [J/mol]**
18	8	3300
19	8.6E8	85590
20	14	2750
21	1.2E8	85590
22	6.2	1980
23	7.95	3300
24	2.4E6	59800
25	1.5E18	206400
26	1.4	19900
27	3896	39700
28	3896	39700
29	7.3	2580
30	3.6	2780
31	2.7E7	67000
32	1.8	2780
33	2.18E16	193500
34	1E16	124500
35	1E10	62300
36	5.7E6	16200
37	1E11	62300
38	6E8	89200
39	3E10	74400
40	56700	16200

The modeling objective was to match the predicted outlet concentrations of NO_x (including NO and NO_2), ammonia, N_2O and reductants with the experimental data during the rich pulse. The results of NO_x reduction experiments considering H_2, CO and C_3H_6 used as primary reductants are shown Figure 37, Figure 38 and Figure 39 respectively. It is worth noting that, for all three reductants, the predicted NO and NO_2 concentrations during regeneration phase matches well with the experimental data.

In detail, NO_x conversion efficiency versus temperature is plotted in Figure 40, which is calculated based on Equation 28.

$$NO_x\ Conversion\ Efficiency = 1 - \frac{\int_{t_{start}}^{t_{end}} \left(\dot{n}_{NO_x,out}\right) dt}{\int_{t_{start}}^{t_{end}} \left(\dot{n}_{NO_x,in}\right) dt} \tag{28}$$

The maximum conversion is observed for intermediate temperatures, between 286 and 393 °C, as reported by several authors [57,74,75]. In addition, it has been found that C_3H_6 is less efficient than CO and H_2 in abating NO_x slip during reduction, which is consistent with the literature findings [90–92]. Furthermore, even when CO and C_3H_6 are used as the primary reductants as in Figure 38 and Figure 39**,** the main share of regeneration is carried out by H_2 as a result of WGS and steam reforming reactions, specifically at higher temperatures where H_2 production is favored. For example, the steady H_2 concentration at 393 °C is around 1000 ppm both for CO and C_3H_6 reductants, as seen in Figure 38 and Figure 39, thus confirming almost complete consumption of primary reductants.

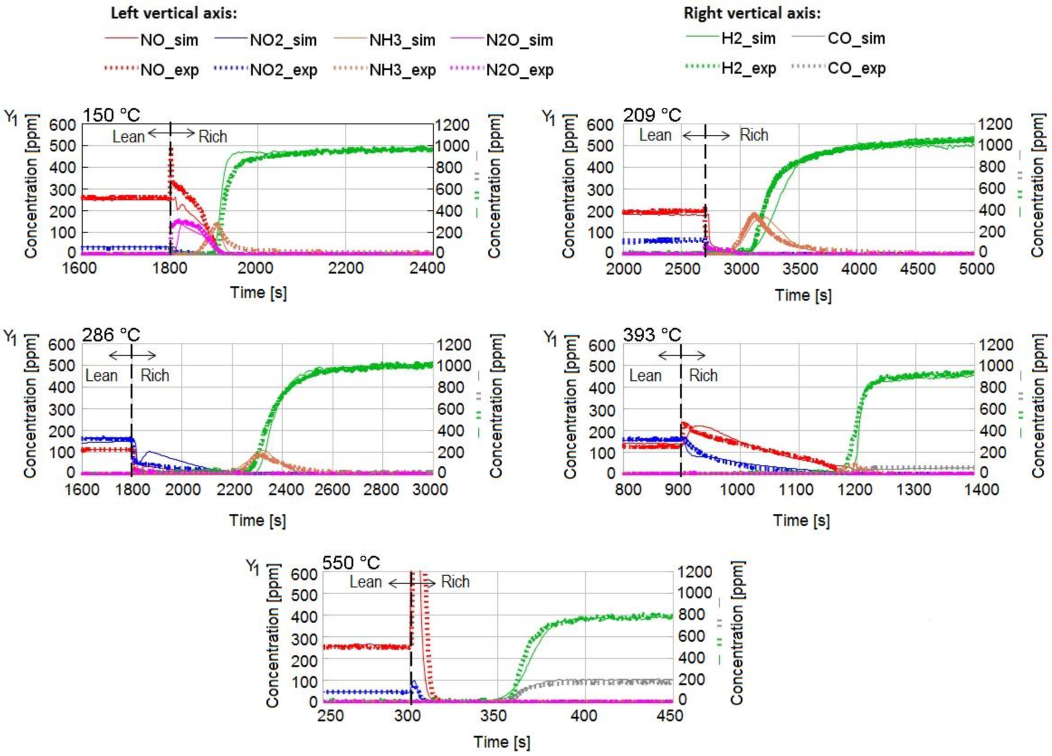

Figure 37. NO_x reduction calibrated simulation model in comparison with experimental data when H_2 is used as the reductant, CO and H_2 concentrations are referred to right axis and other species are referred to left axis; LNT case study #1

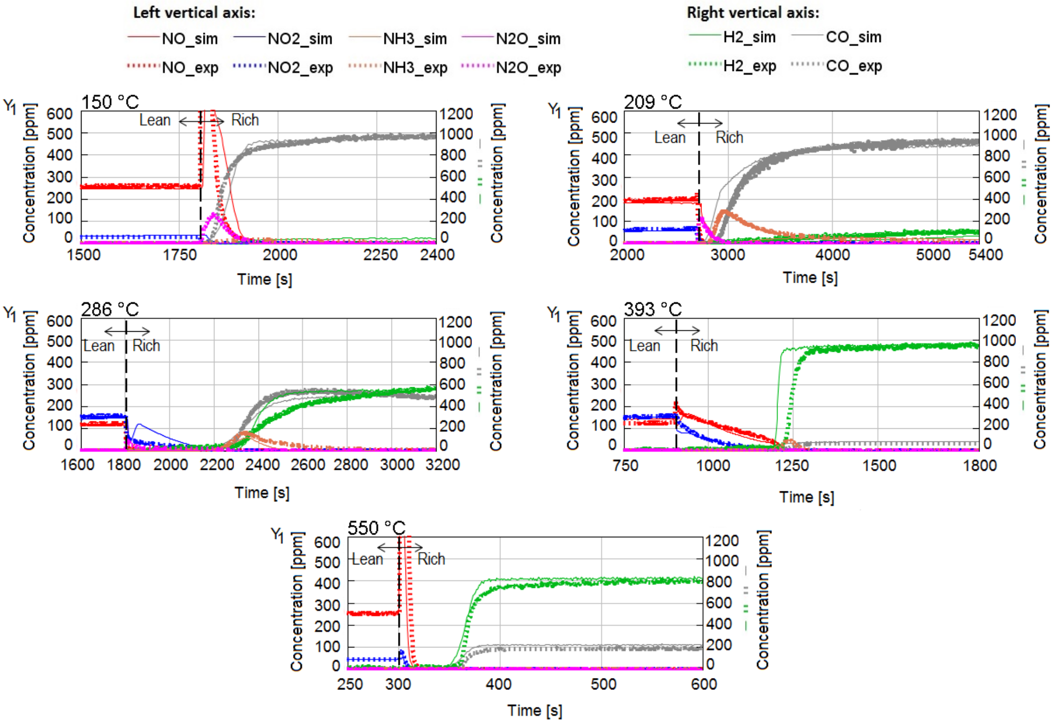

Figure 38. NO_x reduction calibrated simulation model in comparison with experimental data when CO is used as the reductant, CO and H_2 concentrations are referred to right axis and other species are referred to left axis; LNT case study #1

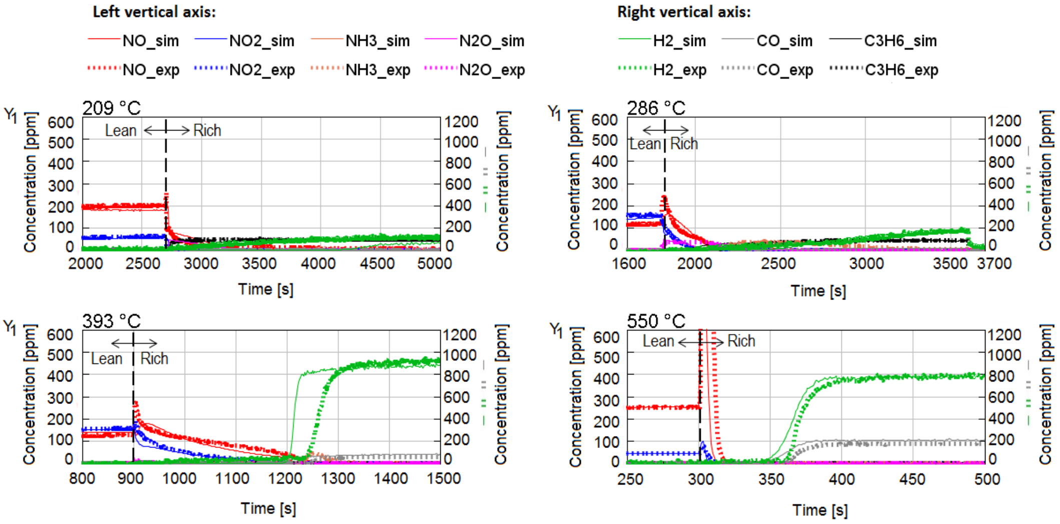

Figure 39. NO_x reduction calibrated simulation model in comparison with experimental data when C_3H_6 is used as the reductant, CO and H_2 concentrations are referred to right axis and other species are referred to left axis; LNT case study #1

NH_3 production is the highest at 209 °C both for CO and H_2 reductant experiments. Because H_2 is the main source of ammonia production, the highest NH_3 slip is observed when the primary reductant is H_2 [85,90]. Lindholm et al. [93]

evaluated the effect of H_2 concentration on ammonia production and observed that higher ammonia slip is detected when higher feed concentrations of hydrogen. In a similar study, Kočí et al. [74] concluded that the highest ammonia production is detected at around 200 °C, while at higher temperatures ammonia consumption reactions become faster.

Regarding nitrous oxides, it is observed that N_2O formation has highest selectivity at lower temperatures [93,94]. Lindholm et al. [93] observed that the amount of N_2O generated is more favored at lower temperatures. In a similar study by Kočí [75], it was concluded that maximum nitrous oxide yield occurs at temperatures below 300 °C. On the other hand, N_2O production is limited when C_3H_6 is used, which is consistent with the outcome of the work done by Abdulhamid et al. [85]. Moreover, generation of NH_3 and N_2O are predicted accurately with respect to experimental results, with NH_3 breakthrough occurring after N_2O disappears.

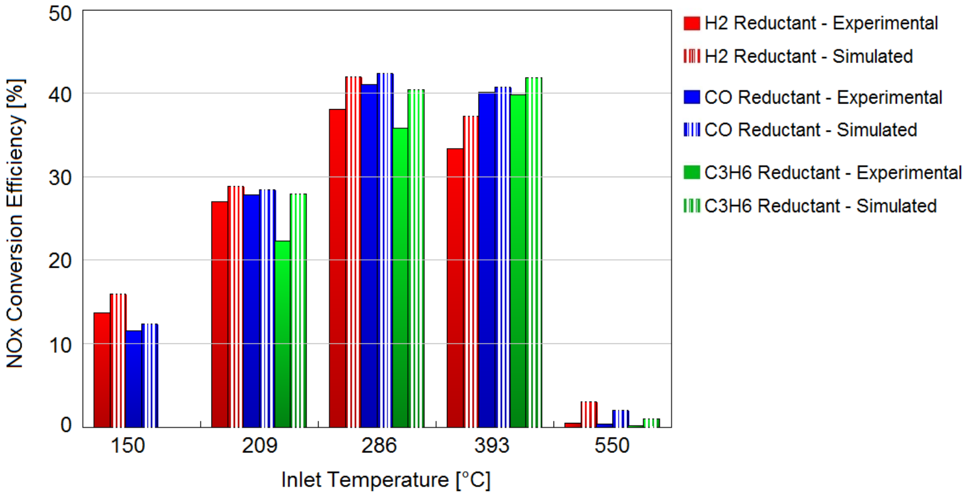

Figure 40. Integral NO_x conversion efficiency for different reductants H_2, CO and C_3H_6; LNT case study #1

3.3 Lean NO_x Trap – Case Study 2

In order to test the kinetic model robustness, the performance of another type of LNT catalyst was studied both experimentally and numerically. The analysis was performed with a core sample from an LNT monolith (cordierite, 400 cpsi) used for diesel passenger car applications.

3.3.1 Experimental Set-up

The lab scale samples were obtained from a full-scale monolith as it can be observed in Figure 41, such that the diameter of the sample does not exceed 18.5 mm. The experiments were performed on an oven aged core. It is worth noting that the catalyst technology in terms of PGM ratio and loading and component composition is different from the one of case study #1; however, due to confidentiality reasons more details are not reported.

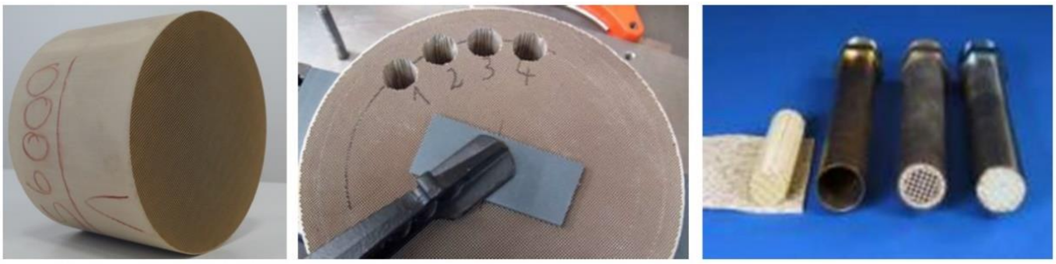

Figure 41. Extraction of LNT case study #2 lab scale samples from full scale monolith

The main characteristics of the sample are reported in Table 19.

Table 19. Main characteristics of the LNT under investigation in case study #2

Characteristic	**Unit**	**Value**
Substrate material	-	Cordierite
Cell density	cpsi	400
Wall thickness	mil, (mm)	4, (0.1016)
Dimensions (short radius x long radius x length)	mm	68.58 x 68.58 x 96.6
PGM loading	g/ft^3	120
PGM ratio (Pt:Pd:Rh)	-	103:12:5

The experimental activity was performed at ACA – Center for Automotive Catalytic Systems of the RWTH Aachen University through a laboratory gas bench, shown in Figure 42-a. The sample is put into an isothermal cylindrical reactor and the reactor core sample size should have a diameter around 18 mm and a length in the range of 50 to 180 mm. The gases were mixed from compressed gas cylinders using mass flow controllers. It is important to note that inlet concentrations were not measured during the tests; although, a by-pass flow at the beginning and at the end of each test is used to measure the composition of the inlet mixture. Therefore, in the simulations the nominal values reported in the test protocols are imposed.

As depicted in Figure 42-b, two thermocouples, 0.5 mm diameter each, are mounted in the gas flow upstream, TUS, and downstream, TDS, of the sample. Moreover, the temperatures at the sample central channel inlet, T1, middle (3 radial positions, T2, T4, T5), and outlet, T3, have also been measured.

Gas concentration measurements were performed with a multicomponent FTIR with 1 Hz sampling frequency. Moreover, lambda evaluation was performed via

Lambdasonde (UEGO) and calculation from feed gas. Since H_2 measurements were not available downstream of the catalyst, the predicted catalyst outlet H_2 concentration from simulation model could be validated only indirectly by checking the other species concentrations.

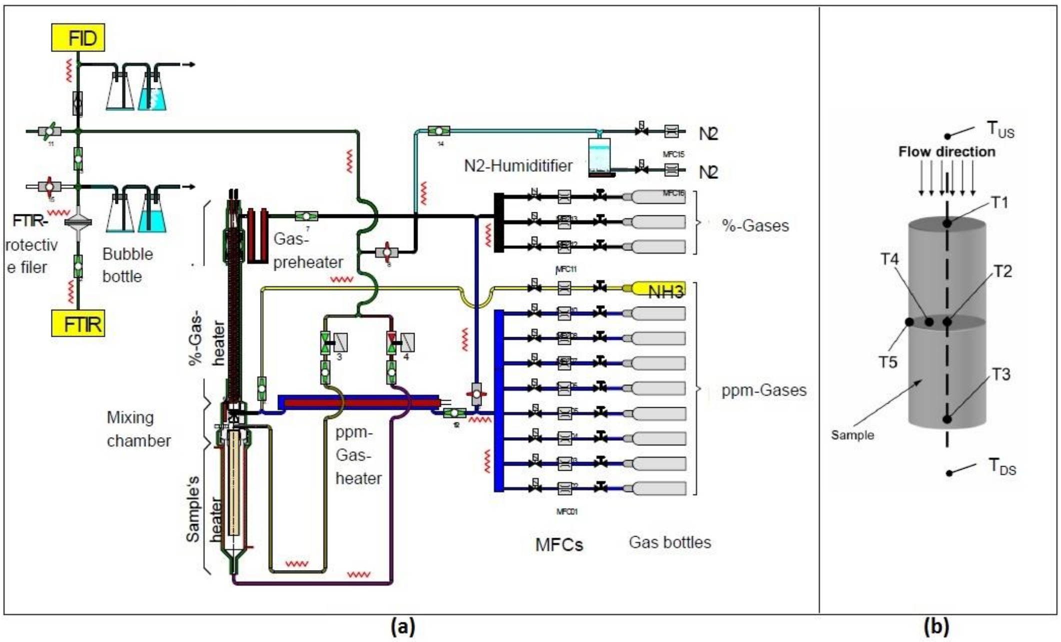

Figure 42. Experimental setup: schematic view of laboratory gas bench for case study #2 (a) and thermocouple locations on the lab scale sample (b)

3.3.2 Test Protocols

The SGB test protocols are similar to the ones defined for case study #1 with minor changes. The isothermal tests are performed at constant standard space velocity of 30,000 1/hr, measured at 273.15 K and 101325 Pa. The tests can be categorized in three main groups: light-off tests, OSC and NSR.

3.3.2.1 Oxygen Storage Capacity (OSC)

The OSC experiment is performed at a space velocity of 30,000 1/hr, measured at 273.15 K and 101325 Pa with a sufficient pre-reduction with H_2 prior to each test run, around 900 seconds. Five inlet temperatures, starting from 150 °C to 450 °C are tested.

Identical to case study #1, OSC consists of a lean phase and a short rich phase by introduction of CO as the reducing agent. In this case, overlap between feeding oxygen and CO simultaneously is avoided by waiting to feed CO until oxygen is completely shut-off. The inlet gas composition is presented in Table 20.

Table 20. Inlet gas composition for OSC experiments in LNT case study #2 (concentrations on volume basis)

Species	Lean phase (60 s)	Rich phase (30 s)
CO [ppm]	0	20000
O_2 [%]	0.5	0
CO_2 [%]	5	0
H_2O [%]	10	10
N_2	Balance	Balance

3.3.2.2 NO_x Storage and Reduction (NSR)

The NSR test is carried out at a space velocity of 30,000 1/hr, measured at 273.15 K and 101325 Pa with a sufficient pre-reduction with H_2 prior to each test run, around 900 seconds. Five inlet temperatures, starting from 150 °C to 400 °C, are tested which are equally spaced in 1/T, where T is in K. Similar to case study #1, the experiment is ideally repeated at each temperature using H_2, CO, and HC (represented by propylene, C_3H_6) as reductant for each step. The inlet gas composition for lean/rich cycle is reported in Table 21. NO_x is fed during the lean phase together with O_2 and after around 1000 seconds, NO_x and O_2 flows are shut-off and reductants in separate steps, H_2, CO and C_3H_6, are injected with the aim to clean-off the NO_x storage sites. Since engine-out NO_x emission mainly consists of NO, in the NSR test protocol inlet NO_x only includes NO, although NO_2 adsorption/desorption kinetics can be indirectly characterized due to production of NO_2 from oxidation of NO. An example of measured NO_x during NSR experiment in which H_2 is used as the primary reductant is presented in Figure 43.

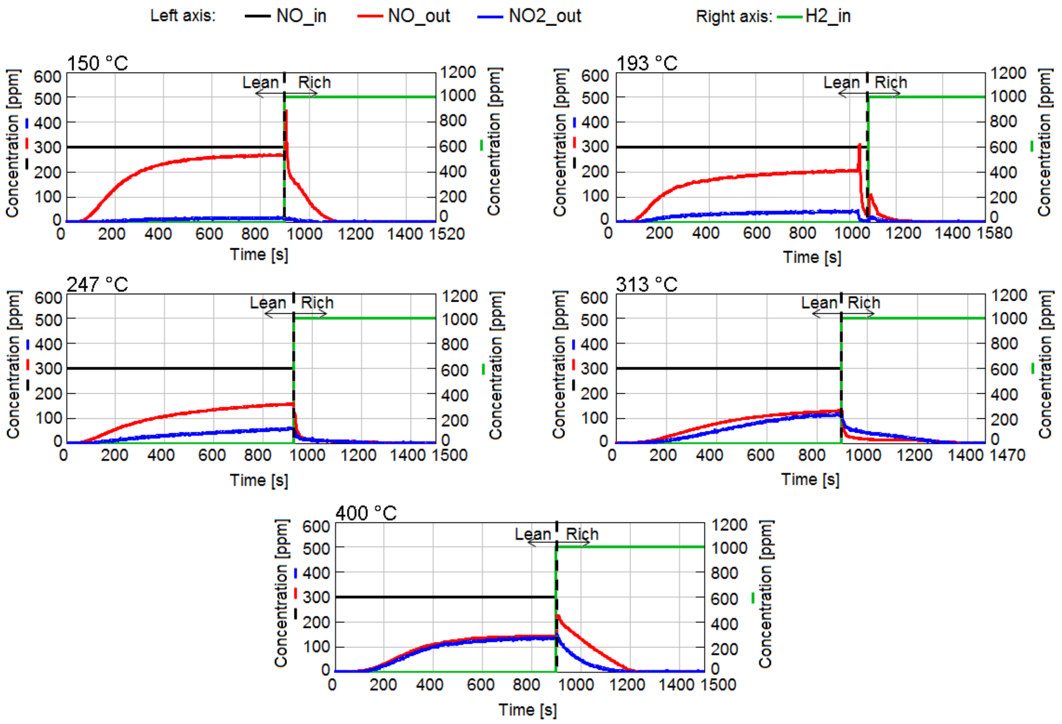

Figure 43. Measured NO and NO_2 profiles from NSR experiments with 300 ppm NO feed during lean phase and 1000 ppm H_2 during rich phase; LNT case study #2

The inlet gas feed composition is expressed in Table 21 in volume basis. Similar to case study #1, the reductant concentrations were selected such that the NO_x reduction potential constant is held constant, i.e. around 110 ppm of C_3H_6 can reduce the same quantity of NO_x as 1000 ppm H_2 based on reaction stoichiometry.

Table 21. Inlet gas composition for NSR experiments in LNT case study #2 (concentrations on volume basis)

Species	Lean	Rich, H_2	Rich, CO	Rich, HC
Reductant [ppm]	0	1000	1000	110
O_2 [%]	10	0	0	0
CO_2 [%]	5	0	0	0
H_2O [%]	5	5	5	5
NO [ppm]	300	0	0	0
N_2	Balance	Balance	Balance	Balance

3.3.2.2 Light-off

The light-off behavior of the catalyst during warm-up can be examined by means of light-off experiments through a temperature ramp cycle which gives the possibility to predict the CO and HC oxidation rates on the noble metal component as a function of the catalyst temperature [95]. The temperature ramp cycle starts from 125°C to 300°C at a rate of 3 K/min. The experiment is performed at a space velocity of 40,000 1/hr with the inlet feed composition shown in Table 22. HCs are specified on a C3 basis and consist of a 2:1 molar ratio of propane (C_3H_8), representative of slow oxidizing HC, to propylene (C_3H_6), representative of fast oxidizing HC.

Table 22. Inlet gas composition for light-off experiments in LNT case study #2 (concentrations on volume basis)

Species	Composition
HC [ppmC3]	400
CO [ppm]	300
H_2 [ppm]	60
O_2 [%]	10
CO_2 [%]	5
H_2O [%]	5
N_2	Balance

3.3.3 Kinetic model development and calibration guideline

The LNT model was built at first for the reactor scale sample, i.e. for a cylinder of 18 mm diameter and a length of 96.6 mm, corresponding to the full monolith length.

The reaction mechanism is a global-type surface reaction mechanism using turnover number reaction rate format, expressed in units of mol/mol-site/sec, where mol-site is the active site density participating in the reaction. The model incorporates the NO oxidation, NO_x adsorption/desorption on barium sites, oxygen storage on ceria and NO_x reduction reactions in addition to WGS and steam reforming reaction taking place over PGM. Similar to LNT case study #1, total of five sites participate in the reaction: ceria, three different barium sites, and Platinum Group Metals (PGM). The kinetic parameters including site densities, pre-exponent multipliers and activation energies, of Arrhenius term, were calibrated with the aim to match the simulation results with measurement data. Details about model set-up and assumptions can be found in Section 3.2.

In steps such as OSC and NSR, the calibration procedure is identical to the one in the LNT case study #1, which is described in Section 3.2, while more details will be provided regarding light-off tests calibration, which was not included in the test protocols listed for the LNT case study #1.

3.3.3.1 Oxygen Storage and Reduction

The reaction model of the OSC test includes Water Gas Shift (WGS) reaction on the precious metal, storage of oxygen and its reduction via CO, H_2 and C_3H_6 on ceria sites, as reported in Table 11. As far as ceria site cleaning with H_2 and HC, Reaction #4 and Reaction #5, is considered, the rate constants are later tuned to to accommodate the NO_x reduction model development; since the OSC test protocol did not include tests with H_2 and C_3H_6 used as the reductant. The optimized pre-exponent multipliers and activation energies for OSC reaction model are expressed in Table 23 and Table 24.

Table 23. WGS and oxygen storage and reduction reactions for LNT case study #2

#	Reaction	Rate Expression
1	$H_2O + CO \xleftrightarrow{K_{eq,WGS}} CO_2 + H_2$	$r_1 = \frac{k_1 C_{CO} C_{H_2O} - \frac{C_{CO_2} C_{H_2}}{K_{eq,WGS}}}{G_1}$
2	$Ce_2O_3 + 0.5O_2 \rightarrow 2CeO_2$	$r_2 = k_2 C_{O_2} (\theta_{Ce_2O_3}^{eq} - \theta_{Ce_2O_3})$
3	$2CeO_2 + CO \rightarrow Ce_2O_3 + CO_2$	$r_3 = k_3 C_{CO} \theta_{CeO_2}$
4	$2CeO_2 + H_2 \rightarrow Ce_2O_3 + H_2O$	$r_4 = k_4 C_{H_2} \theta_{CeO_2}$
5	$2CeO_2 + \frac{1}{9} C_3H_6 \rightarrow Ce_2O_3 + \frac{1}{3} H_2O + \frac{1}{3} CO_2$	$r_5 = k_5 C_{C_3H_6} \theta_{CeO_2}$

$$G_1 = \left(1 + 9.467 \exp\left(\frac{63.451}{T}\right) C_{CO} + 274.82 \exp\left(\frac{-215.34}{T}\right) C_{C_3H_6}\right)^2 \left(1 + 0.00061 \exp\left(\frac{9715.6}{T}\right) C_{CO}^2 C_{C_3H_6}^2\right) \left(1 + 5.554E6 \exp\left(\frac{-6206.9}{T}\right) C_{NO}\right)$$

Table 24. Kinetic parameters for WGS and oxygen storage and reduction reactions of LNT case study #2 and comparison with LNT case study #1

#	Pre-Exponent Multiplier		Activation Energy (J/mol)	
	Case study #2	**Case study #1**	**Case study #2**	**Case study #1**
1	8.12E8	$3.24E6$	73430	61000
2	1.8	0.1	0	0
3	3.2	3.2	$1800(1-0.9\theta_{CeO_2})$	$1800(1-0.9\theta_{CeO_2})$
4	12.6	12.6	$2900(1-0.7\theta_{CeO_2})$	$2900(1-0.7\theta_{CeO_2})$
5	15	0.06	$1800(1-0.9\theta_{CeO_2})$	$1800(1-0.9\theta_{CeO_2})$

Similar to case study #1, the calibration is started from WGS reaction. In this case, due to the fact that H_2 measurement was not available, the amount of produced H_2 was estimated from CO_2 production during rich pulse; considering that each produced mole of CO_2 is equivalent to one mole of H_2 according to stoichiometry of water gas shift reaction. The results of OSC calibration model for each inlet temperature are shown in Figure 44, considering that the start of the rich phase is characterized by the injection of CO as the reductant.

The production of CO_2 as a result of water gas shift reaction is predicted with good accuracy, which increases by increasing temperature, such that at higher temperatures all CO is converted to H_2 and CO_2 and at the highest temperature level, the water gas shift reaction is controlled by equilibrium. Moreover, CO breakthrough which takes into account the stored O_2 clean-off from ceria sites matches the experimental data with satisfactory accuracy. More details about model assumptions and calibration guideline can be found in Section 3.2.

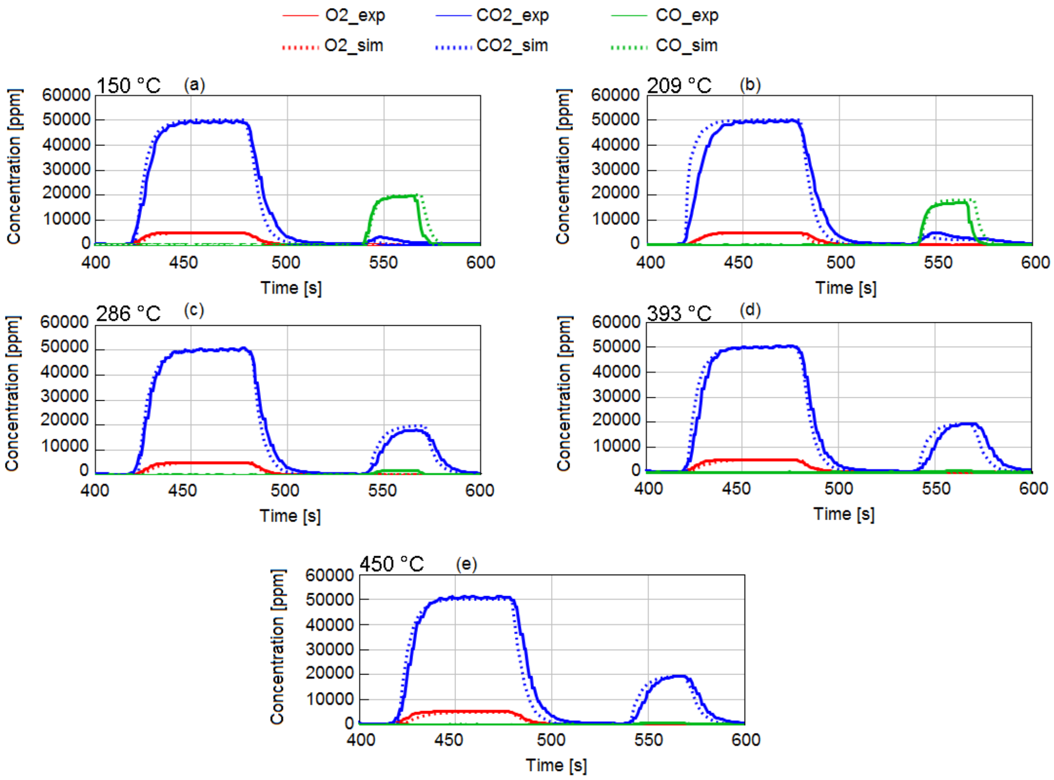

Figure 44. Measured outlet concentration for one cycle of the oxygen storage and reduction experiments at (a) 150°C, (b) 209°C, (c) 286°C, (d) 393°C, (e) 550°C for LNT case study #2

3.3.3.2 NO_x Storage and Reduction

Despite availability of experimental data for LNT case study #1 for pure NO_x adsorption/desorption decoupled with reduction, in this case NO_x storage and reduction tests are performed in a single test; therefore, during the lean phase (NO_x feeding) NO_x storage reactions can be calibrated and afterwards, when NO_x feeding is stopped and reductants are inject, by focusing on rich phase, NO_x reduction reactions

NO_x storage capacity has been calculated using the data presented in Figure 43 and according to Equation 29 in which $t_{NO_{x,stop}}$ represents the time at which NO_x feeding is stopped, lean duration. NO_x storage capacity is depicted in Figure 45 which shows a bell shape behavior [70,74] with maximum storage occurring at medium temperatures, which is consistent with the results obtained for LNT case study #1, Section 3.2. It is worth mentioning that in this case the lean duration is fixed and equal for all temperature steps, which is in contrast to LNT case study #1, in which lean duration was altered at different temperatures such that saturation was reached.

$$n_{NO_x,stored} = \int_0^{t_{NO_x,stop}} \left(\dot{n}_{NO_x,in} - \dot{n}_{NO_x,out}\right) dt \tag{29}$$

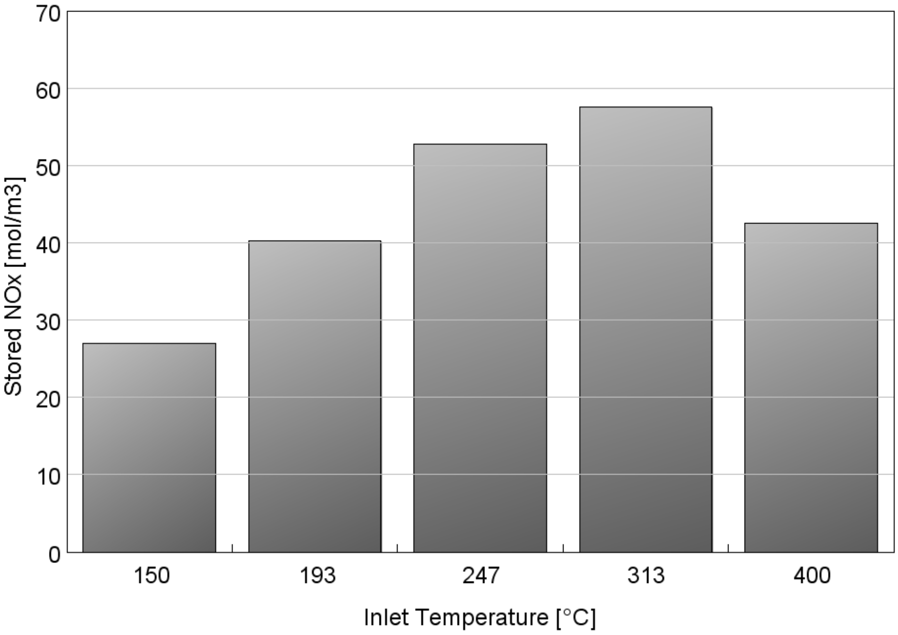

Figure 45. NO_x stored per unit reactor volume for LNT case study #2

Similar to the model represented for NO_x storage in Section 3.2 for the LNT case study #1, a three-site model, differentiated by Ba^I, Ba^{II} and Ba^{III} and site densities expressed in Table 25, is developed with the reactions and kinetic parameters reported in Table 26 and Table 27. The calibration procedure is identical to the one presented in Section 3.2 for the LNT case study #1. More details about calibration procedure, the rationality of selection of proposed reaction pathways and different sites can be found in Section 3.2.

Table 25. Site densities in the turnover number based reaction model; LNT case study #2

Site	**Site Density [mol/m^3]**	
	Case study #1	**Case study #2**
PGM	2.2	2.0
Ce	80	109
Ba^I	35	60
Ba^{II}	10	14
Ba^{III}	9	16

Comparing the site densities calculated for the LNT case study #2, Table 25, with the ones obtained for the LNT case study #1, it can be appreciated that the storage capacity is expected to be lower for the LNT case study #2 which can also be confirmed comparing the storage curves and Figure 31 and Figure 45, with maximum values of 120 (#1) and 60 (#2) mol/m^3, respectively.

Table 26. NO oxidation and NO$_x$ storage reactions for LNT case study #2

#	**Reaction**	**Rate Expression**
6	$NO + 0.5O_2 \rightarrow NO_2$	$r_6 = k_6 \dfrac{C_{NO}C_{O_2}^{0.5} - \dfrac{C_{NO_2}}{K_{eq,NO}}}{G_1}$
7	$Ba^{I}O + 3NO_2 \rightarrow Ba^{I}(NO_3)_2 + NO$	$r_7 = k_7 C_{NO_2}\theta_{Ba^{I}O}$
8	$Ba^{I}O + 2NO + 1.5O_2 \rightarrow Ba^{I}(NO_3)_2$	$r_8 = k_8 C_{NO}C_{O_2}^{0.1}\theta_{Ba^{I}O}$
9	$Ba^{I}(NO_3)_2 \rightarrow Ba^{I}O + 2NO + 1.5O_2$	$r_9 = k_9\theta_{Ba^{I}(NO_3)_2}$
10	$Ba^{II}O + 3NO_2 \rightarrow Ba^{II}(NO_3)_2 + NO$	$r_{10} = k_{10}C_{NO_2}\theta_{Ba^{II}O}$
11	$Ba^{II}O + 2NO + 0.5O_2 \rightarrow Ba^{II}(NO_2)_2$	$r_{11} = k_{11}C_{NO}C_{O_2}^{0.1}\theta_{Ba^{II}O}$
12	$Ba^{II}(NO_2)_2 \rightarrow Ba^{II}O + 2NO + 0.5O_2$	$r_{12} = k_{12}\theta_{Ba^{II}(NO_2)_2}$
13	$Ba^{II}(NO_2)_2 + O_2 \rightarrow Ba^{II}(NO_3)_2$	$r_{13} = k_{13}C_{O_2}^{0.1}\theta_{Ba^{II}(NO_2)_2}$
14	$Ba^{II}(NO_3)_2 \rightarrow Ba^{II}O + 2NO_2 + 0.5O_2$	$r_{14} = k_{14}\theta_{Ba^{II}(NO_3)_2}$
15	$Ba^{III}O + 2NO + 1.5O_2 \rightarrow Ba^{III}(NO_3)_2$	$r_{15} = \dfrac{k_{15}C_{NO}C_{O_2}^{0.1}\theta_{Ba^{III}O}}{G_2}$
16	$Ba^{III}(NO_3)_2 \rightarrow Ba^{III}O + 2NO + 1.5O_2$	$r_{16} = k_{16}\theta_{Ba^{III}(NO_3)_2}$

$$G_2 = 1 + 0.0001675213\,\exp(8952.6/T)\,C_{NO}$$

Table 27. Kinetic parameters for NO oxidation and NO_x storage; LNT case study #2 compared with identical reactions present in kinetic scheme of LNT case study #1

#	**Pre-exponent Multiplier**		**Activation Energy [J/mol]**	
	Case study #2	**Case study #1**	**Case study #2**	**Case study #1**
6	3.4E4	5.25E4	39400	39400
7	0.8	0.2	0	0
8	0.21	-	0	-0
9	128	-	60690	-
10	3.1	3.1	0	0
11	2.1	1.2	0	0
12	0.032	0.032	$21400\ (1-0.7\theta_{Ba^{II}(NO_2)_2})$	$21400\ (1-0.7\theta_{Ba^{II}(NO_2)_2})$
13	4660	1480	66200	66200
14	7.94E6	2E12	109560	185000
15	12.6	12	0	0
16	2.24E15	1.12E16	257000	257000

Preliminary analysis on the measured data, suggests a reaction model similar to the one proposed for case study #1, Section 3.2. As it can be appreciated from Figure 46, the delayed ammonia slip with respect to other species suggests a pathway through which ammonia is generated from reaction of primary reductant with stored NO_x which is further consumed as a secondary reductant to reduce remaining stored NO_x to N_2, NO_x or N_2O as by-product; this assumption is coherent with the model proposed by Kočí et al. [70,74], Shwan et al. [76] and Lindholm et al. [89] and the one used in Section 3.2 for LNT case study #1.

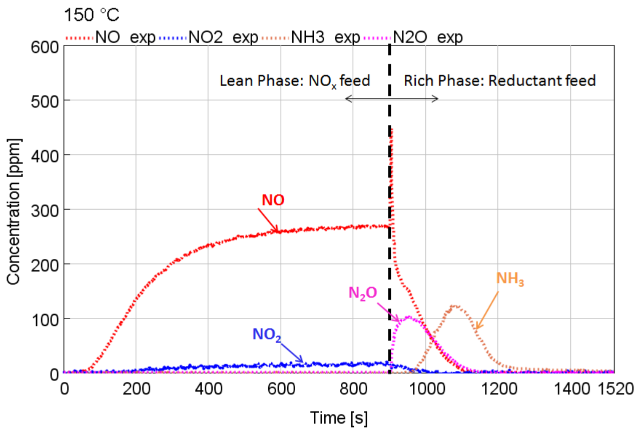

Figure 46. Experimental outlet concentration of NO_x, NH_3 and N_2O during LNT regeneration by H_2 at 150 °C for LNT case study #2

Considering the abovementioned observations, a NO_x reduction model is reported in Table 28 and Table 29 through which NO_x stored in the form of nitrates and nitrites will be converted to gaseous NO_x, N_2 or NH_3 and N_2O as by-products and therefore the storage sites would be cleaned-off. The calibration is performed with the aim to minimize the difference between predicted and measured outlet concentrations of different species with the procedure explained in Section 3.2. The optimized kinetic parameters are reported in Table 30.

Table 28. NO_x Reduction reaction on barium sites for LNT case study #2

#	Reaction	Rate Expression
17	$Ba^{II}(NO_2)_2 + 6H_2 \rightarrow Ba^{II}O + 2NH_3 + 3H_2O$	$r_{17} = k_{17}C_{H_2}\theta_{Ba^{II}(NO_2)_2}$
18	$Ba^{II}(NO_2)_2 + 2NH_3 \rightarrow Ba^{II}O + 2N_2 + 3H_2O$	$r_{18} = k_{18}C_{NH_3}\theta_{Ba^{II}(NO_2)_2}$
19	$Ba^{II}(NO_2)_2 + 0.4NH_3 \rightarrow Ba^{II}O + 2.4NO + 0.6H_2O$	$r_{19} = k_{19}C_{NH_3}\theta_{Ba^{II}(NO_2)_2}$
20	$Ba^{II}(NO_3)_2 + \frac{10}{3}NH_3 \rightarrow Ba^{II}O + \frac{8}{3}N_2 + 5H_2O$	$r_{20} = k_{20}C_{NH_3}\theta_{Ba^{II}(NO_3)_2}$
21	$Ba^{II}(NO_3)_2 + 2NH_3 \rightarrow Ba^{II}O + 2N_2O + 3H_2O$	$r_{21} = k_{21}C_{NH_3}\theta_{Ba^{II}(NO_3)_2}$
22	$Ba^{I}(NO_3)_2 + 8H_2 \rightarrow Ba^{I}O + 2NH_3 + 5H_2O$	$r_{22} = k_{22}C_{H_2}\theta_{Ba^{I}(NO_3)_2}$
23	$Ba^{I}(NO_3)_2 + \frac{10}{3}NH_3 \rightarrow Ba^{I}O + \frac{8}{3}N_2 + 5H_2O$	$r_{23} = k_{23}C_{NH_3}\theta_{Ba^{I}(NO_3)_2}$
24	$Ba^{III}(NO_3)_2 + 3H_2 \rightarrow Ba^{III}O + 2NO + 3H_2O$	$r_{24} = k_{24}C_{H_2}\theta_{Ba^{III}(NO_3)_2}$
25	$Ba^{III}(NO_3)_2 + 8H_2 \rightarrow Ba^{III}O + 2NH_3 + 5H_2O$	$r_{25} = k_{25}C_{H_2}\theta_{Ba^{III}(NO_3)_2}$
26	$Ba^{III}(NO_3)_2 + \frac{10}{3}NH_3 \rightarrow Ba^{III}O + \frac{8}{3}N_2 + 5H_2O$	$r_{26} = k_{26}C_{NH_3}\theta_{Ba^{III}(NO_3)_2}$
27	$Ba^{I}(NO_3)_2 + 5CO \rightarrow Ba^{I}O + 5CO_2 + N_2$	$r_{27} = k_{27}C_{CO}\theta_{Ba^{I}(NO_3)_2}$
28	$Ba^{II}(NO_3)_2 + 4CO \rightarrow Ba^{II}O + 4CO_2 + N_2O$	$r_{28} = k_{28}C_{CO}\theta_{Ba^{II}(NO_3)_2}$

29	$Ba^{II}(NO_3)_2 + 3CO \rightarrow Ba^{II}O + 3CO_2 + 2NO$	$r_{29} = k_{29}C_{CO}\theta_{Ba^{II}(NO_3)_2}$
30	$Ba^{III}(NO_3)_2 + 5CO \rightarrow Ba^{III}O + 5CO_2 + N_2$	$r_{30} = k_{30}C_{CO}\theta_{Ba^{III}(NO_3)_2}$
31	$Ba^{II}(NO_2)_2 + CO \rightarrow Ba^{II}O + CO_2 + 2NO$	$r_{31} = k_{31}C_{CO}\theta_{Ba^{II}(NO_2)_2}$
32	$Ba^{I}(NO_3)_2 + \frac{5}{9}C_3H_6 \rightarrow Ba^{I}O + \frac{5}{3}CO_2 + \frac{5}{3}H_2O + N_2$	$r_{32} = k_{32}C_{C_3H_6}\theta_{Ba^{I}(NO_3)_2}$
33	$Ba^{I}(NO_3)_2 + \frac{1}{3}C_3H_6 \rightarrow Ba^{I}O + CO_2 + H_2O + 2NO$	$r_{33} = k_{33}C_{C_3H_6}\theta_{Ba^{I}(NO_3)_2}$
34	$Ba^{II}(NO_3)_2 + \frac{5}{9}C_3H_6 \rightarrow Ba^{I}O + \frac{5}{3}CO_2 + \frac{5}{3}H_2O + N_2$	$r_{34} = k_{34}C_{C_3H_6}\theta_{Ba^{II}(NO_3)_2}$
35	$Ba^{II}(NO_2)_2 + \frac{1}{9}C_3H_6 \rightarrow Ba^{I}O + \frac{1}{3}CO_2 + \frac{1}{3}H_2O + 2NO$	$r_{35} = k_{35}C_{C_3H_6}\theta_{Ba^{II}(NO_3)_2}$
36	$Ba^{III}(NO_3)_2 + \frac{5}{9}C_3H_6 \rightarrow Ba^{III}O + \frac{5}{3}CO_2 + \frac{5}{3}H_2O + N_2$	$r_{36} = k_{36}C_{C_3H_6}\theta_{Ba^{III}(NO_3)_2}$
37	$Ba^{III}(NO_3)_2 + \frac{1}{3}C_3H_6 \rightarrow Ba^{III}O + CO_2 + H_2O + 2NO$	$r_{37} = k_{37}C_{C_3H_6}\theta_{Ba^{III}(NO_3)_2}$

Table 29. PGM reactions participating in NO$_x$ reduction for LNT case study #2

#	**Reaction**	**Rate Expression**
38	$NO + 2.5H_2 \rightarrow NH_3 + H_2O$	$r_{38} = \frac{k_{38}C_{NO}C_{H_2}}{G_1}$
39	$C_3H_6 + 3H_2O \rightarrow 3CO + 6H_2$	$r_{39} = \frac{k_{39}C_{C_3H_6}C_{H_2O}}{G_1}$
40	$C_3H_6 + 9NO \rightarrow 3CO_2 + 3H_2O + 4.5N_2$	$r_{40} = \frac{k_{40}C_{C_3H_6}C_{NO}}{G_1}$

Table 30. Kinetic parameters for NO_x reduction reactions of LNT case study #2 compared with identical reactions present in kinetic scheme of LNT case study #1

#	Pre-exponent Multiplier		Activation Energy [J/mole]	
	Case study #2	**Case study #1**	**Case study #2**	**Case study #1**
17	25.26	14	12150	2750
18	2.49E7	2.4E6	55510	59800
19	5.23	7.95	940	3300
20	2.71E14	8	122770	3300
21	9.93	-	390	-
22	0.61	8.6E8	2460	85590
23	0.21	-	1250	-
24	4.12E15	-	177250	-
25	917	1.2E8	26440	85590
26	6.93E9	-	87830	-
27	1.36E8	1.4	68340	19900
28	5.99	-	1600	-
29	8243	-	32040	-
30	27.14	3896	10970	39700
31	2.42	7.3	3480	2580
32	8.8	3.6	7650	2780
33	6.81E11	2.7E7	111840	67000
34	20.57	-	13080	-
35	8.8	-	7650	-
36	42.2	1.8	13190	2780
37	6.78E31	-	357200	-
38	1.2E10	-	61600	-

39	4.5E15	6E8	94130	89200
40	2.37E23	3E10	212070	16200

The simulation results for NO, NO_2, CO, C_3H_6 and by-products NH_3 and N_2O for different reductants H_2, CO and C_3H_6 are shown in Figure 47, Figure 48 and Figure 49, respectively. It is shown that the NO and NO_2 traces during storage and regeneration phase are within acceptable accuracy compared to measured data for all the three reductants injected during rich pulse. It can be seen that even when CO and C_3H_6 are used as the primary reductants, the main share of regeneration is carried out by H_2 as a result of WGS and steam reforming reactions, specifically at higher temperatures where H_2 production is favored. Moreover, it was found out that C_3H_6 is less efficient in terms of NO_x slip abatement during reduction phase [96], specifically at low temperatures, as it can be observed in Figure 49.

NH_3 slip is found to be maximum at 193 °C, identical to the results obtained for the LNT case study #1 around 209 °C, both for CO and H_2 reductant experiments; which is also consistent to the trend of ammonia slip Kočí et al. [74] reported, maximum around 200 °C. At this temperature; from one side, sufficient H_2 is available as the main source of ammonia production [93] and from the other side, the rate of ammonia consumption reactions are not still so high compared with other reactions. Moreover, ammonia slip is limited when C_3H_6 is injected as the primary reductant, Figure 49. It is also important to note that the delayed concentration of outlet NH_3 with respect to N_2O is well-captured by the model due to consumption of a portion of ammonia for reducing barium nitrates and nitrites.

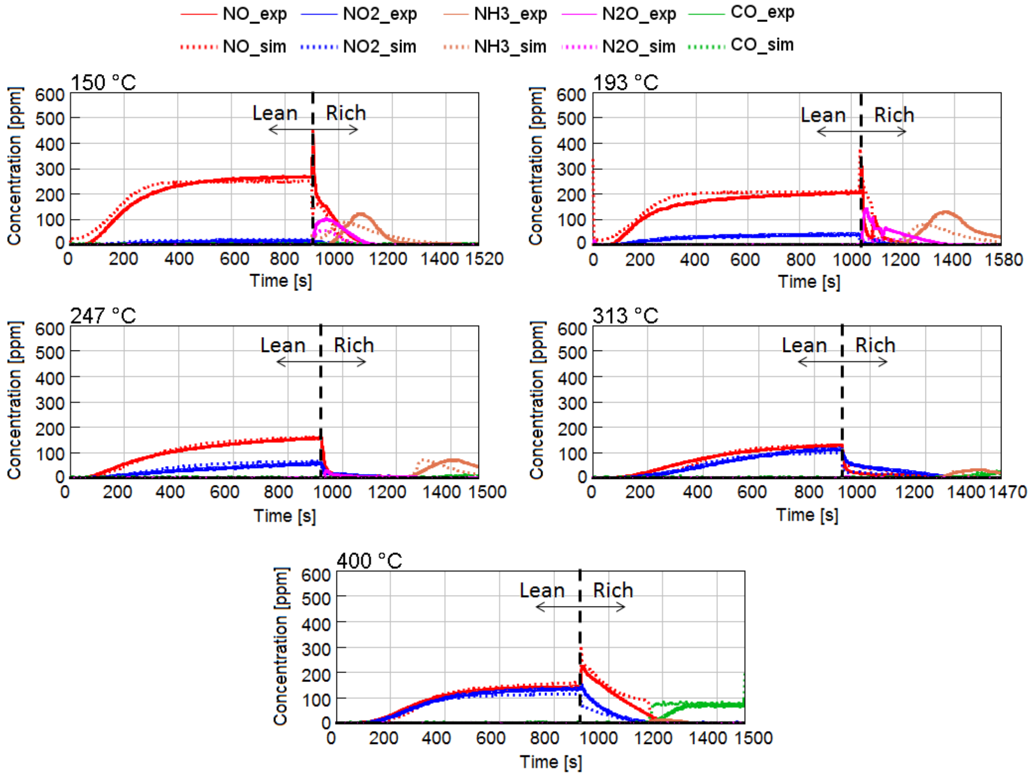

Figure 47. NO_x reduction calibrated simulation model in comparison with experimental data when H_2 is used as the reductant for the LNT case study #2

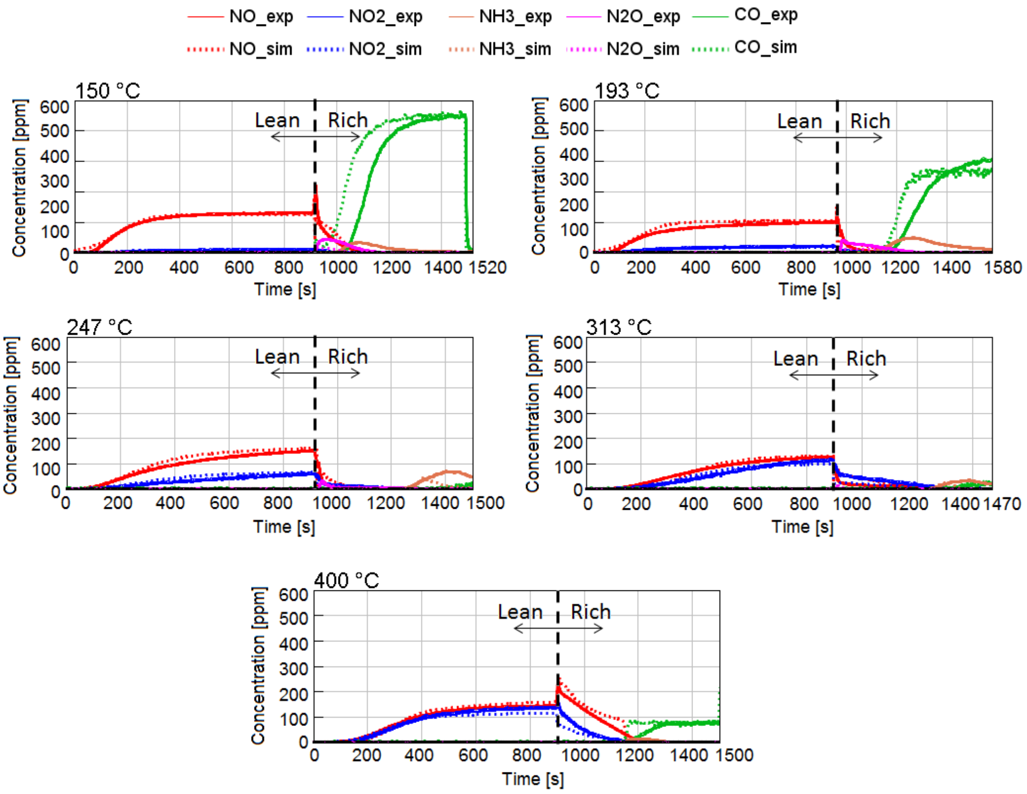

Figure 48. NO$_x$ reduction calibrated simulation model in comparison with experimental data when CO is used as the reductant for the LNT case study #2

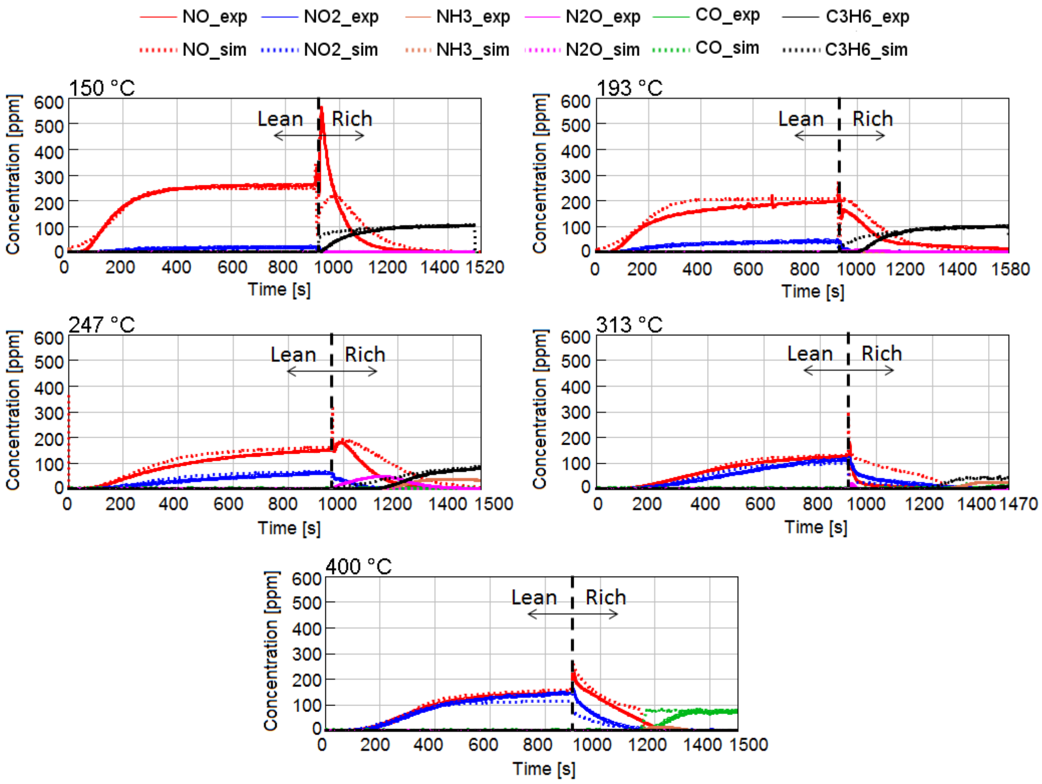

Figure 49. NO_x reduction calibrated simulation model in comparison with experimental data when C_3H_6 is used as the reductant for the LNT case study #2

The comparison between experimental and predicted NO_x conversion efficiency is depicted in Figure 50, which is calculated based on Equation 28. The simulation results show acceptable matching with experimental data with maximum difference not exceeding 8%. It can be observed that at low temperatures H_2 is the most effective reductant, reaching 23% and 22% of conversion efficiency from measured data and simulation model, respectively, exhibiting higher NO_x conversion with respect to CO and propylene. Moreover, the bell-shape NO_x conversion as a function of inlet temperature can be detected reaching around 50% at 247 °C, [75,97]. Besides, NO_x formation is higher when C_3H_6 is used as the primary reductant with respect to the H_2 and CO cases [91,92].

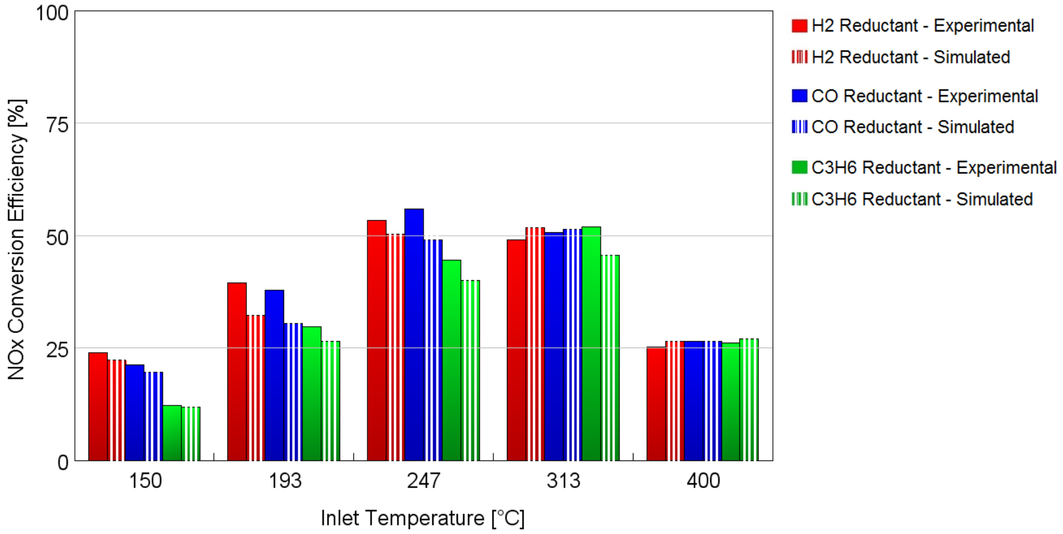

Figure 50. Integral NO_x conversion efficiency for different reductants H_2, CO and C_3H_6 for the LNT case study #2

3.3.3.3 Light-off

As far as light-off test modelling is considered, the reaction model includes the previously calibrated reactions in OSC tests, Table 23 , in addition to oxidation of CO, HC and H_2 and steam reforming [98], presented in Table 31. The pre-exponent multiplier and activation energy obtained for each reaction is reported in Table 32.

Table 31. Kinetic model for light-off experiment for LNT case study #2 on PGM

#	Reaction	Rate Expression
41	$CO + 0.5\,O_2 \rightarrow CO_2$	$r_{41} = \frac{k_{41} C_{CO} C_{O_2}}{G_1}$
42	$H_2 + 0.5\,O_2 \rightarrow H_2O$	$r_{42} = \frac{k_{42} C_{H_2} C_{O_2}}{G_1}$
43	$C_3H_8 + 5\,O_2 \rightarrow 3CO_2 + 4H_2O$	$r_{43} = \frac{k_{43} C_{C_3H_8} C_{O_2}}{G_1}$
44	$C_3H_6 + 4.5\,O_2 \rightarrow 3CO_2 + 3H_2O$	$r_{44} = \frac{k_{44} C_{C_3H_6} C_{O_2}}{G_1}$
45	$C_3H_8 + 3H_2O \rightarrow 3CO + 7H_2$	$r_{45} = \frac{k_{45} C_{C_3H_8} C_{H_2O}}{G_1}$

Table 32. Kinetic parameters for light-off experiment for LNT case study #2 on PGM

#	Pre-Exponent Multiplier	Activation Energy (J/mol)
41	8500	28035
42	9.43E14	111450
43	7.2E5	71060
44	4.49E12	11320
45	1.2E13	174250

Since the inlet temperature is not constant, Arrhenius approach proposed in Section 3.2.3.1 for finding the pre-exponent multipliers and activation energies is not applicable; hence, an automatic optimizer built in GT-SUITE can be used with the aim of minimizing the error between simulated and experimental concentrations of CO, C_3H_6 and C_3H_8. The optimization method selected in this case is the Brent method which is based on the root-finding that combines the bisection method, secant method, and inverse quadratic interpolation. It is gradient-free and is faster to converge compared with the discrete-grid method.

The history of concentrations at the outlet of the component and the conversion efficiencies as a function of inlet temperature are shown in Figure 51. It can be observed that both the concentrations and the conversion efficiencies are in good agreement with experimental data. As expected, the slow oxidizing HC, in this case propane, does not reach light-off until 370 °C. Furthermore, it can be appreciated from total HC conversion efficiency curve in Figure 51 at lower temperatures the slope is steeper due to oxidation of C_3H_6, while after full conversion of C_3H_6 (around 150 °C) conversion efficiency will increase with a more gradual slope due to oxidation of C_3H_8. In more detail, light-off temperatures based on 50% conversion efficiency are reported in Figure 52. The error between simulated and experimental light-off temperatures does not exceed 1.4 °C.

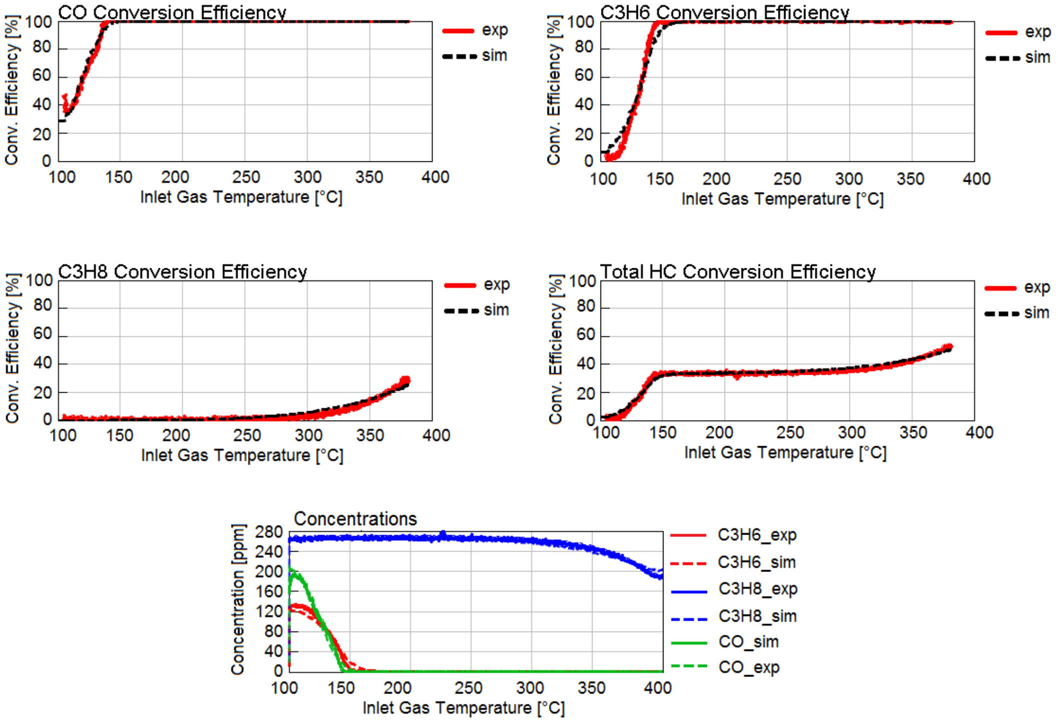

Figure 51. Light-off calibrated simulation model results in comparison with experimental data for the LNT case study #2

It is noteworthy that low CO light-off temperature can, at least in part, be attributed to the fact that the light-off inlet batch does not include NO, which typically shows a significant inhibition effect over the PGM: hence with the presence of NO, all light-off temperatures would be shifted to higher values. Moreover, the presence of considerable amount of H_2 in the inlet batch of light-off ($CO/H_2 = 300/60 = 5$), Table 22, affects strongly CO and HC oxidation and thus their light-off temperature [99]. This effect can be furtherly investigated by performing SGB tests with different H_2 concentrations.

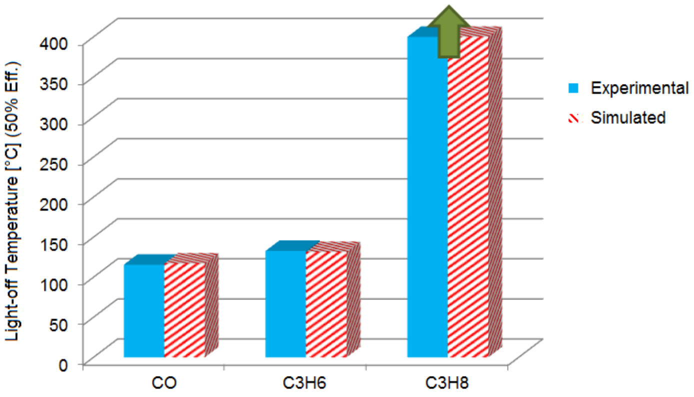

Figure 52. Comparison of simulation and experimental light-off temperature based on 50% efficiency for the LNT case study #2

In conclusion, by comparing the kinetic scheme and parameters defied for the two LNT studies with different washcoat compositions and PGM loadings and the similarities between the two cases, it can be observed that the methodology presented in this chapter can be used as a reference for development and calibration of an LNT model. Therefore, depending on the technology and by tuning some parameters, such as site densities, acceptable estimation of the behavior of the component regarding oxygen storage ad reduction, NO_x storage and reduction and light-off characteristics of the system can be achieved.

Chapter 4

Validation of reactor-scale LNT model on full-size components

4.1 Introduction and limitations

Building and calibration of an aftertreatment model based on experimental data for a full-size component using engine-out emissions is challenging due to transient conditions and complex gas mixture.For an LNT technology, the case is even more demanding due to the complex kinetic scheme as previously described in Chapter 3. Therefore, after calibration of a reactor-size model based on SGB tests, the model can be up-scaled and used for a full-size component, as shown in Figure 53.

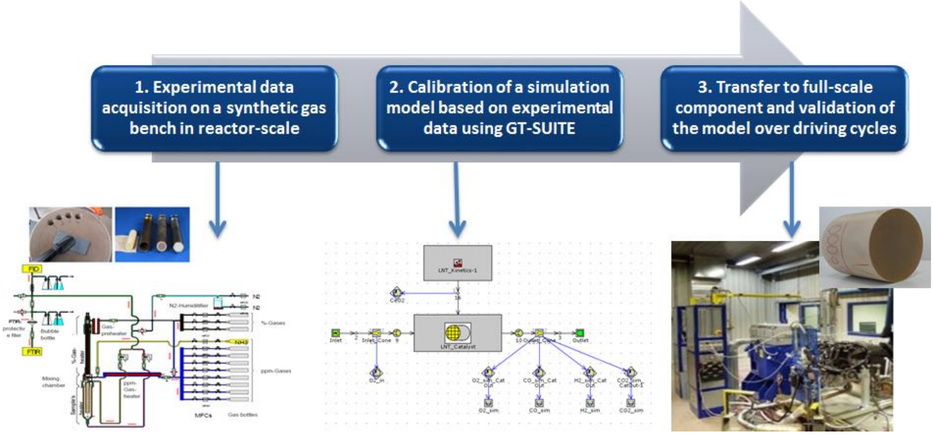

Figure 53. Transferring the calibrated reactor-scale model to full-scale component

Several studies have been focused on transformations of a calibrated reactor-size model to full-size component. As an example, Millet et al. [100] calibrated a global kinetic model for a Three Way Catalyst (TWC) using SGB data and applied the model to engine test bench experiments and indicated that some of the kinetic constants require modifications in order to consider the effect of geometry and washcoat formulation. Lafossas et al. [101] developed a global kinetic mechanism for a DOC component using SGB data; however, in order to reduce the gap between reactor-scale and full-scale model, after preliminary calibration based on SGB measurements, engine-out exhaust gas was fed to the reactor to capture the effect of HC speciation in diesel exhaust. They reached a final conversion deviation around 0.1% and 5.2% for CO and total HCs respectively over New European Driving Cycle (NEDC) [101]. In another study, Sampara et al. [102], adjusted the site density to match the light-off in a DOC for automotive diesel applications due to the differences in the ageing status that the reactor-scale and full-scale sample may have.

The transformation of the model from reactor-scale to full-scale component requires some modifications; however, in the current study the goal is to use the same kinetic constants of the reactor-scale component without tuning. Therefore, it is required to detect the source of mismatching and limitations between reactor-size and full-size models in order to find physical explanation and solutions:

- Although 1D models with uniform flow pattern are beneficial in terms of computational time, absence of pore diffusion model in washcoat layer may lead to higher conversions [96,103].
- Temperature distribution influences the kinetics in a significant way. Radial temperature profile and hence radial concentration profiles are observed in 3D simulations of catalysts [104], [105]. In addition, variation of Peclet number between full size and lab-scale component affects the heat and mass transfer phenomena [106].
- Compared to lab-scale model, the engine exhaust gas includes a mixture of different gas species entering the reactor which affect the behavior of the catalyst, especially as far as the HC speciation is concerned [104].
- External heat transfer in the lab scale sample is negligible, while in full size component it can have not negligible effects [106], [104].
- Ageing status of the catalyst component under investigation may differ from reactor-scale tests and full-size measurements using engine-out emissions, which can highly impact the kinetics [102].

4.2 Model refinements

In the current study, after preliminary analysis of experimental data, the following assumptions and refinements are applied in order to reduce the gap between measured and simulated results when transferring the reactor-size model to full-scale model.

The assumptions include:

- The same kinetic parameters for the NO_x Storage and Reduction (NSR) test and Oxygen Storage Capacity (OSC) mechanisms are transferred from reactor-scale model without any modifications.
- NO_x mass flow rate was calculated using the NO_2 molar mass, due to the characteristics of Chemi-Luminescence Detectors (CLD), and without any correction related to the test cell temperature and humidity since all the tests were carried out at standard condition, 25 °C, 50% humidity.
- Engine-out hydrocarbons are characterized by a defined ratio of diesel fuel (high molecular weight HC, such as dodecane or decane) and propylene considering only the Non-Methane HC (NMHC) portion both at the inlet and the outlet of LNT.

The refinements include:

- Due to the fact that high molecular weight HC, dodecane, was not included in the reactor-scale characterizations, the oxidation kinetic parameters are imposed initially from literature [34,102] and further calibrated according to measured LNT outlet HC concentrations.
- Moreover, CO oxidation rate also depends on the pre-conditioning (different Rh oxidation state) [107] and level of H_2 in the gas feed [99], which can be different from real driving condition. Therefore, slight re-calibration for CO oxidation parameters can be performed.
- The simulations of the full-size model were run based on the aged reactor-scale kinetics.
- The H_2 concentration at LNT in/out are not available from measurements and therefore are estimated from CO and CO_2 emissions. The estimated values during lean part are not consistent with literature [99], CO/H_2 between 40-50, while the estimated one shows CO/H_2 around 4 (one order of magnitude lower). However, the estimated H_2 concentration during rich pulses are acceptable. In order to avoid imposing uncertainty, H_2 concentration is assumed to be 0 during lean part and equal to estimated value during rich pulse.
- NO_x reduction reactions, regardless of CO, H_2 or HC, are expected to have low rate during lean part of the cycle in which O_2 concentration is high. To take this effect into account, according to literature [72–74] NO_x reduction reactions are inhibited by an inhibition function of the type $1 + kC_{O_2}$ in which k is represented with an Arrhenius function. Since reactor-scale tests do not include O_2 during NO_x reduction phase, the results of lab-scale model will be preserved.

- External heat transfer model is built in order to account for the thermal loss across the catalyst, if the isothermal condition is not satisfied.

4.3 Experimental data

The experimental tests are performed on a roller test bench for two different aftertreatment configurations: A) LNT + DPF; and B) LNT + SCR-F. The position of outlet concentration measurements for architecture A is after DPF (which does not affect NO and NO_2 concentrations, while CO and HC concentrations may change from LNT out position) and for the architecture B is after LNT. The characteristics of the systems are reported in Table 33 and the geometric information are expressed in Table 34. The samples are exposed to pre-cleaning condition in order to remove any stored NO_x prior to start of the test, however, in one sample intentionally a partially filled sample is used to assess the impact of initial storage on the performance of the component. Moreover, the cases with and without $DeNO_x$ events have been examined to evaluate the effectiveness of regeneration to restore NO_x storage capability of the system. The washcoat composition, substrate properties and PGM loading are consistent with the reactor-scale components tested in SGB measurements. The samples are sulphur free and therefore the effect of sulphur loading can be neglected.

Table 33. Characteristics of the full-size components under study

Type	AT System	PGM Loading [g/ft^3]	Substrate [cpsi/mil]	PGM Ratio [Pt:Pd:Rh]	Initial Trapping	DeNOx Events
A-1	cc(LNT+DPF)	120	400/4	103:12:5	Empty	Yes
B-1	cc(LNT+SCR-F)	120	400/4	103:12:5	Empty	No
B-2	cc(LNT+SCR-F)	120	400/4	103:12:5	Partially Filled	No

Table 34. Geometric information of the two aftertreatment systems under study for full-size experiments over driving cycles

Type	AT System	Long dia. x Short dia. x Length [mm x mm x mm]	Substrate Frontal Area [mm^2]	Substrate Volume [L]
A-1	cc(LNT+DPF)	165.6 x 129.6 x 85	17633.3	1.50
B-1	cc(LNT+SCR-F)	125 x 125 x 100	12271.9	1.23
B-2	cc(LNT+SCR-F)	125 x 125 x 100	12271.9	1.23

The measurements are performed over cold Worldwide harmonized Light vehicles Test Cycle (WLTC), the main characteristics of which are reported in Table 35. The WLTC is composed by 4 phases including low, medium, high and extra high portions with a duration of 1800 seconds.

Table 35. Characteristics of WLTC Class 3b [108]

Phase	Max. Velocity	Ave. Velocity (no stops)	Ave. Velocity (with stops)	Stop Duration	Duration	Distance
	[km/h]	[km/h]	[km/h]	[s]	[s]	[km]
Low	56.5	25.7	18.9	156	589	3.095
Medium	76.6	44.5	39.5	48	433	4.756
High	97.4	60.8	56.7	31	455	7.162
Extra High	131.3	94	92	7	323	8.254
Total	-	-	-	242	1800	23.266

4.4 Results and discussions

For the sake of simplicity, the analysis is started from the case which does not include any regeneration events and before starting the WLTC, a cleaning purge is applied in order to remove any prior NO_x trapping effects; therefore, B-1 configuration is selected. Afterwards, in order to model the component with primary NO_x storage, the final values of site storage coverages at the end of WLTC for the B-1 configuration are used as the input for the initial site coverages of B-2 configuration for all the sites including $Ba^{I}O$, $Ba^{II}O$, $Ba^{II}(NO_2)_2$, $Ba^{III}O$ and Ce_2O_3. It should be considered that the other barium nitrate coverages and CeO_2 can be calculated considering that the sum of coverages for each site including Ba^{I}, Ba^{II}, Ba^{III} and Ce, equal to 1. It is worth mentioning that comparison between predicted and measured instantaneous concentrations has also been performed; however, due to confidentiality reasons only cumulative comparison is presented.

More in detail, a comparison between cumulative NO_x mass of aftertreatment configuration B over WLTC, without any regeneration events, is presented in Figure 54-a for both empty and partially filled component in terms of initial NO_x trapping condition. It can be observed that the simulation model can predict the NO_x mass over WLTC with acceptable accuracy with the total error not exceeding 6%. Moreover, it can be clearly observed that the B-2 configuration, data related to the component with initial NO_x storage represented with dashed lines, results in higher cumulative NO_x at the outlet of LNT, especially in the low and medium portions in which the difference between inlet and outlet NO_x is minor; which is due to the fact that a part of NO_x storage sites are previously occupied by initial storage, while the empty initial trapping condition component, B-1, is capable to reduce NO_x both at low temperature and higher temperature portions of WLTC and the model is able to capture the effect of initial storage successfully. In addition, it can be realized that most of the NO_x slip occurs during high and extra-high portions of WLTC, starting from $t = 1477$ seconds

Focusing on Figure 54-b, related to cumulative NO_x mass for configuration A, it can be observed that although the component is exposed to higher inlet cumulative NO_x mass (with a total of around 8 gr) with respect to configuration B (around 5.1 gr), thanks to rich events LNT is capable to recover its storage capacity and reduce NO_x to 2.7 gr which is well-captured by the model showing a total error around 4.5%.

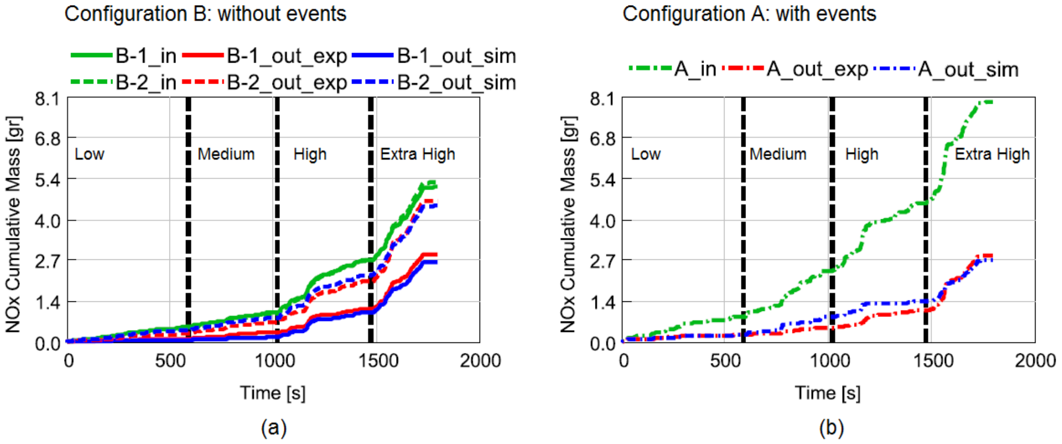

Figure 54. Cumulative NO_x mass for a) Configuration B over WLTC, dashed lines represent the case with initial NO_x storage and full lines represent the empty initial NO_x trapping condition; b) Configuration A, with rich events and empty initial NO_x storage

Finally, temperature profiles at the inlet and outlet of the LNT are compared to measured data in Figure 55. It can be observed that temperature levels for the cases without any rich events, Figure 55-a and Figure 55-b have lower peak temperatures, around 300°C; however, when several regenerations events are imposed, Figure 55-c, the temperature is increased, up to 420°C, during the events to higher values and the thermal model is capable to predict the temperatures with good satisfactory accuracy. Moreover, comparing Figure 55-a and Figure 55-b, as expected, presence of initial NO_x storage does not impact temperature profiles.

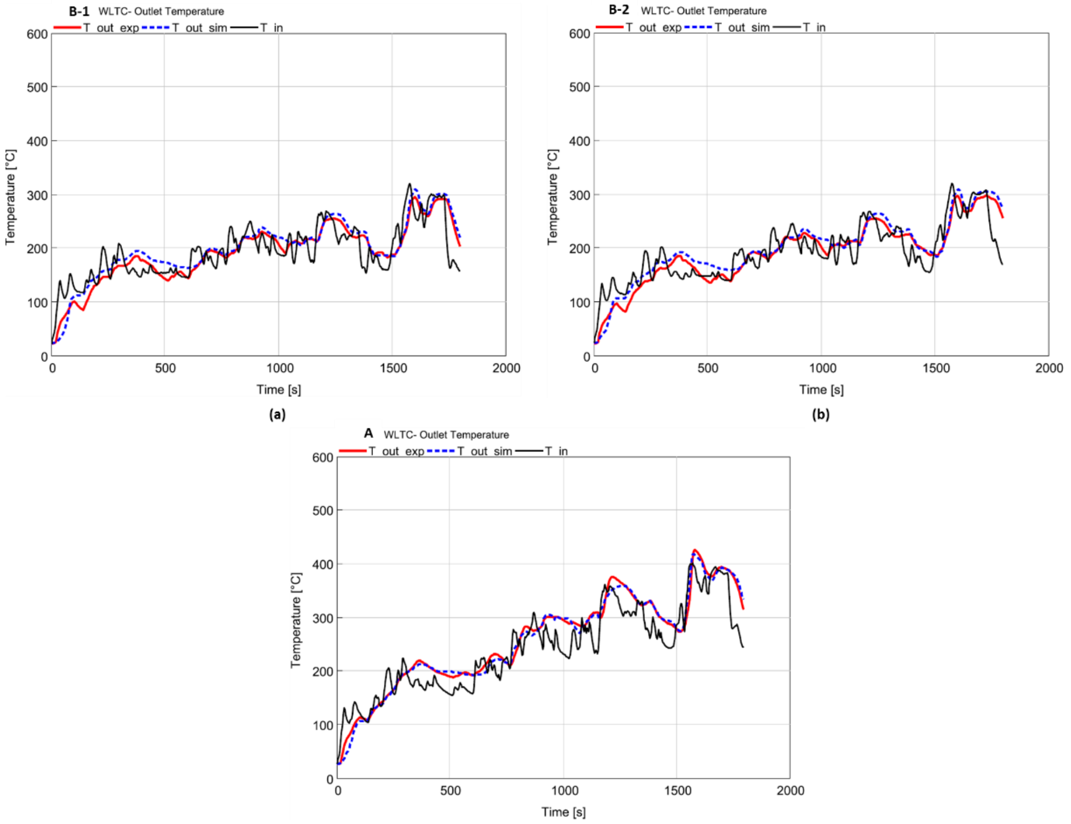

(a) (b) (c)

Figure 55. Temperature profiles at the inlet (black) and the outlet of LNT from simulation (blue-dashed lines) and experiments (red-full lines) for a) configuration B-1: no events, no initial trapping; b) configuration B-2: no events, initial NO_x storage is present; c) configuration A: no initial trapping, regeneration events are present

Chapter 5

Grey-box ECU/Hardware in Loop Capable LNT model

5.1 Model development

Considering that the complexity of emission control technologies has been increased during last decades, in order to maximize the efficiency of such aftertreatment systems, under the highly transient conditions which occur in real driving operation, model-based control is required. Such techniques use instant information about the state of the reactors to calculate the control output and therefore will require accurate and fast running reactor-plant models. In this section, the LNT model calibrated using GT-SUITE in Section 3.2 is linearized with the aim to be used in ECU/ Hardware-in-the-Loop (HiL) applications as the reactor-plant model.

In order to reduce the model to be used in ECU/HiL applications, it is required to apply reasonable assumptions to linearize coupled non-linear Partial Differential Equations (PDEs) to algebraic equations which can be solved by explicit solvers such that a balance between accuracy of detailed models and efficiency of black-box models is achieved:

- Since the heat of reaction is negligible, non-isothermal effects can be ignored and therefore constant thermodynamic properties are used.
- Since the reaction rates are controlled by external (i.e. fluid to wall) mass transfer at high temperatures, two phase model is used.

- Considering that the transvers Peclet number ($Pe = \frac{uR_\Omega}{LD_f}$) is less than 0.1, entrance length effects are neglected; hence, constant heat and mass transfer coefficients for a rounded square channel are used [29].
- The washcoat diffusional limitations (concentration gradients in the washcoat) are neglected and lumped into kinetic parameters (convert 1+1D → 1D)
- Quasi-steady approximation is used, considering that the accumulation in fluid phase can be ignored → elimination of transient terms in fluid phase species balances.
- Block-in-series approach is adopted to ignore axial gradients in each block (convert 1D → 0D) such that the output signal of each block is used as the input to the subsequent block, Figure 56.

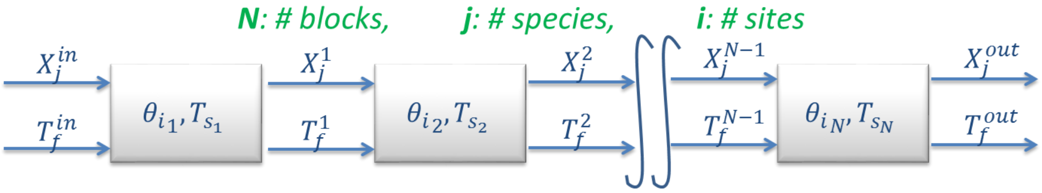

Figure 56. Block-in-series approach

Therefore, the governing equations presented in Section 1.2 are reduced. The base simplifications of the governing equations for a 1D-CFD model are derived from an SCR model developed by Santhosh et al. [29]. Species balance equations, Equation 30 and Equation 32 which results in simplified forms of Equation 31 and Equation 33, respectively:

$$\begin{aligned} Gas:\ \varepsilon \frac{\partial X_{wc_i}}{\partial t} &= \frac{1}{C_0}\alpha_i^T r + D_s \frac{\partial^2 X_{wc_i}}{\partial y^2} \\ &\rightarrow \frac{1}{C_0}\alpha_i^T r + \frac{k_{me}}{\delta_c}\left(X_{fm} - X_{wc}\right) = 0 \end{aligned} \tag{30}$$

Which results in:

$$X_{fm} = -\frac{\delta_c}{C_0 k_{me}}\alpha_i^T r + X_{wc} \tag{31}$$

$$\begin{aligned} Solid:\ \frac{\partial X_{fm_i}}{\partial t} &= -u\frac{\partial X_{fm}}{\partial x} - \frac{k_{me}}{R_\Omega}\left(X_{fm} - X_{wc}|_{y=0}\right) \\ &\rightarrow \frac{u}{L}\left(X_{fm} - X_{fm}^{in}\right) + \frac{k_{me}}{R_\Omega}\left(X_{fm} - X_{wc}\right) = 0 \end{aligned} \tag{32}$$

Which results in:

$$X_{wc} = (1+P)X_{fm} - PX_{fm}^{in} \tag{33}$$

Where:

$$P = \frac{uR_\Omega}{Lk_{me}} \tag{34}$$

Using Equation 31 and Equation 33, X_{wc} can be calculated from Equation 35:

$$X_{wc_i} = X_{fm_i}^{in} + \frac{1}{FPP}\alpha_i^T r \tag{35}$$

Where the parameter FPP is defined by Equation 36:

$$FPP = \frac{C_0 k_{me}}{\delta_c}\left(\frac{P}{1+P}\right) \tag{36}$$

Site balance equation partial derivative will be converted to Equation 37:

$$\begin{cases} \dfrac{d\theta_k}{dt} = \dfrac{1}{C_s}\alpha_{\theta_k}^T r \\ \displaystyle\sum_k \theta_k = 1 \qquad for\ each\ site \end{cases} \tag{37}$$

The gas phase energy balance is simplified as Equation 38:

$$\frac{u}{L}\left(T_f - T_f^{in}\right) + \frac{h}{R_\Omega \rho_f C_{pf}}\left(T_f^{out} - T_s\right) = 0 \rightarrow T_f^{out} = \frac{T_f^{in} + \dfrac{hL}{uR_\Omega \rho_f C_{pf}}T_s}{1 + \dfrac{hL}{uR_\Omega \rho_f C_{pf}}} \tag{38}$$

The solid phase energy balance is simplified as Equation 39:

$$\delta_w \rho_w C_{pw}\frac{dT_s}{dt} = h\left(T_f^{out} - T_s\right) \tag{39}$$

Substituting Equation 38 in Equation 39 results in Equation 40:

$$\delta_w \rho_w C_{pw}\frac{dT_s}{dt} = \frac{h\left(T_f^{in} - T_s\right)}{1 + \dfrac{hL}{uR_\Omega \rho_f C_{pf}}} \tag{40}$$

Considering the kinetic scheme presented in Section 3.2 the parameters to be solved in each time step and for each block is listed as follows and therefore the full detailed system contains 16 PDEs:

- Concentrations: NO, NO_2, NH_3, N_2O, H_2, CO, C_3H_6, Heavy HC, O_2 → 9 unknowns
- Coverages: $Ba^{I}O$, $Ba^{II}O$, $Ba^{II}(NO_2)_2$, $Ba^{III}O$ and CeO_2 → 5 unknowns
- Wall and gas temperatures → 2 unknowns

The reaction expression for each species based on the defined kinetic scheme and stoichiometric coefficients is given in Equation 41 to Equation 49:

$$\begin{aligned} r_{NO} = \alpha_{NO}^T r = {} & -r_1 + r_2 - r_3 - 2r_4 + 2r_5 + 2r_8 - 2r_{10} + 2.4r_{23} \\ & + 3.2r_{25} - 1.5r_{26} - r_{27} + 2r_{31} + 2r_{34} + 2r_{36} \\ & - 9r_{37} - 18r_{38} \end{aligned} \tag{41}$$

$$r_{NO_2} = \alpha_{NO_2}^T r = r_1 - 3r_2 - 3r_3 + 2r_7 - 2r_9 + 2r_{11} + 2r_{12} \tag{42}$$

$$\begin{aligned} r_{NH_3} = \alpha_{NH_3}^T r = {} & -\frac{10}{3} r_{18} + 2r_{19} + 2r_{20} - r_{21} + 2r_{22} - 0.4r_{23} \\ & - 2r_{24} - 1.2r_{25} - r_{26} \end{aligned} \tag{43}$$

$$r_{N_2O} = \alpha_{N_2O}^T r = 1.5r_{21} + 9r_{38} \tag{44}$$

$$r_{H_2} = \alpha_{H_2}^T r = -r_{15} + r_{17} - 8r_{19} - 8r_{20} - 6r_{22} + 6r_{32} - r_{42} \tag{45}$$

$$\begin{aligned} r_{CO} = \alpha_{CO}^T r = {} & -r_{14} - r_{17} - r_{27} - 5r_{28} - 5r_{29} - 5r_{30} - r_{31} \\ & + 3r_{32} - r_{40} \end{aligned} \tag{46}$$

$$\begin{aligned} r_{C_3H_6} = {} & \alpha_{C_3H_6}^T r \\ & = -\frac{1}{9} r_{16} - r_{32} - \frac{5}{9} r_{33} - \frac{1}{3} r_{34} - \frac{5}{9} r_{35} - \frac{1}{3} r_{36} \\ & - r_{37} - r_{38} - r_{39} \end{aligned} \tag{47}$$

$$r_{Heavy\,HC} = \alpha_{Heavy\,HC}^T r = -r_{41} \tag{48}$$

$$\begin{aligned} \alpha_{O_2}^T r = {} & -0.5r_1 - 0.5r_4 + 0.5r_5 - r_6 + 0.5r_7 + 1.5r_8 - 0.5r_9 \\ & - 1.5r_{10} + 0.5r_{11} + 0.5r_{12} - 0.5r_{13} - 4.5r_{39} \\ & - 0.5r_{40} - 19.4r_{41} - 0.5r_{42} \end{aligned} \tag{49}$$

Considering that for each site, the site balance equation results in: $\sum_k \theta_k = 1$, some sites can be written as a function of the others, Equation 50 to Equation 53:

$$\theta_{Ba^I(NO_3)_2} = 1 - \theta_{Ba^IO} \tag{50}$$

$$\theta_{Ba^{II}(NO_3)_2} = 1 - \theta_{Ba^{II}O} - \theta_{Ba^{II}(NO_2)_2} \tag{51}$$

$$\theta_{Ba^{III}(NO_3)_2} = 1 - \theta_{Ba^{III}O} \tag{52}$$

$$\theta_{Ce_2O_3} = 1 - \theta_{CeO_2} \tag{53}$$

The reaction expression for each site based on the defined kinetic scheme is expressed by Equation 54 to Equation 58:

$$r_{Ba^IO} = \alpha^T_{\theta_{Ba^IO}} r = -r_2 + r_{12} + r_{19} + r_{28} + r_{33} + r_{34} \tag{54}$$

$$\begin{aligned} r_{Ba^{II}O} = \alpha^T_{\theta_{Ba^{II}O}} r \\ &= -r_3 - r_4 + r_5 + r_{11} + r_{18} + r_{21} + r_{22} \\ &+ r_{23} + r_{24} + r_{29} + r_{31} \end{aligned} \tag{55}$$

$$\begin{aligned} r_{Ba^{II}(NO_2)_2} = \alpha^T_{\theta_{Ba^{II}(NO_2)_2}} r \\ &= r_4 - r_5 - r_6 - r_{21} - r_{22} - r_{23} - r_{24} - r_{31} \end{aligned} \tag{56}$$

$$\begin{aligned} r_{Ba^{III}O} = \alpha^T_{\theta_{Ba^{III}O}} r \\ &= r_7 + r_8 - r_9 - r_{10} + r_{20} + r_{25} + r_{30} + r_{35} + r_{36} \end{aligned} \tag{57}$$

$$r_{CeO_2} = \alpha^T_{\theta_{CeO_2}} r = 2r_{13} - 2r_{14} - 2r_{15} - 2r_{16} \tag{58}$$

Finally, by using Equation 35, $X_{wc_i} = X^{in}_{fm_i} + \frac{1}{FPP}\alpha_i^T r$ PDEs for the following species are eliminated by finding a closed form solution which can be found by algebraic equations:

- N_2O
- NO_2
- H_2
- NH_3
- Heavy HC

Moreover, by using Equation 38, the gas temperature PDE is eliminated.

However, due to complexity of the kinetic scheme and presence of exponent lower than 1 for some species such as O_2, ODEs for the following species cannot be converted to algebraic equations:

- NO
- CO
- C_3H_6
- O_2

The simplified ODE for these species can be written as Equation 59:

$$\frac{dX_{wc_i}}{dt} = \frac{1}{\varepsilon}\left(\frac{km_i}{\delta_c}\left(X_{f_i} - X_{wc_i}\right) + \frac{1}{C_0} r_i\right) \tag{59}$$

Therefore, in total 10 ODEs will remain including:

- 4 PDEs for species (NO, CO, C_3H_6 and O_2) → Equation 59
- 5 PDEs for site coverages ($Ba^{I}O$, $Ba^{II}O$, $Ba^{II}(NO_2)_2$, $Ba^{III}O$ and CeO_2) → Equation 37
- 1 PDE for the solid temperature (T_s) → Equation 40

The remaining parameters will be simplified to algebraic equation as a function of the abovementioned states:

- Species N_2O, NO_2, H_2, NH_3 and Heavy HC → Equation 35
- Gas Temperature → Equation 38

The ODEs can be further converted to algebraic equations using numerical methods marching in time such as Runge-Kutta and explicit Euler method which can be handled by ECU and HiL systems. As an example, the explicit Euler is defined as follows evaluating the right-hand-side at time t, Equation 60:

$$\frac{dy(t)}{dt} = f(t, y) \rightarrow \frac{y(t + \Delta t) - y(t)}{\Delta t} = f\big(t, y(t)\big) \tag{60}$$

It is also required to select suitable time step, Δt, so that the solution converges with acceptable accuracy.

5.2 Validation of the model for LNT case study 1

Validation of the model is performed for a calibrated model on GT-SUITE, according to NO_x Storage Reduction (NSR) test, Figure 57, with following operating condition at five constant inlet temperatures ranging from 150 to 550 °C, spaced equally in 1/T [1/K].

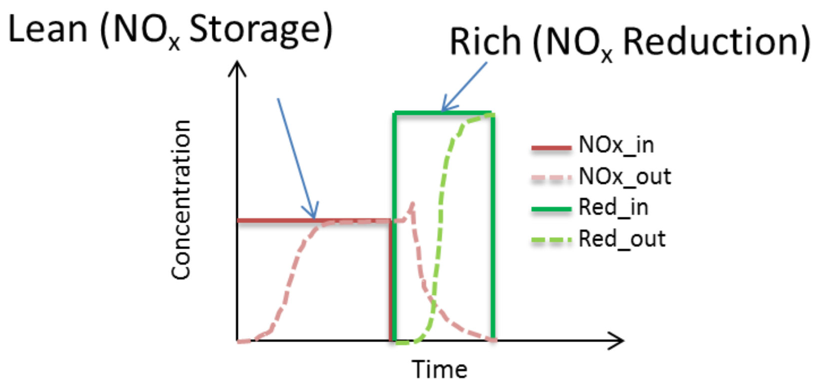

Figure 57. Schematic view of NSR experiment

The Composition of the feeding is reported in Table 36.

Table 36. Inlet gas composition for NO_x reduction experiments in volume basis

Species	**Lean**	**Rich, H_2**	**Rich, CO**	**Rich, HC**
Reductant [ppm]	0	1000	1000	111
O_2 [%]	10	0	0	0
CO_2 [%]	5	5	5	5
H_2O [%]	5	5	5	5
NO [ppm]	287	0	0	0
NO_2 [ppm]	13	0	0	0
N_2	Balance	Balance	Balance	Balance

The settings of the model set-up are as follows:

- Number of sub-volumes: 10
- Time step: 0.0002 seconds
- Processor: *Intel (R)Core(TM) i7 – 4600U CPU @2.10GHz 2.70 GHz*

The GT-SUITE model has been calibrated using SGB experimental data and therefore the calibrated kinetic parameters from previous study [16], which matches the measurements with satisfactory accuracy, are used. The comparison of the GT-SUITE model with the reduced-order grey box model presented in this work for NSR test are depicted in Figure 58, Figure 59 and Figure 60 for H_2, CO and C_3H_6 reductants, respectively.

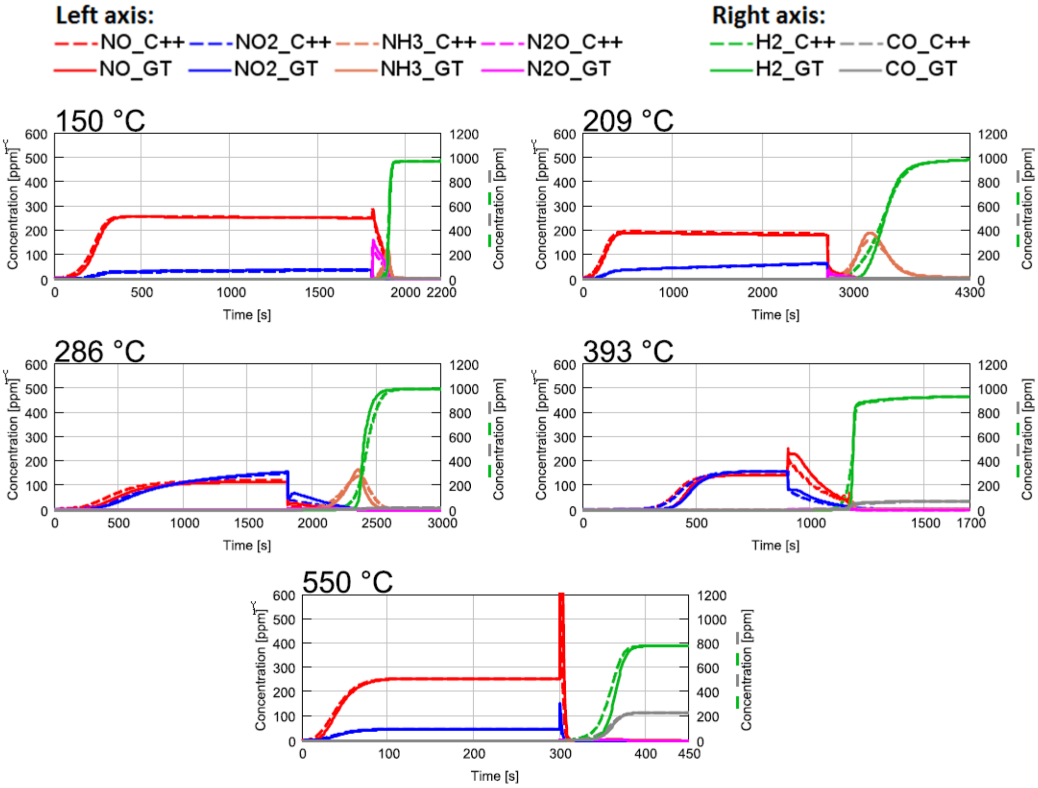

Figure 58. Comparison of NSR test results between GT-SUITE and reduced-order models, H_2 used as the primary reductant

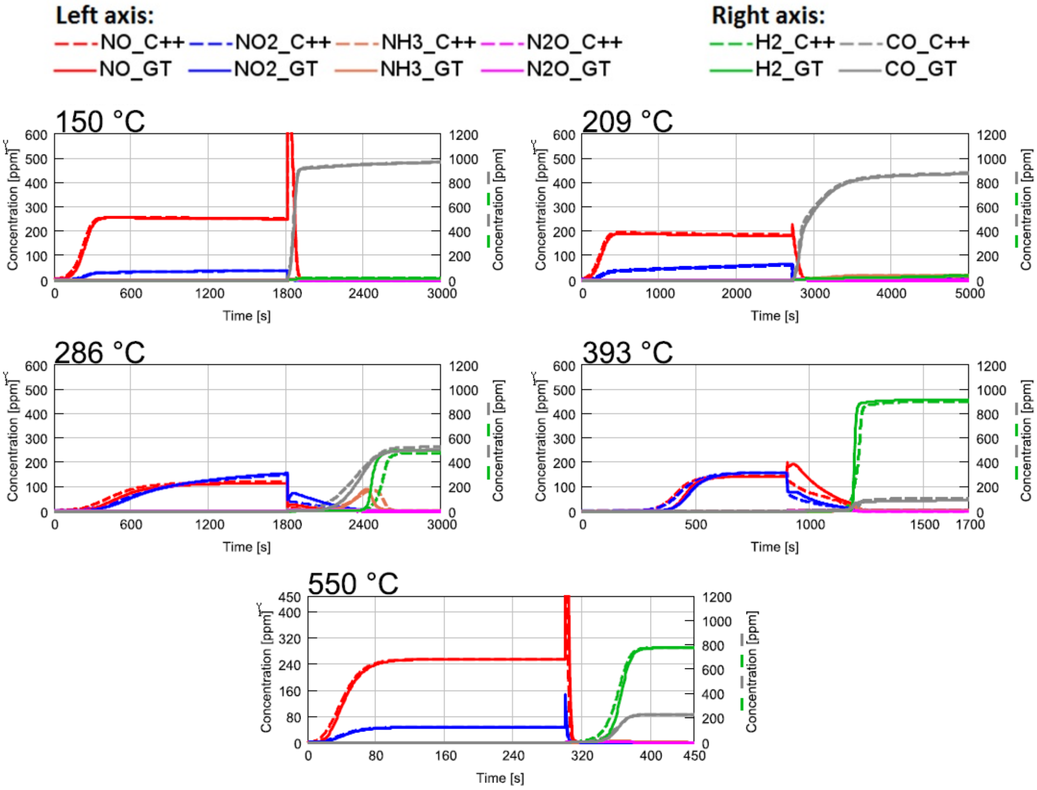

Figure 59. Comparison of NSR test results between GT-SUITE and reduced-order models, CO used as the primary reductant

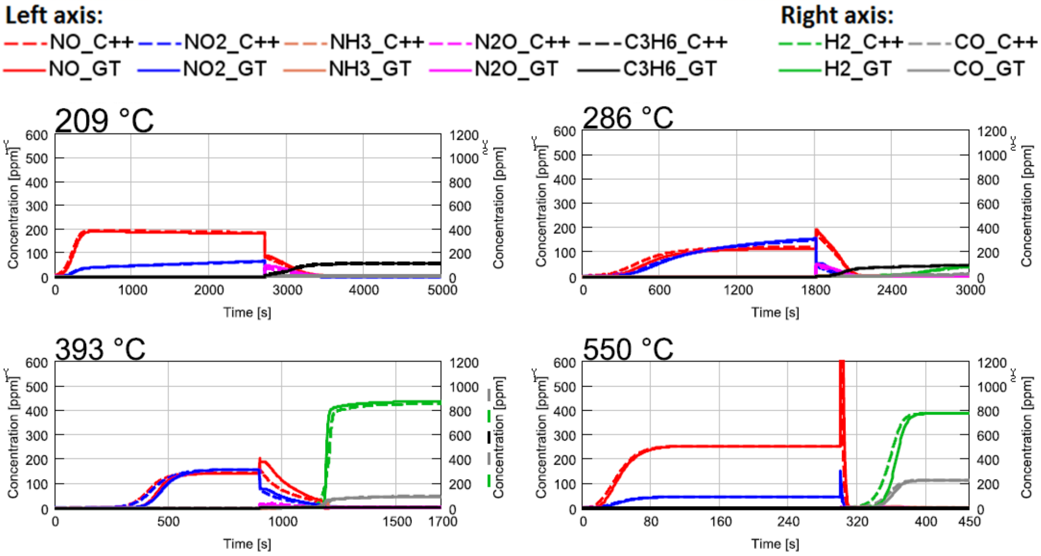

Figure 60. Comparison of NSR test results between GT-SUITE and reduced-order models, C_3H_6 used as the primary reductant

As an example, comparison between simulation run time and real time for the NSR test in which H_2 is used as the primary reductant is shown in Figure 61.

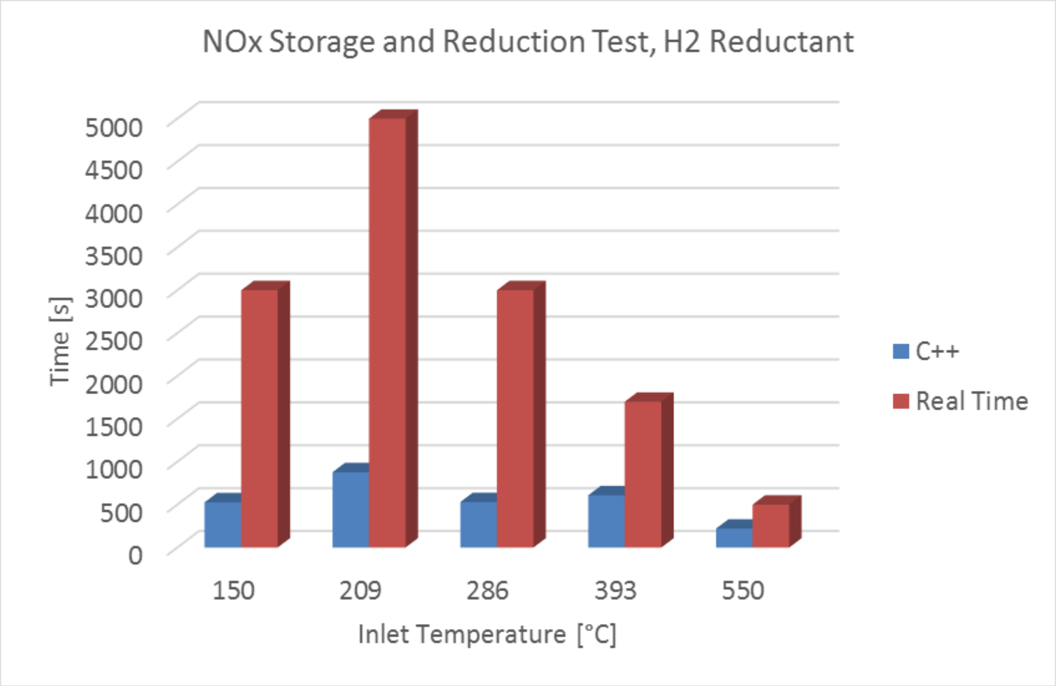

Figure 61. Simulation run time versus real time for NSR test

5.3 Sensitivity analysis

The sensitivity of the results and simulation run time with respect to the number of blocks is performed.

According to Figure 62 it can be observed that the results for 10 blocks is very close to 15 blocks, while the run time is almost half. If the number of blocks are very low, the accuracy deteriorates while the CPU hours will be highly improved and therefore for obtaining accurate results re-calibration of kinetic parameters would be required.

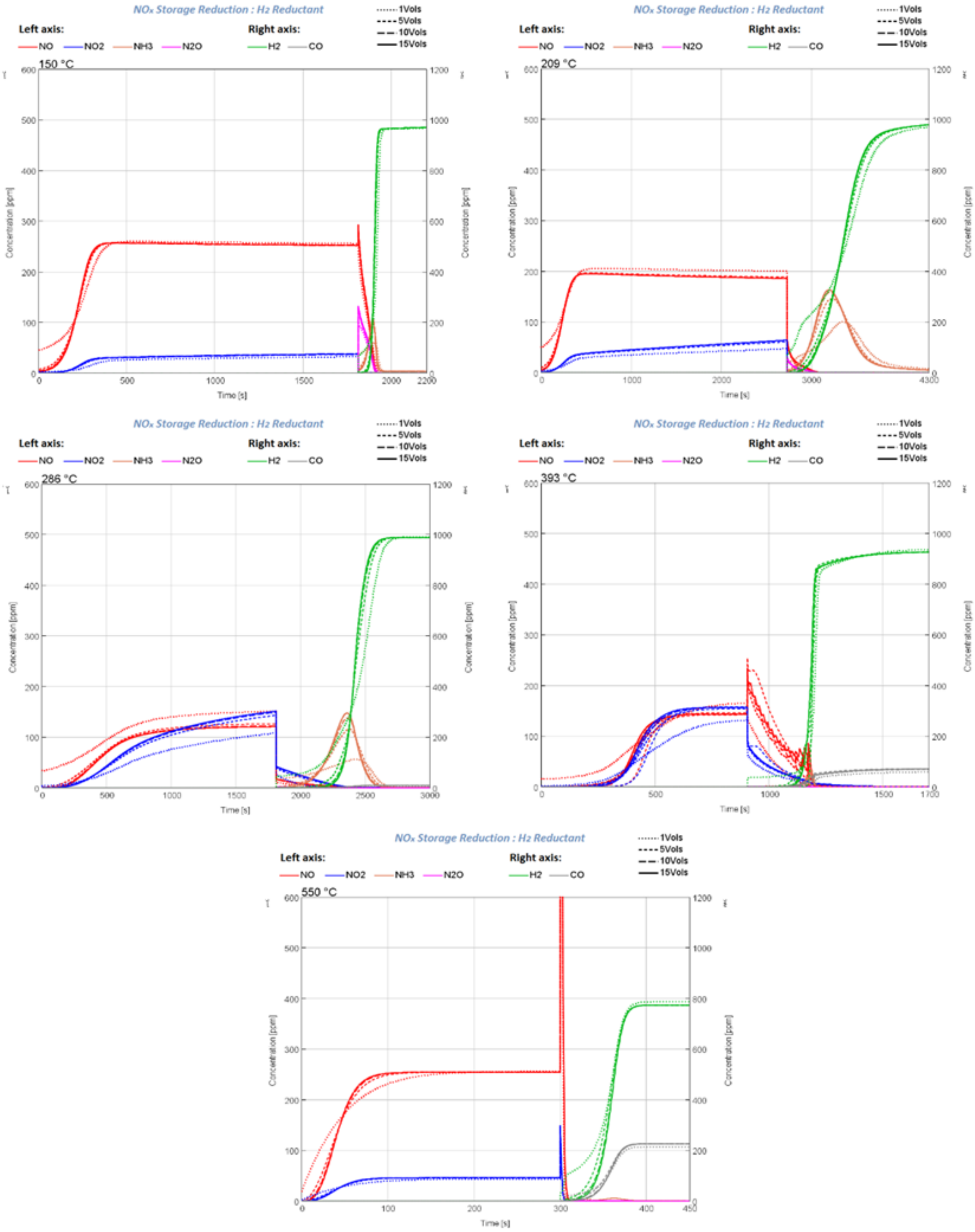

Figure 62. Sensitivity of NSR results (H_2 reductant) to number of blocks

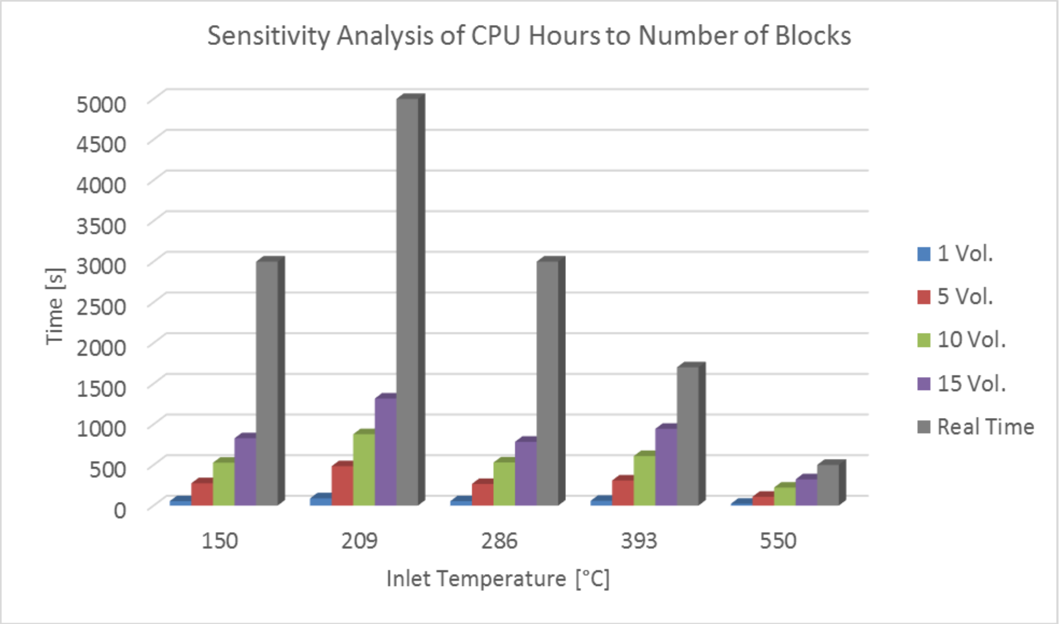

Figure 63. Comparison of simulation run time versus real time varying number of axial sub-volumes/blocks

It should be noted that considering that in GT-SUITE solver since all the partial differential equations do not need to be linearized, it runs faster than the current grey-box model thanks to possibility of using larger time step. However, that it is possible to further reduce the presemted grey-box model to acheive faster speed. Moreover, as depicted in Figure 62, by using lower number of sub-volumes and re-tuning of kinetic parameters to preserve the simulation results, larger time step can be selected and therefore the run time can be improved significantly.

Chapter 6

Application of Genetic Algorithm for Calibration of Diesel Oxidation Catalyst Kinetics

6.1 Introduction to Diesel Oxidation Catalyst

Diesel Oxidation Catalyst (DOC) are used with the aim to reduce CO and HC emissions in addition to conversion of NO to NO_2 [4] which can improve the performance of downstream aftertreatment devices such as SCR [47,53] by moving the kinetics towards fast SCR through increase in the amount of NO_2 and therefore bringing the NO_2/NO ratio closer to equimolar condition [5].

Generally, DOCs contain a storage material such as zeolite which can store hydrocarbons at low temperature when the light-off has not yet been reached and desorb them at higher temperatures; thus, increasing the cold start efficiency [6–8]. Moreover, oxidation reactions take place over the Platinum Group Metals (PGM) which is normally a mixture of Pt and Pd [109–111].

Several experimental and numerical studies have been performed regarding the performance of DOC to reduce CO and HC emissions of diesel engine exhaust. Micro-kinetic or detailed models are more accurate, however such models are more complex such as the model proposed by Sharma et al. [112] which takes into account mainly oxidation reactions over Pt. However, several global kinetic models were proposed in the literature [34,110,113] which are simpler and if calibrated properly can be used for quite accurate prediction of emissions downstream of the catalyst. To calibrate the kinetic model, experimental tests are performed which can either be based on real exhaust using engine-out emissions as the input to the catalyst [4,35,114] or reactor-scale synthetic gas bench tests in which controlled species concentrations, mass flowrate and temperature can be imposed [6,115,116].

In this chapter, the performance of two DOC cores with different washcoat composition has been analyzed both experimentally and numerically. The experimental data, coming from synthetic gas bench tests on reactor-scale component, were used for the calibration of the global kinetic model built in 1D CFD software, GT-SUITE. The kinetic model was calibrated using Genetic Algorithm optimization tool, embedded in GT-SUITE, which is more successful in finding global optimum, rather than being trapped in local optimums.

6.2 Experimental tests

The experimental activity has been performed using SGB measurements with controlled inlet temperature, mass flowrate and species concentrations aiming to minimize the interaction of each reaction on the others by dosing specific species in the inlet batch and thus facilitating the kinetic model calibration.

The concentrations of species including CO, CO_2, O_2, C_3H_6 [ppmC_3], $C_{10}H_{22}$ [ppmC_{10}], NO, NO_2 and N_2O at the outlet of the cores are recorded by FTIR measurements. Total HC is also measured from MEXA in [ppmC_3] basis. However, inlet concentrations are assumed to be the same as nominal values. Moreover, inlet and outlet gas temperatures are also measured by K-type thermocouples.

Due to zone coating of the considered component, the reactor data refer to two core samples with different washcoat loadings: one extracted from the front zone (first half of the full-size brick, which contains zeolite coating and therefore is capable of HC storage), the other one mined from the rear zone (second half of the full-size brick, which does not contain zeolite). The characteristics of the cores are reported in Table 37. The components are oven aged. The samples are placed into an isothermal furnace.

Table 37. Characteristics of reactor-scale DOC samples

Characteristic	**Unit**	**Front Core**	**Rear Core**
Core size: diameter x length	in x in	1 x 3	1 x 3
PGM	[-]	Pt and Pd	Pt
Cells density	[cpsi]	400	400
Wall thickness	[mil]	4.5	4.5
Substrate material	[-]	Cordierite	Cordierite
Zeolite coating	[-]	Yes	No

The experimental test protocols can be categorized in two main groups including HC storage and light-off experiments.

6.2.1 HC storage tests

Previous studies have shown that mainly high molecular HCs are stored on zeolite such as decane, while low molecular weight HCs such propylene do not show adsorption/desorption behavior on zeolite in the presence of heavy HCs [6,103]. Therefore, only decane is used as the representative of high molecular weight HC in storage tests. The test is performed using different HC concentrations 400 and 800 [ppmC_1] $C_{10}H_{22}$ with the base feed composition of 4.5% H_2O, 4.5% CO_2, Balanced N_2 and at constant standard Space Velocity (SV) of 30,000 1/hr referred to pressure of 1 atm and temperature of 273.15 K.

The HC storage experiment is performed through a Temperature Programmed Desorption (TPD) test consisting of two phases, as it can be observed in Figure 64:

- Adsorption phase in which the temperature is kept constant and is continued until saturation of adsorption sites, zeolite, is reached and the outlet concentration of HC reaches the inlet one. Two starting inlet gas temperature was selected for the adsorption phase, 90 and 120 °C.
- Temperature ramp phase in which after the saturation of storage sites, the temperature is ramped linearly up to 400 °C with a constant rate of 5 K/min.

It is worth mentioning that storage test has been carried out only for the front core, since the rear one is without zeolite which is not capable to store HCs.

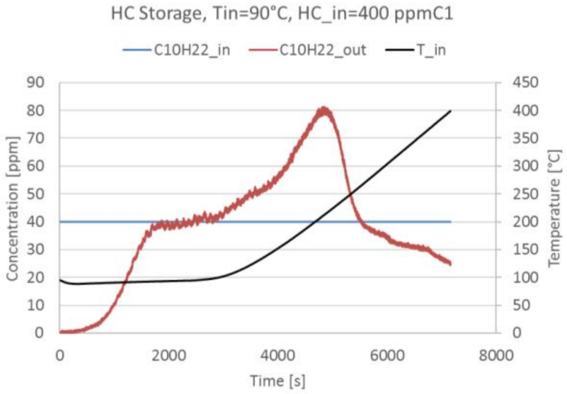

Figure 64. An example of HC storage experiment for the front core

6.2.2 Light-off tests

Light-off tests are performed over a temperature ramp starting from 80 °C up to 400 °C with a constant rate of 5 K/min carried out at two levels of standard space velocity, 30,000 and 60,000 1/ hr referred to pressure of 1 atm and temperature of 273.15 K. Inlet feed gas composition is varied from single trace species to more complex tests in which several trace species are present in the inlet batch. The standard feed composition contains 12% O_2, 4.5% H_2O, 4.5% CO_2, Balanced N_2 and the trace species as reported in Table 38. It is worth noting that some of the tests in Table 38 are used for calibration and some are used for validation. Moreover, presence of tests with different levels of concentrations of a specie will provide sufficient information for calibration of inhibition terms.

Table 38. Trace species composition for light-off test in volumetric basis

Test ID	**CO**	**C_3H_6**	**$C_{10}H_{22}$**	**NO**	**NO_2**
#	[ppm]	[ppmC_1]	[ppmC_1]	[ppm]	[ppm]
1	800				
2	1500				
3	800	200			
4	800		400		
5	800	200	400		
6	800			100	
7	800			100	100
8	800	200	400	100	100
9		200			
10		400			
11		200		100	
12		200		100	100
13	500	200		100	100
14			400		
15			800		
16			400	100	
17			400	100	100
18	800		400	100	100
19				100	
20				200	
21		200	400	100	
22	800	200	400	100	
23	1500	300	600	100	

An example of light-off test is depicted in Figure 65.

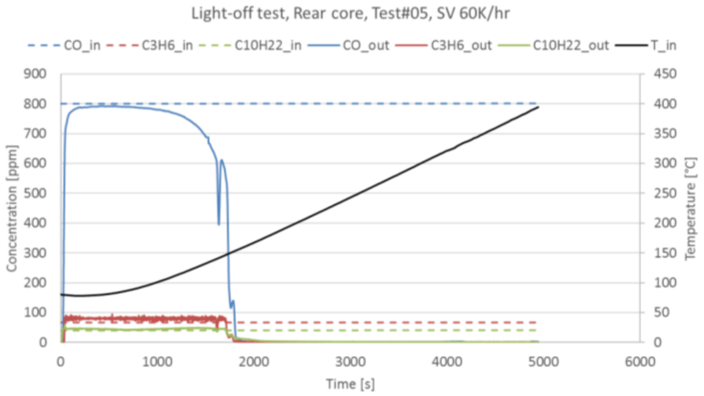

Figure 65. An example of light-off test for the rear core, using inlet composition of test #05 at standard space velocity of 60,000 1/hr

6.3 Kinetic model development and calibration

A global reaction model was defined and calibrated in 1D CFD software GT-SUITE. The specific reaction rates or the turnover number rate (R_i) is expressed in units of mol/mol-site/sec, where mol-site is the active site density participating in the reaction. Site densities were calibrated, at the same time, with the pre-exponent multipliers to match measurement data. Unless otherwise noted, all rates were assumed to be first order with respect to each reactant concentration. The Arrhenius expression was chosen for the form of the kinetic rates, Equation 7. The reaction model includes HC adsorption/desorption reactions on zeolite, water gas shift, steam reforming, oxidation reactions and NO_x reduction via HC as reported in Table 39 [101,103,110,117].

Table 39. Reaction model for the DOC component

#	Site	Reactions
1	Zeolite	$Z + C_{10}H_{22} \rightarrow Z - C_{10}H_{22}$
2	Zeolite	$Z - C_{10}H_{22} \rightarrow Z + C_{10}H_{22}$
3	PGM	$CO + 0.5O_2 \rightarrow CO_2$
4	PGM	$C_3H_6 + 4.5O_2 \rightarrow 3CO_2 + 3H_2O$
5	PGM	$C_{10}H_{22} + 15.5O_2 \rightarrow 10CO_2 + 11H_2O$
6	PGM	$NO + 0.5O_2 \rightarrow NO_2$
7	PGM	$C_3H_6 + 9NO_2 \rightarrow 9NO + 3CO_2 + 3H_2O$
8	PGM	$C_{10}H_{22} + 31NO_2 \rightarrow 31NO + 10CO_2 + 11H_2O$

9	PGM	$CO + NO_2 \rightarrow NO + CO_2$
10	PGM	$C_3H_6 + 9(1 + y')NO \rightarrow 3CO_2 + 3H_2O + 4.5(1 - y')N_2 + 9y'N_2O$
11	PGM	$C_{10}H_{22} + 31(1 + y'')NO \rightarrow 10CO_2 + 11H_2O + 15.5(1 - y'')N_2 + 31y''N_2O$

The reaction rate expression for each reaction listed in Table 39 is reported in Table 40. It is worth mentioning that I_i is the inhibition function of each reaction. Suitable inhibition terms are defined such that the behavior of the system can be simulated by the model; however, due to confidentiality reasons the form of inhibition terms are not expressed.

Table 40. Reaction rate expressions for the DOC component

#	**Reaction Rate**
1	$A_1 C_{C_{10}H_{22}}\left(1 - \theta_{C_{10}H_{22}}\right)$
2	$A_2 \exp\left(-\frac{E_2}{RT}\right)\theta_{C_{10}H_{22}}$
3	$A_3 \exp\left(-\frac{E_3}{RT}\right)C_{CO}C_{O_2}/I_3$
4	$A_4 \exp\left(-\frac{E_4}{RT}\right)C_{C_3H_6}C_{O_2}/I_4$
5	$A_5 \exp\left(-\frac{E_5}{RT}\right)C_{C_{10}H_{22}}C_{O_2}/I_5$
6	$A_5 \exp\left(-\frac{E_5}{RT}\right)C_{C_{10}H_{22}}C_{O_2}/I_5$
7	$A_7 \exp\left(-\frac{E_7}{RT}\right)C_{C_3H_6}C_{NO_2}/I_7$
8	$A_8 \exp\left(-\frac{E_8}{RT}\right)C_{C_{10}H_{22}}C_{O_2}/I_8$
9	$A_9 \exp\left(-\frac{E_9}{RT}\right)C_{CO}C_{NO_2}/I_9$
10	$A_{10} \exp\left(-\frac{E_{10}}{RT}\right)C_{C_3H_6}C_{NO}/I_{10}$
11	$A_{11} \exp\left(-\frac{E_{11}}{RT}\right)C_{C_{10}H_{22}}C_{NO}/I_{11}$

The calibration was performed using Genetic Algorithm embedded in GT-SUITE with the aim to minimize the objective function defined as the cumulative absolute error between simulated and measured outlet concentration of different species. In order to find the kinetic parameters, it is required to define a sequential calibration strategy and categorize the reaction model into several steps according to the test protocol so that in each step of the calibration the number of independent variables (unknowns) are reduced as much as possible and the reactions can be isolated using primary single species test, and then moving to more complex gas mixtures to calibrate the interaction of different species on each other. Therefore, the calibration was performed using the following sequence: It should be noted that overall 46 parametes are unknown, including 18 pre-exponent mutlplier, 17 activation energies, 9 exponents for the inhibition terms and 2 site densities.

1. Adsorption/desorption kinetic parameters, A_1, A_2, E_2, in addition to zeolite site density are found using the TPD test data with the aim to minimize the objective function defined by Equation 61. A population size of 16, 20 generations and mutation rate of 0.25 (defined based as 1 over number of independent variables) were selected for the GA optimization settings.

$$F_{obj} = \int_0^{t_1} \left|(C_{C_{10}H_{22}})_{sim} - (C_{C_{10}H_{22}})_{meas}\right| dt \tag{61}$$

It is worth mentioning that t_1 is selected such that only the effect of adsorption/desorption is considered and the effect of steam reforming and water gas shift can be neglected, around 5000-5200 seconds marked with red circle in Figure 66. Considering that in real driving operating condition, lean exhaust and excess of O_2, after light-off is reached the rate of oxidation reactions are much higher than steam reforming and water gas shift and therefore the mentioned reactions do not play a significant role. Moreover, as it can be observed in Figure 66, at lower temperatures WGS and SR are not active. Therefore, either the reactions can be neglected from the kinetic model or can be calibrated after determination of PGM site density, step 2, focusing on CO and decane traces.

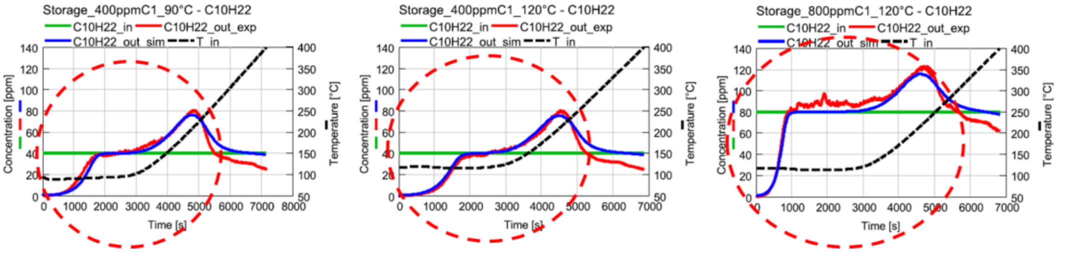

Figure 66. Comparison between simulated and measured decane concentration in TPD test for the front core, characterization of HC trapping

As an example, the progress of objective function and independent variables for the front core sample are shown in Figure 67. It can be observed that after a certain number of iterations, the objective function and independent variables converge to the optimized values.

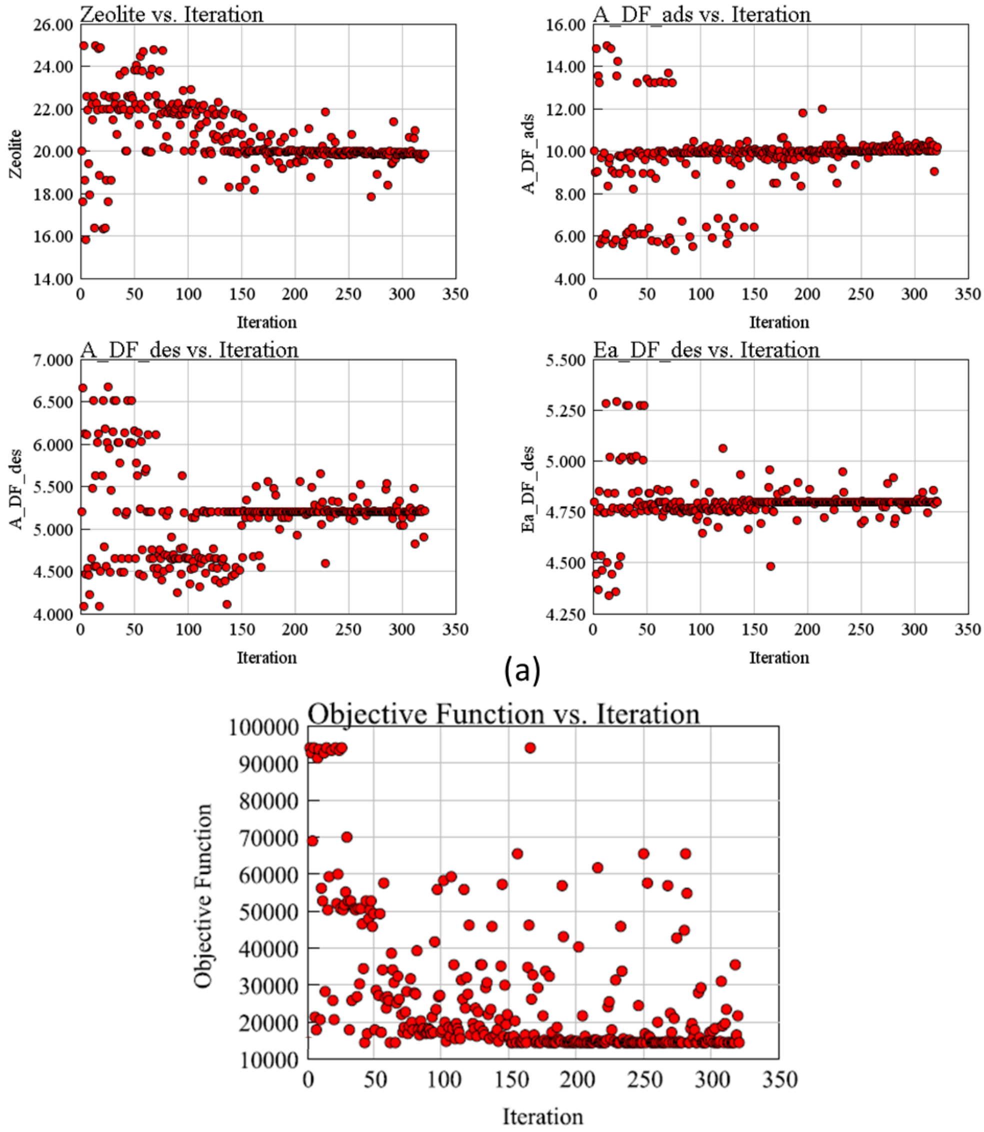

(a)

(b)

Figure 67. An example of GA optimization tool application for calibration of DOC kinetic parameters for the front core; a) independent variables as a function of iterations; b) progress of objective function

2. Using test#14 and #15 from light-off experiments, Table 38, which only includes decane in the inlet batch, gives the possibility to calibrate $C_{10}H_{22}$ oxidation parameters, A_5, E_5 in addition to PGM site density. The objective function is defined according to Equation 61., using 16 population, 20 generations and a mutation rate of 0.3. As an example, a comparison between simulated, optimization results, and measured decane concentrations are shown in Figure 68 for the front core and the rear core for selected tests. It can be observed that the results of the front core,

Figure 68-a, shows trapping of decane at lower temperatures due to presence of zeolite coating; however, in the rear core, Figure 68-b, the effect of zeolite HC trapping is not detected.

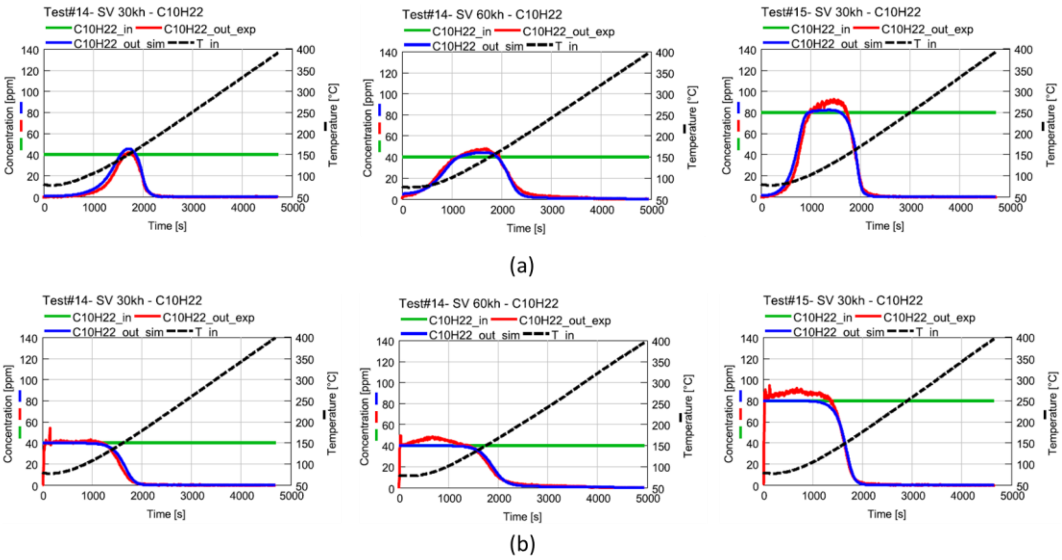

(a)

(b)

Figure 68. Simulated and measured concentrations of $C_{10}H_{22}$ after calibration of $C_{10}H_{22}$ oxidation kinetic constants; a) front core; b) rear core

3. Test#01, #02 are used for calibration of CO oxidation parameters (A_3, E_3) in addition to the CO inhibition term. 16 population size and 25 generations was selected with the aim to minimize the objective function is defined by Equation 62:

$$F_{obj} = \int_{0}^{t_{end}} |(C_{CO})_{sim} - (C_{CO})_{meas}| dt \tag{62}$$

4. Calibration of C_3H_6 oxidation parameters (A_4, E_4) and propylene inhibition term parameters, using experimental data of test #09 and #10 with 20 population size, 25 generations and 0.2 mutation rate. The objective function is defined by Equation 63: As an example, a comparison between optimization results and measured propylene concentrations are shown in Figure 69 for the front core and the rear core for selected tests.

$$F_{obj} = \int_{0}^{t_{end}} \left|(C_{C_3H_6})_{sim} - (C_{C_3H_6})_{meas}\right| dt \tag{63}$$

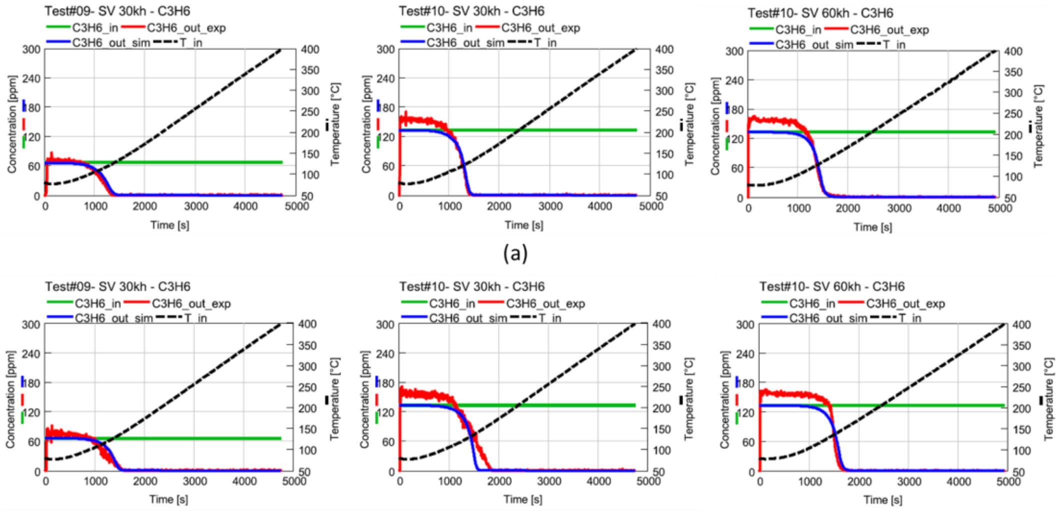

(a)

(b)

Figure 69. Simulated and measured concentrations of C_3H_6 after calibration of C_3H_6 oxidation kinetic constants; a) front core; b) rear core

5. Calibration of NO oxidation parameters (A_6, E_6) and inhibition term, using experimental data of test #19 and #20 with 20 population size, 25 generations and 0.2 mutation rate. The objective function is defined by Equation 64: As an example, a comparison between simulated, optimization results, and measured NO and NO_2 concentrations are shown in Figure 70 and Figure 71 , respectively, for the front core and the rear core for selected tests; showing acceptable matching between simulated with measured traces.

$$F_{obj} = \int_{0}^{t_{end}} \left(\left| (C_{NO})_{sim} - (C_{NO})_{meas} \right| + \left| (C_{NO_2})_{sim} - (C_{NO_2})_{meas} \right| \right) dt \tag{64}$$

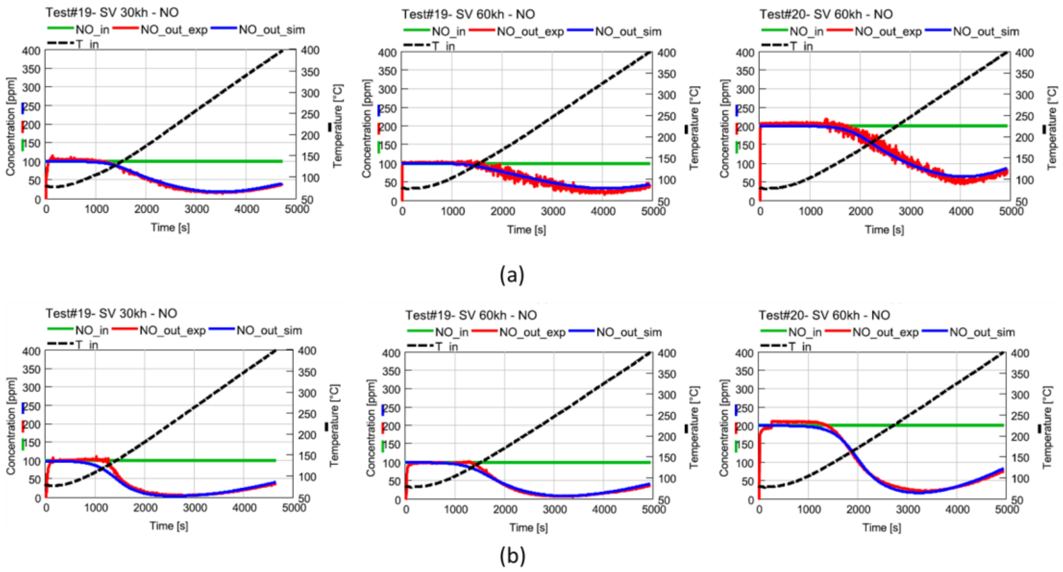

(a)

(b)

Figure 70. Simulated and measured concentrations of NO after calibration of NO oxidation kinetic constants; a) front core; b) rear core

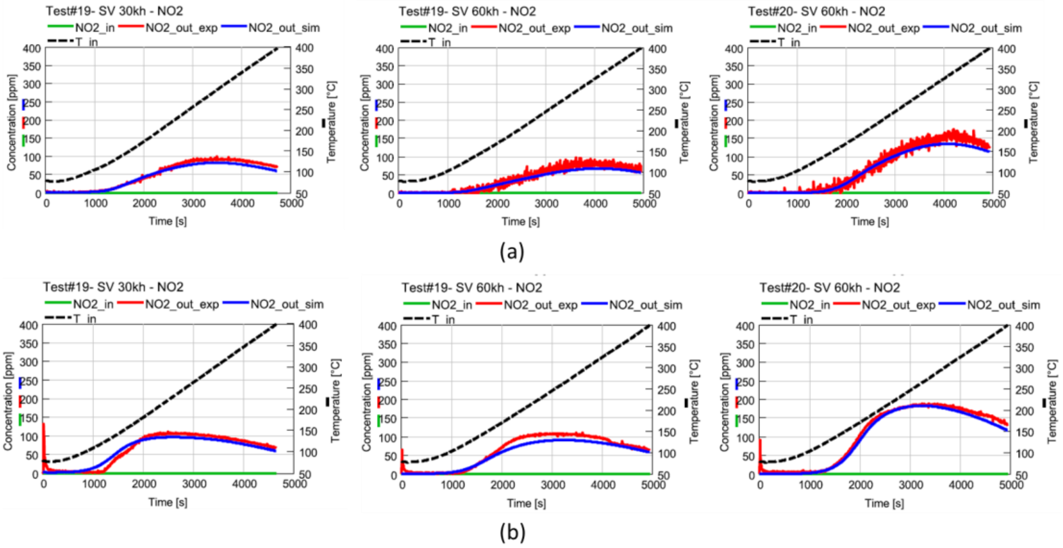

(a)

(b)

Figure 71. Simulated and measured concentrations of NO_2 after calibration of NO oxidation kinetic constants; a) front core; b) rear core

After calibration of pre-exponent multipliers and activation energies of oxidation reactions and inhibitions terms using single species experiments, the tests with more than 1 trace species present in the inlet batch can be used to determine the exponents of inhibition terms.

6. Therefore, test #04 which includes CO and $C_{10}H_{22}$ in the inlet batch is used for the calibration of CO inhibition effect on decane oxidation reaction, with 16 population size, 10 generations and 1 mutation rate. The objective function is defined by Equation 61.

7. The interaction between NO and CO can be characterized using test#06 and test#07 experimental data, giving the possibility to optimize NO inhibition exponent effect on CO oxidation in addition to A_9 and E_9 (reaction#9 parameters of in Table 39 and Table 40. The objective function is defined as weighted error between simulated and measured traces of NO, NO_2 and CO, Equation 65, and optimization settings include 16 population size, 20 generations and 0.333 mutation rate.

$$F_{obj} = \int_0^{t_{end}} \big(w_1 |(C_{NO})_{sim} - (C_{NO})_{meas}| + w_2 \left|(C_{NO_2})_{sim} - (C_{NO_2})_{meas}\right| + w_3 |(C_{CO})_{sim} - (C_{CO})_{meas}|\big) dt \tag{65}$$

8. The interaction between CO and C_3H_6 is characterized using test #03 and the inhibition terms are calibrated using objective function defined in Equation 66. Optimization settings include 16 population size, 20 generations and 0.5 mutation rate.

$$\mathrm{F_{obj}} = \int_0^{\mathrm{t_{end}}} \big(\mathrm{w_1} \left|(\mathrm{C_{C_3H_6}})_{\mathrm{sim}} - (\mathrm{C_{C_3H_6}})_{\mathrm{meas}}\right| + \mathrm{w_2} |(\mathrm{C_{CO}})_{\mathrm{sim}} - (\mathrm{C_{CO}})_{\mathrm{meas}}|\big) \mathrm{dt} \tag{66}$$

9. Test #05, including CO, C_3H_6 and $C_{10}H_{22}$ is used, is used to characterize propylene inhibition effect on decane oxidation with the aim to minimize objective function defined in Equation 61 and optimization settings defined in step 6.

The last two steps include characterization of interaction between HCs and NO_x and N_2O production.

10. Test #16 and #17, including NO and decane in the inlet, are used to obtain the kinetic parameters of A_8, E_8, A_{11}, E_{11} listed in Table 39 and Table 40. The optimization settings contain 80 population size, 30 generations and a mutation rate of 0.111 with the aim of minimizing the objective function defined in Equation 67.

$$
\begin{aligned}
F_{obj} = \int_{0}^{t_{end}} \Big(& w_1 |(C_{NO})_{sim} - (C_{NO})_{meas}| \\
& + w_2 \big|(C_{NO_2})_{sim} - (C_{NO_2})_{meas}\big| \\
& + w_3 \big|(C_{N_2O})_{sim} - (C_{N_2O})_{meas}\big| \\
& + w_4 \big|(C_{C_{10}H_{22}})_{sim} - (C_{C_{10}H_{22}})_{meas}\big| \Big) dt
\end{aligned}
\tag{67}
$$

11. Test #11 and #12, including NO and propylene in the inlet, are used to obtain the kinetic parameters of A_7, E_7, A_{10}, E_{10} in addition to corresponding inhibition term parameters (I_{10}) listed in Table 39 and Table 40. The optimization settings contain 80 population size, 30 generations and a mutation rate of 0.111 with the aim of minimizing the objective function defined in Equation 68.

$$
\begin{aligned}
F_{obj} = \int_{0}^{t_{end}} \Big(& w_1 |(C_{NO})_{sim} - (C_{NO})_{meas}| \\
& + w_2 \big|(C_{NO_2})_{sim} - (C_{NO_2})_{meas}\big| \\
& + w_3 \big|(C_{N_2O})_{sim} - (C_{N_2O})_{meas}\big| \\
& + w_4 \big|(C_{C_3H_6})_{sim} - (C_{C_3H_6})_{meas}\big| \Big) dt
\end{aligned}
\tag{68}
$$

The list of calibration parameters including the range of variation and the optimized values are reported in Table 41. It should be noted the pre-exponent multipliers and activation energies are represented in the form of $10^{[A]}$ and $10^{[Ea]}$ in order to cover higher range in the calibration process. In addition, the optimized value for the site densities are reported in Table 42.

Table 41. Optimized values and range of pre-exponent multipliers and activation energies of the reactions for the DOC kinetic model

Reaction	**Pre-exponent Multiplier** $10^{[A]}$			**Activation Energy**$10^{[Ea]}$		
	Range	**Front**	**Rear**	**Range**	**Front**	**Rear**
1	-2 – 1.5	1.009	-	-	-	-
2	2 – 8	5.210	-	4 – 6	4.800	
3	13 – 17	14.523	14.814	2 – 8	4.993	4.993
4	14.5 – 19.5	17.709	16.902	13 – 17	5.096	5.075
5	15.5 – 19.5	17.156	17.539	4 – 6	5.135	5.135

6	2 – 6	4.339	5.556	3 – 5	4.469	4.533
7	11 – 18	11.675	13.726	3 – 6.5	4.645	4.841
8	12 – 20	15.063	16.706	3.5 – 6.5	4.950	5.010
9	7 – 11	7.143	8.217	3 – 5	3.214	3.786
10	12 – 24	17.437	17.888	3.5 – 6.5	5.074	5.076
11	12 – 24	23.556	22.940	3.5 – 6.5	5.185	5.140

Table 42. Optimized values and range of site densities for the DOC kinetic mod

Parameter	**Range**	**Front**	**Rear**
Zeolite Site Density	10 – 30	19.844	-
PGM Dispersion Factor	0.3 – 1.1	0.656	0.518

In the following part, the optimized calibrated parameters are inserted in the DOC kinetic scheme for the validation of the model using the experimental data with more complex gas mixture at the inlet.

As an example, test #08, #22 and #23, in which the inlet batch composition includes all the trace species as reported in Table 38, are selected for validation. Temperature profiles during the tests are depicted in Figure 72, for the front and the rear core samples. It can be observed that the assumption of isothermal condition can be confirmed and temperature drop due to heat transfer is not detected from measurements. Slight increase in temperature across the DOC is seen comparing the inlet and outlet temperatures which is due to the exotherm effect of oxidation reactions. Moreover, it is worth noting that the model predictions are in good agreement compared to measured values.

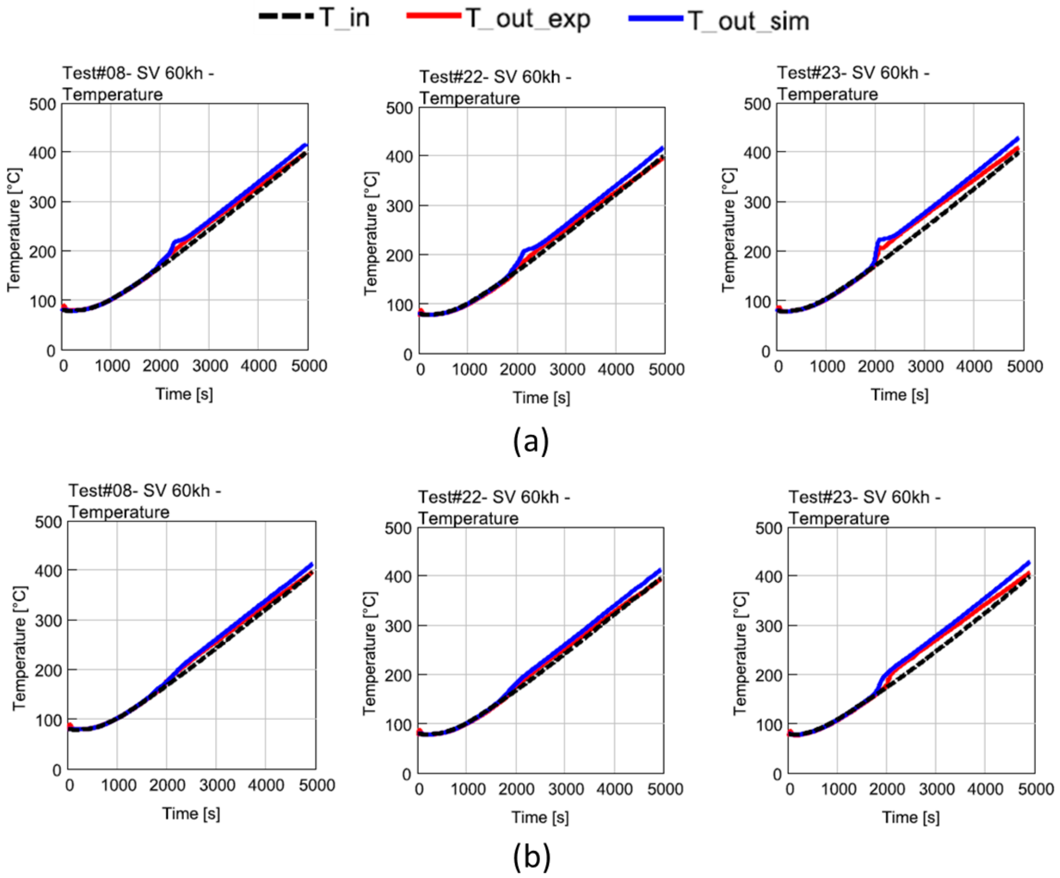

(a)

(b)

Figure 72. Temperature profiles across DOC; a) front core; b) rear core

The results of the CO, C_3H_6 and $C_{10}H_{22}$ traces are shown in Figure 73 and Figure 74 for the front and the rear cores, respectively. It can be observed that the model predictions are in agreement with measured data for CO and HCs regarding light-off, while for the model over-estimates the light-off for decane in the front core data, Figure 73-c. It is worth mentioning that inlet conditions are assumed to be equal to nominal values in the model, since measurements were not performed at the inlet of DOC and therefore slight variations, such as higher concentration of propylene before light-off for test #23, Figure 73-b and Figure 74-b, are acceptable considering that real dosing might differ from nominal condition. In addition, it can be observed that the front core decane adsorption, thanks to zeolite coating, is well-captured by the model. It can also be confirmed that HC trapping is only applied to long chain HC, $C_{10}H_{22}$, and the measurements do not suggest C_3H_6 trapping which was also not included in the model.

In addition focusing on CO concentrations of the front core sample, Figure 73-a, and $C_{10}H_{22}$, Figure 73-c, concentrations, as previously mentioned, it can be confirmed that steam reforming and water gas shift do not play significant role in the lean condition where excess of O_2 is present and therefore for model simplifications SR and WGS can be disregarded from kinetic scheme calibration.

The NO, NO_2, NO_x and N_2O traces are shown in Figure 75 and Figure 76 for the front core and the rear core samples, respectively, using inlet condition specified by test #08, #22 and #23. Test #08, includes NO_2 in the inlet batch and it can be observed that at lower temperatures, before CO light-off, reaction #09 in Table 39 results in production of NO; however, after CO light-off is reached the rate of reaction of CO oxidation overcomes reaction #09 and CO will be oxidized. Referring to NO concentration, Figure 75-a, it can be observed that by increasing temperature NO oxidation leads to higher amount of NO_2 production.

Moreover, due to differences is PGM loading and formulation, Pd/Pt ratio, between the rear and the front core, NO oxidation rate and NO_2 production is different [118]. This behavior can be observed comparing NO traces at the outlet of DOC of the front and the rear cores, Figure 75-a and Figure 76-a, respectively.

As expected, NO_x concentration is constant and equal to the inlet during the test, Figure 75-c and Figure 76-c, except during N_2O production, Figure 75-d and Figure 76-d, which depends on HC and NO concentrations in addition to temperature; thus, a maximum in N_2O production coincident with a minimum in NO_x traces is detected. Considering that front core limits decane concentration due to adsorption, lower amount of N_2O is produced, Figure 75-d, with respect to the rear core in which higher amount of decane is available, Figure 76-d.

In summary, the model predictions for both cores are in satisfactory agreement with measured data and the provided calibration guideline and automatic optimization tool can be successfully implemented for finding kinetic parameters of a DOC model.

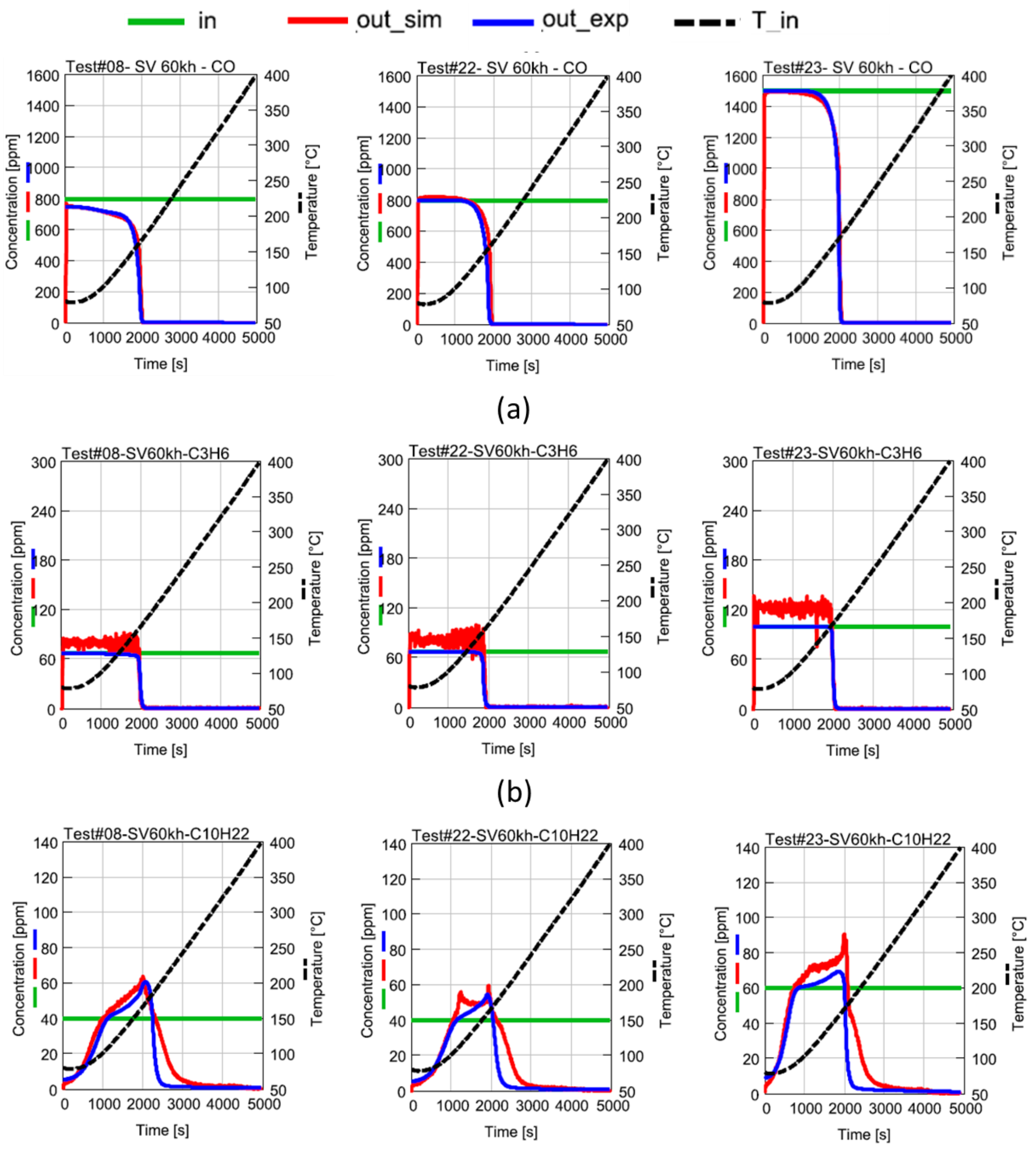

(a)

(b)

(c)

Figure 73. Results of validation of the DOC kinetic model at standard space velocity of 60,000 1/hr for the front core, concentration of trace species; a) CO; b) C_3H_6; c) $C_{10}H_{22}$

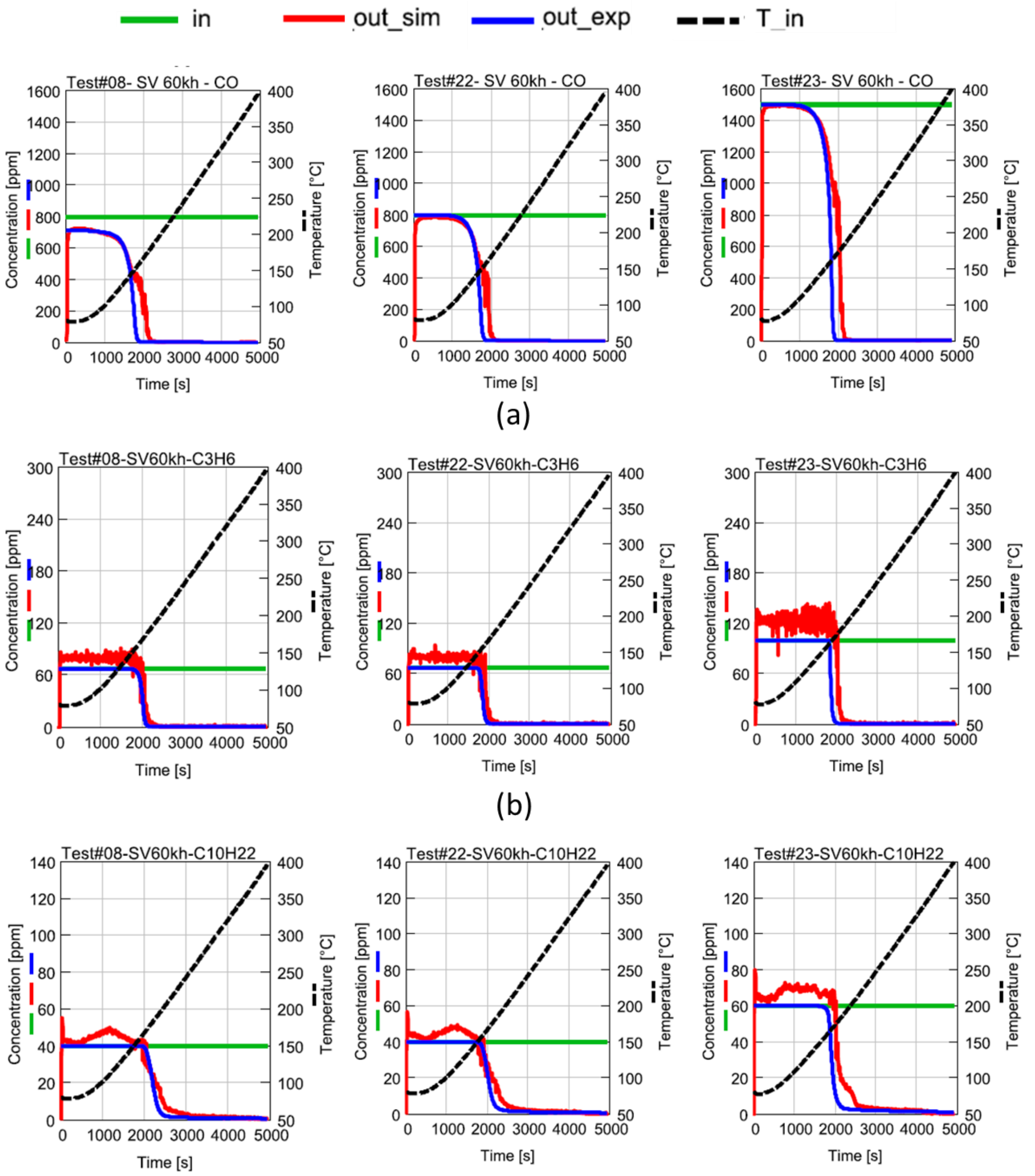

(a)

(b)

(c)

Figure 74. Results of validation of the DOC kinetic model at standard space velocity of 60,000 1/hr for the rear core, concentration of trace species; a) CO; b) C_3H_6; c) $C_{10}H_{22}$

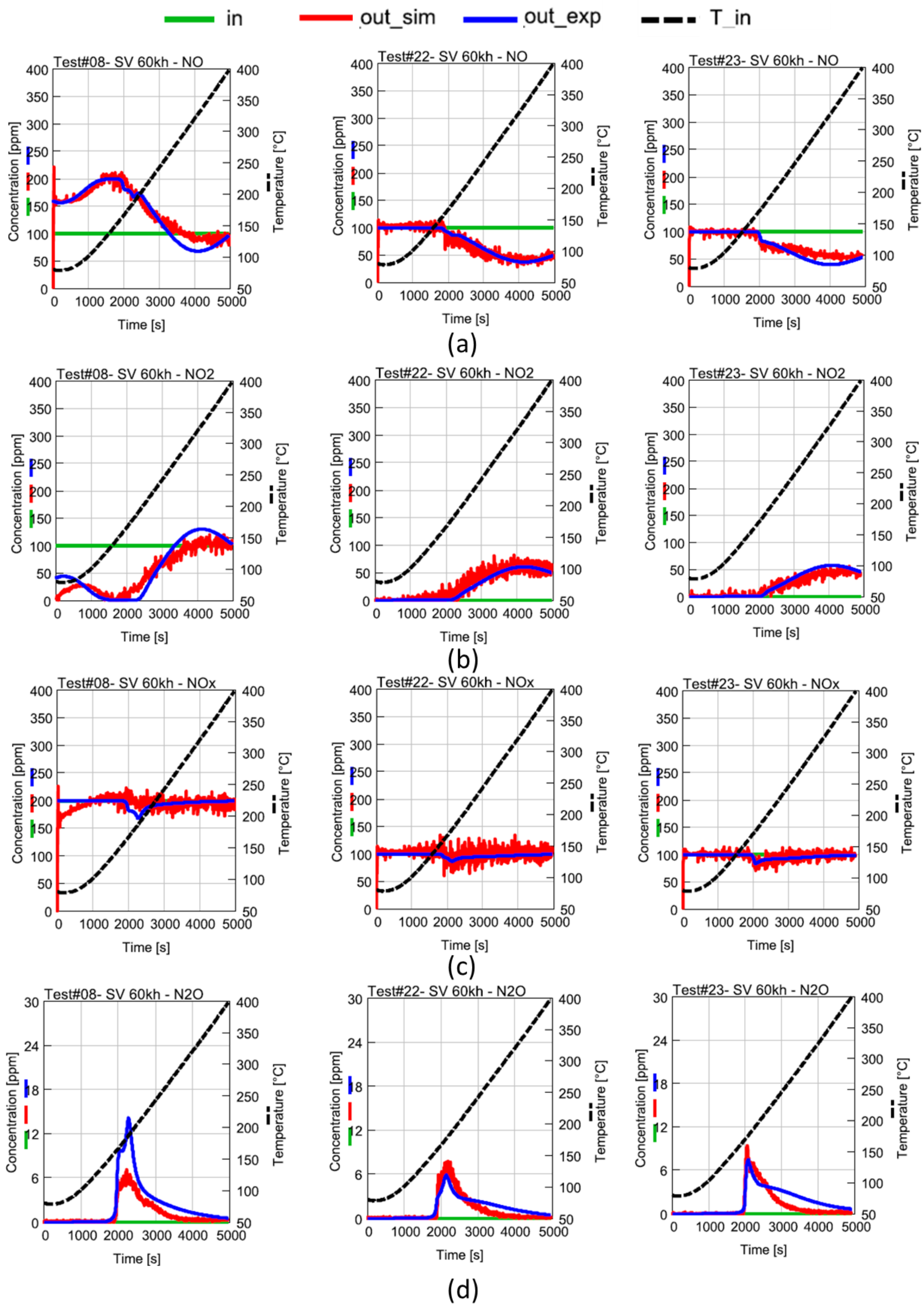

Figure 75. Results of validation of the DOC kinetic model at standard space velocity of 60,000 1/hr for the front core, concentration of trace species; a) NO; b) NO_2; c) NO_x; d) N_2O

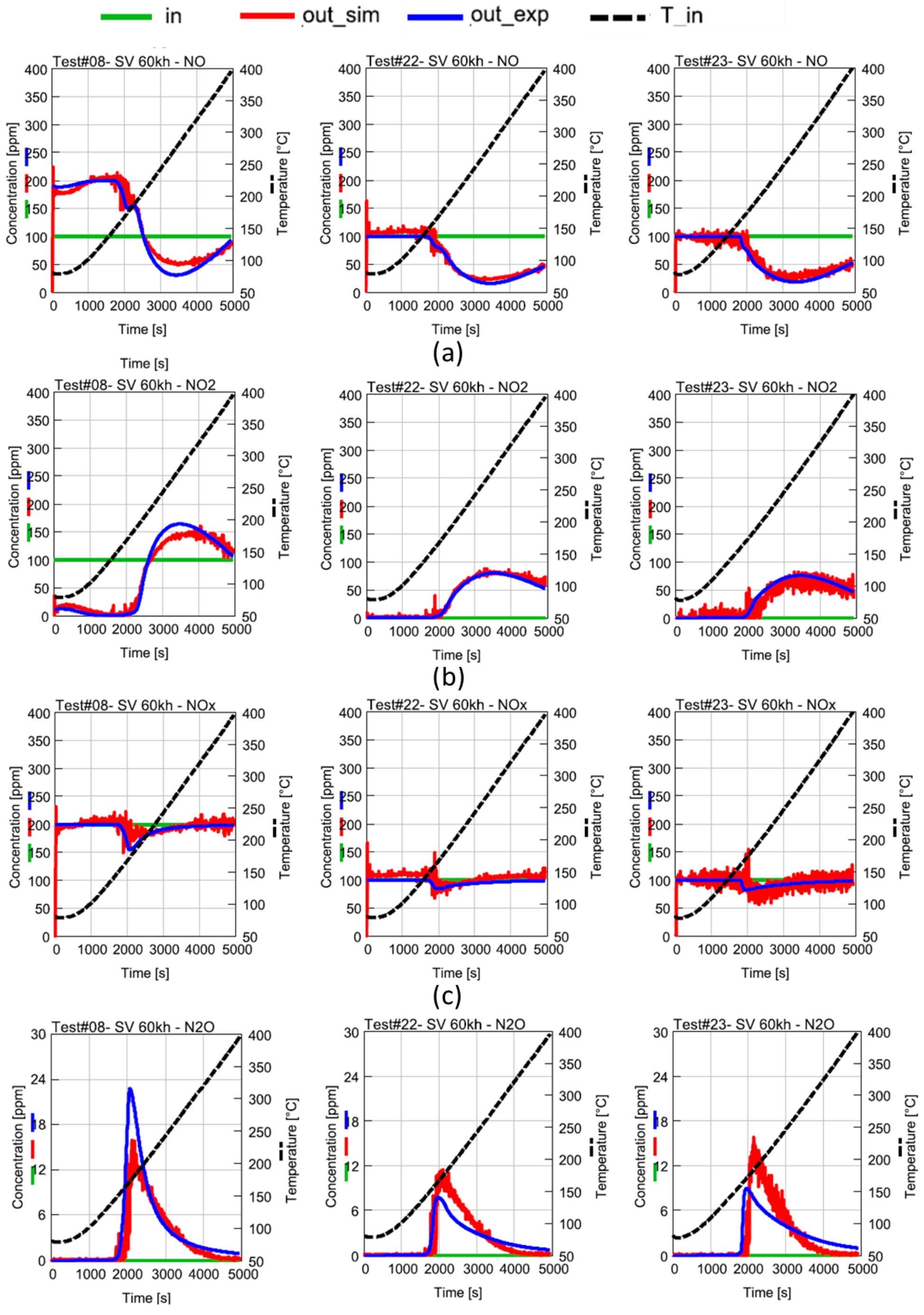

(a)

(b)

(c)

(d)

Figure 76. Results of validation of the DOC kinetic model at standard space velocity of 60,000 1/hr for the rear core, concentration of trace species; a) NO; b) NO_2; c) NO_x; d) N_2O

In conclusion, it can realized that the application of GA optimization tool in calibration of a kinetic model for aftertreatment systems can successfully predict the behavior of the system compared with measured data assuring that the objective fuction, in this case the error between simulation and measurement, will not trap in local minimum and that a deep knowledge of kinetics will not be required due to not dependency of the optimization results to the starting point. Therefore, through definition of a step-by-step guideline, as presented in this Chapter, the modeler can take advantage of more automatic approaches with higher level of accuracy and less effort instead of traditional methods such as manual calibration or optimization tools which depend on initial guess.

Chapter 7

Conclusions

Controlling emissions of a lean exhaust requires a combination of system of aftertreatment technologies such as Diesel Oxidation Catalyst (DOC) to reduce hydrocarbon (HC) and CO emissions, Lean NO_x Trap (LNT) to reduce NO_x, CO and HC emissions, Selective Catalytic Reduction (SCR) for NO_x control and Diesel Particulate Filter (DPF) for PM emissions. Reliable and computationally efficient simulation models can support the optimization of such complex systems thanks to their reduced time and cost expenses. Therefore, the innovative contribution expected from this research was the assessment, through a new comprehensive numerical model of the whole powertrain system, including the aftertreatment, of the more promising technology mix to reach the future challenging emissions and fuel economy targets for diesel powertrain for passenger car applications.

In the current work the performance of 3 different aftertreatment components including Diesel Oxidation Catalyst (DOC), Lean NO_x Trap (LNT) and Selective Catalytic Reduction coated on Filter (SCR-F) is analyzed both experimentally and numerically. The experimental activity for the three mentioned components are performed, separately, by defining suitable test protocols on Synthetic Gas Bench (SGB) using controlled species concentrations, temperature and mass flowrates with the aim to register sufficient information for the calibration of simulation model. Afterwards, the simulation model for each technology is built using a commercially available software, 1D GT-SUITE, and a proper global kinetic model is calibrated through suitable optimization tool.

Furthermore, the SCR-F model was calibrated using Brent method optimization according to Temperature Programmed Desorption (TPD), Temperature Programmed Reduction (TPR) and NO oxidation tests for different levels of soot loading of a Cu-Zeolite reactor-scale sample. The model successfully captured the effect of NO_2/NO_x ratio and temperature on soot regeneration due to passive regeneration, ammonia storage capacity and NO_x reduction.

In addition, a Lean NO_x Trap kinetic model was developed based on two experimental dataset case studies with the aim of characterizing Oxygen Storage Capacity (OSC), light-off and NO_x Storage and Reduction (NSR) for reactor-scale cordierite samples. A three-site model for NO_x storage and reduction on barium site was proposed and according to sequence of NO, NO_2 and by-products such as N_2O and NH_3 formation during rich phase of NSR, it was found out that NH_3 acts as a secondary reductant for further NO_x reduction. Moreover, the effect of different reductants such as CO, H_2 and HC on NO_x reduction and by-products formation were assessed at different temperature levels. The simulated results showed satisfactory agreement with measured data. Considering that the LNT kinetic scheme is complex and it is required to find suitable set of reactions to mimic measurement traces, manual calibration was applied in most cases.

Afterwards, the LNT model calibrated for reactor-scale component was up-scaled and the engine-out emissions, mass flowrate and temperature over WLTC driving cycle was used as the input in full-size model for validation and assessment of the performance of the whole aftertreatment system to reduce NO_x efficiently. It is worth mentioning that kinetic parameters previously calibrated were kept constant and only reasonable adjustments were applied to consider the effect of geometry; therefore, confirming that the full-size component can differ in terms of external heat loss, uniformity of temperature across a defined cross section, ageing and species concentrations (such as HC speciation). It was shown that the model predictions were in agreement with measurements with a maximum error of 6% in terms of total cumulative NO_x mass along the cycle; thus, confirming the reliability of the model.

After the validation of the LNT model, the model was further reduced and linearized with reasonable assumptions to be converted in fast running plant model for control and real time applications such Electronic Control Unit (ECU)/Hardware-in-the-Loop (HiL) systems using block-in-series approach. The computational run-time of the model was around one fifth of real time using a PC processor with acceptable accuracy.

Finally, the application of Genetic Algorithm for calibration of kinetic model of aftertreatment models was assessed for a zone-coated DOC using SGB experimental data and the model was validated for different complex gas mixtures.

In conclusion, it has been proved that reactor-scale measurements performed through suitable test protocols can assist the calibration of kinetic parameters of a simulation model which can be further validated for full-size sample using engine-out emissions as the input. Moreover, the models can be further combined to simulate the whole aftertreatment system, including DOC+SCR-F or LNT+SCR-F, with the aim to assess the performance of the system over driving cycles.

References

[1] W.A. Majewski, M.K. Khair, Diesel Emissions and Their Control, SAE International, 2006.

[2] L.L.F. Squaiella, C.A. Martins, P.T. Lacava, Strategies for emission control in diesel engine to meet Euro VI, Fuel. 104 (2013) 183–193. doi:10.1016/j.fuel.2012.07.027.

[3] F. Millo, M. Rafigh, Modelling of Aftertreatment Systems for NOx Control for Diesel Passenger Car Applications, in: 5th Int. Exhaust Emiss. Symp., Bosmal, Poland, 2016.

[4] W.A. Majewski, J.L. Ambs, K. Bickel, Nitrogen Oxides Reactions in Diesel Oxidation Catalyst, in: SAE Tech. Pap., SAE International, 1995. doi:10.4271/950374.

[5] F. Millo, M. Rafigh, D. Fino, P. Miceli, Application of a global kinetic model on an SCR coated on Filter (SCR-F) catalyst for automotive applications, Fuel. (2016). doi:10.1016/j.fuel.2016.11.082.

[6] C.S. Sampara, E.J. Bissett, D. Assanis, Hydrocarbon storage modeling for diesel oxidation catalysts, Chem. Eng. Sci. 63 (2008) 5179–5192. doi:10.1016/j.ces.2008.06.021.

[7] K.F. Czaplewski, T.L. Reitz, Y.J. Kim, R.Q. Snurr, One-dimensional zeolites as hydrocarbon traps, Microporous Mesoporous Mater. 56 (2002) 55–64. doi:10.1016/S1387-1811(02)00441-9.

[8] F. Millo, M. Rafigh, M. Andreata, T. Vlachos, P. Arya, P. Miceli, Impact of high sulfur fuel and de-sulfation process on a close-coupled diesel oxidation catalyst and diesel particulate filter, Fuel. (2017) 1–10. doi:10.1016/j.fuel.2017.01.006.

[9] V. Bermúdez, J.M. Luján, P. Piqueras, D. Campos, Pollutants emission and particle behavior in a pre-turbo aftertreatment light-duty diesel engine, Energy. 66 (2014) 509–522. doi:10.1016/j.energy.2014.02.004.

[10] a Konstandopoulos, D. Zarvalis, I. Dolios, Multi-Instrumental Assessment

of Diesel Particulate Filters, SAE Tech. Pap. 2007 (2007) 776–790. doi:10.4271/2007-01-0313.

[11] F. Millo, M. Andreata, M. Rafigh, D. Mercuri, C. Pozzi, Impact on vehicle fuel economy of the soot loading on diesel particulate filters made of different substrate materials, Energy. 86 (2015) 19–30. doi:10.1016/j.energy.2015.03.076.

[12] M. Koebel, M. Elsener, M. Kleemann, Urea-SCR: a promising technique to reduce NOx emissions from automotive diesel engines, Catal. Today. 59 (2000) 335–345. doi:10.1016/S0920-5861(00)00299-6.

[13] T. Wittka, B. Holderbaum, P. Dittmann, S. Pischinger, Experimental Investigation of Combined LNT + SCR Diesel Exhaust Aftertreatment, Emiss. Control Sci. Technol. 1 (2015) 167–182. doi:10.1007/s40825-015-0012-0.

[14] R.G. Tonkyn, R.S. Disselkamp, C.H.F. Peden, Nitrogen release from a NOx storage and reduction catalyst, Catal. Today. 114 (2006) 94–101. doi:10.1016/j.cattod.2006.02.005.

[15] F. Millo, M. Rafigh, S. Wahiduzzaman, R. Dudgeon, Calibration of a Global Kinetic Mechanism Based on Synthetic Gas Bench Experiments for a Lean NOx Trap Catalyst for Automotive Applications, THIESEL Conf. Thermo-Fluid Dyn. Process. Direct Inject. Engines. (2016).

[16] M. Rafigh, R. Dudgeon, J. Pihl, S. Daw, R. Blint, S. Wahiduzzaman, Development of a Global Kinetic Model for a Commercial Lean NOx Trap Automotive Catalyst Based on Laboratory Measurements, Emiss. Control Sci. Technol. (2016). doi:10.1007/s40825-016-0049-8.

[17] T. Wittka, B. Holderbaum, T. Maunula, M. Weissner, Development and Demonstration of LNT+SCR System for Passenger Car Diesel Applications, SAE Int. J. Engines. 7 (2014) 1269–1279. doi:10.4271/2014-01-1537.

[18] T. Körfer, Potential of Advanced, Combined Aftertreatment Systems for Light-Duty Diesel Engines to Meet Upcoming EU and US Emission Regulation, in: SAE Tech. Pap., SAE International, 2013. doi:10.4271/2013-24-0163.

[19] K. Ruth, I. Grisstede, W. Müller, S. Franoschek, M. Seyler, R. Hoyer, H. Noack, S. Basso, Diesel NOx -After-treatment Systems for Upcoming LDV-Emission Legislations, Umicore AG Co. KG, Hanau-Wolfgang, Ger. (2012).

[20] R. Wanker, H. Granter, G. Bachler, G. Rabenstein, A. Ennemoser, R.

Tatschl, M. Bollig, New physical and chemical models for the CFD simulation of exhaust gas lines: A generic approach, SAE Tech. Pap. (2002). doi:10.4271/2002-01-0066.

[21] J.C. Wurzenberger, R. Wanker, Multi-Scale SCR Modeling, 1D Kinetic Analysis and 3D System Simulation, SAE Tech. Pap. (2005). doi:10.4271/2005-01-0948.

[22] D. Chatterjee, P. Kočí, V. Schmeißer, M. Marek, M. Weibel, B. Krutzsch, Modelling of a combined NOx storage and NH3-SCR catalytic system for Diesel exhaust gas aftertreatment, in: Catal. Today, 2010: pp. 395–409. doi:10.1016/j.cattod.2010.01.014.

[23] M. Corbetta, F. Manenti, C.G. Visconti, S. Pierucci, L. Lietti, P. Forzatti, Development of a kinetic model of lean-nox-trap and validation through a reactive CFD approach, Chem. Eng. Trans. 32 (2013) 643–648. doi:10.3303/CET1332108.

[24] C. Ong, A. Annaswamy, I. V. Kolmanovsky, P. Laing, D. Reed, An Adaptive Proportional Integral Control of a Urea Selective Catalytic Reduction System based on System Identification Models, SAE Int. J. Fuels Lubr. 3 (2010) 625–642. doi:10.4271/2010-01-1174.

[25] W. Tang, S. Wahiduzzaman, S. Wenzel, A. Leonard, T. Morel, Development of a Quasi-Steady Approach Based Simulation Tool for System Level Exhaust Aftertreatment Modeling, Sae Tech. Pap. Ser. 2008 (2008) 776–790. doi:10.4271/2008-01-0866.

[26] A. Onorati, G. Ferrari, G. D’Errico, G. Montenegro, The prediction of 1D unsteady flows in the exhaust system of a S.I. Engine including chemical reactions in the gas and solid phase, SAE Tech. Pap. (2002). doi:10.4271/2002-01-0003.

[27] C. Depcik, D. Assanis, One-dimensional automotive catalyst modeling, Prog. Energy Combust. Sci. 31 (2005) 308–369. doi:10.1016/j.pecs.2005.08.001.

[28] G. Mauviot, F. le Berr, S. Raux, F. Perretti, L.M. Malbec, C.N. Millet, 0D Modelling: A promising means for after-treatment issues in modern automotive applications, La Simul. 0D Une Voie D’avenir Pour Trait. Les Problématiques Post-Traitement Des Véhicules Automob. Mod. 64 (2009) 285–307. doi:10.2516/ogst/2009023.

[29] S.R. Gundlapally, I. Papadimitriou, S. Wahiduzzaman, T. Gu, Development of ECU Capable Grey-Box Models from Detailed Models—Application to a

SCR Reactor, Emiss. Control Sci. Technol. 2 (2016) 124–136. doi:10.1007/s40825-016-0039-x.

[30] S.R. Gundlapally, V. Balakotaiah, Heat and mass transfer correlations and bifurcation analysis of catalytic monoliths with developing flows, Chem. Eng. Sci. 66 (2011) 1879–1892. doi:10.1016/j.ces.2011.01.045.

[31] Gamma Technologies LLC, GT-SUITE Aftertreatment Manual, 2015.

[32] M. Mirzaeian, F. Millo, L. Rolando, Assessment of the Predictive Capabilities of a Combustion Model for a Modern Downsized Turbocharged SI Engine, in: SAE Tech. Pap., SAE International, 2016. doi:10.4271/2016-01-0557.

[33] A. Piano, F. Millo, G. Boccardo, M. Rafigh, A. Gallone, M. Rimondi, Assessment of the Predictive Capabilities of a Combustion Model for a Modern Common Rail Automotive Diesel Engine, SAE Tech. Pap. 2016–April (2016). doi:10.4271/2016-01-0547.

[34] C.S. Sampara, E.J. Bissett, M. Chmielewski, Global kinetics for a commercial diesel oxidation catalyst with two exhaust hydrocarbons, Ind. Eng. Chem. Res. 47 (2008) 311–322. doi:10.1021/ie070813x.

[35] T.J. Wang, S.W. Baek, J.H. Lee, Kinetic parameter estimation of a diesel oxidation catalyst under actual vehicle operating conditions, Ind. Eng. Chem. Res. 47 (2008) 2528–2537. doi:10.1021/ie071306i.

[36] I. Nova, C. Ciardelli, E. Tronconi, D. Chatterjee, M. Weibel, NH3-NO/NO2 SCR for diesel exhausts after treatment: Mechanism and modelling of a catalytic converter, Top. Catal. 42–43 (2007) 43–46. doi:10.1007/s11244-007-0148-4.

[37] C. Ciardelli, I. Nova, E. Tronconi, D. Chatterjee, B. Bandl-Konrad, M. Weibel, B. Krutzsch, Reactivity of NO/NO2-NH3 SCR system for diesel exhaust aftertreatment: Identification of the reaction network as a function of temperature and NO2 feed content, Appl. Catal. B Environ. 70 (2007) 80–90. doi:10.1016/j.apcatb.2005.10.041.

[38] C. Lee, Modeling urea-selective catalyst reduction with vanadium catalyst based on NH3 temperature programming desorption experiment, Fuel. 173 (2016) 155–163. doi:10.1016/j.fuel.2016.01.065.

[39] M. Schejbal, J. Štěpánek, M. Marek, P. Kočí, M. Kubíček, Modelling of soot oxidation by NO2 in various types of diesel particulate filters, Fuel. 89 (2010) 2365–2375. doi:10.1016/j.fuel.2010.04.018.

[40] T.C. Watling, M.R. Ravenscroft, G. Avery, Development, validation and application of a model for an SCR catalyst coated diesel particulate filter, Catal. Today. 188 (2012) 32–41. doi:10.1016/j.cattod.2012.02.007.

[41] J. Czerwinski, Y. Zimmerli, A. Mayer, J. Lemaire, D. Zürcher, G. D'Urbano, Investigations of SDPF -Diesel Particle Filter with SCR Coating for HD-Applications, in: SAE Tech. Pap., SAE International, 2015. doi:10.4271/2015-01-1023.

[42] F. Schrade, M. Brammer, J. Schaeffner, K. Langeheinecke, L. Kraemer, Physico-chemical modeling of an integrated SCR on DPF (SCR/DPF) system, SAE Int. J. Engines. 5 (2012) 958–974. doi:10.4271/2012-01-1083.

[43] M. Colombo, G. Koltsakis, I. Koutoufaris, A Modeling Study of Soot and De-NOx Reaction Phenomena in SCRF Systems, in: SAE Tech. Pap., SAE International, 2011. doi:10.4271/2011-37-0031.

[44] J.Y. Kim, G. Cavataio, J.E. Patterson, P.M. Laing, C.K. Lambert, Laboratory Studies and Mathematical Modeling of Urea SCR Catalyst Performance, in: SAE Tech. Pap., SAE International, 2007. doi:10.4271/2007-01-1573.

[45] A. Grossale, I. Nova, E. Tronconi, Study of a Fe-zeolite-based system as NH3-SCR catalyst for diesel exhaust aftertreatment, Catal. Today. 136 (2008) 18–27. doi:10.1016/j.cattod.2007.10.117.

[46] O. Kröcher, M. Devadas, M. Elsener, A. Wokaun, N. Söger, M. Pfeifer, Y. Demel, L. Mussmann, Investigation of the selective catalytic reduction of NO by NH3 on Fe-ZSM5 monolith catalysts, Appl. Catal. B Environ. 66 (2006) 208–216. doi:10.1016/j.apcatb.2006.03.012.

[47] M. Koebel, G. Madia, M. Elsener, Selective catalytic reduction of NO and NO2 at low temperatures, Catal. Today. 73 (2002) 239–247. doi:10.1016/S0920-5861(02)00006-8.

[48] A. Grossale, I. Nova, E. Tronconi, Role of Nitrate Species in the "NO2-SCR" Mechanism over a Commercial Fe-zeolite Catalyst for SCR Mobile Applications, Catal. Letters. 130 (2009) 525–531. doi:10.1007/s10562-009-9942-x.

[49] M. Naseri, S. Chatterjee, M. Castagnola, H.-Y. Chen, J. Fedeyko, H. Hess, J. Li, Development of SCR on Diesel Particulate Filter System for Heavy Duty Applications, SAE Int. J. Engines. 4 (2011) 1798–1809. doi:10.4271/2011-01-1312.

[50] J. Tan, C. Solbrig, S.J. Schmieg, The Development of Advanced 2-Way

SCR/DPF Systems to Meet Future Heavy-Duty Diesel Emissions, in: SAE Tech. Pap., SAE International, 2011. doi:10.4271/2011-01-1140.

[51] T. Ballinger, J. Cox, M. Konduru, D. De, W. Manning, P. Andersen, Evaluation of SCR Catalyst Technology on Diesel Particulate Filters, SAE Int. J. Fuels Lubr. 2 (2009) 369–374. doi:10.4271/2009-01-0910.

[52] F. Marchitti, I. Nova, E. Tronconi, Experimental study of the interaction between soot combustion and NH3-SCR reactivity over a Cu–Zeolite SDPF catalyst, Catal. Today. 267 (2016) 110–118. doi:http://doi.org/10.1016/j.cattod.2016.01.027.

[53] M. Devadas, O. Kröcher, M. Elsener, A. Wokaun, N. Söger, M. Pfeifer, Y. Demel, L. Mussmann, Influence of NO2 on the selective catalytic reduction of NO with ammonia over Fe-ZSM5, Appl. Catal. B Environ. 67 (2006) 187–196. doi:10.1016/j.apcatb.2006.04.015.

[54] M. Koebel, M. Elsener, G. Madia, Reaction Pathways in the Selective Catalytic Reduction Process with NO and NO2 at Low Temperatures, Ind. Eng. Chem. Res. 59 (2001) 52–59.

[55] E. Tronconi, I. Nova, F. Marchitti, G. Koltsakis, D. Karamitros, B. Maletic, N. Markert, D. Chatterjee, M. Hehle, Interaction of NOx Reduction and Soot Oxidation in a DPF with Cu-Zeolite SCR Coating, Emiss. Control Sci. Technol. 1 (2015) 134–151. doi:10.1007/s40825-015-0014-y.

[56] I. Nova, L. Castoldi, L. Lietti, E. Tronconi, P. Forzatti, F. Prinetto, G. Ghiotti, The Pt-Ba interaction in lean NOx trap systems, SAE Tech. Pap. (2005). doi:10.4271/2005-01-1085.

[57] Z.M. Liu, J.H. Li, S.I. Woo, Recent advances in the selective catalytic reduction of NOx by hydrogen in the presence of oxygen, Energy Environ. Sci. 5 (2012) 8799–8814. doi:10.1039/c2ee22190j.

[58] P. Forzatti, L. Lietti, I. Nova, E. Tronconi, Diesel NOx aftertreatment catalytic technologies: Analogies in LNT and SCR catalytic chemistry, Catal. Today. 151 (2010) 202–211. doi:10.1016/j.cattod.2010.02.025.

[59] C. Daw, K. Chakravarthy, K. Lenox, A simple model for lean NOx adsorber catalysts, Proc. 3rd Jt. Meet. US Sect. Combust. Inst. (2003). doi:papers://B3F20CA2-9ACD-4BA1-A510-19A2EC38FE78/Paper/p613.

[60] J. Xu, M.P. Harold, V. Balakotaiah, Modeling the effects of Pt loading on NOx storage on Pt/BaO/Al2O3 catalysts, Appl. Catal. B Environ. 104 (2011) 305–315. doi:10.1016/j.apcatb.2011.03.014.

[61] S. Morandi, G. Ghiotti, L. Castoldi, L. Lietti, I. Nova, P. Forzatti, Reduction by CO of NO x species stored onto Pt–K/Al 2 O 3 and Pt–Ba/Al 2 O 3 lean NO x traps, Catal. Today. 176 (2010) 399–403. doi:10.1016/j.cattod.2010.11.024.

[62] I. Nova, L. Lietti, P. Forzatti, F. Prinetto, G. Ghiotti, Experimental investigation of the reduction of NOx species by CO and H2 over Pt-Ba/Al2O3 lean NOx trap systems, Catal. Today. 151 (2010) 330–337. doi:10.1016/j.cattod.2010.02.075.

[63] M. AL-Harbi, D. Radtke, W.S. Epling, Regeneration of a model NOX storage/reduction catalyst using hydrocarbons as the reductant, Appl. Catal. B Environ. 96 (2010) 524–532. doi:10.1016/j.apcatb.2010.03.014.

[64] L. Masdrag, X. Courtois, F. Can, S. Royer, E. Rohart, G. Blanchard, P. Marecot, D. Duprez, Understanding the role of C3H6, CO and H2 on efficiency and selectivity of NOx storage reduction (NSR) process, Catal. Today. 189 (2012) 70–76. doi:10.1016/j.cattod.2012.03.053.

[65] I. Nova, L. Lietti, P. Forzatti, Mechanistic aspects of the reduction of stored NOx over Pt-Ba/Al2O3 lean NOx trap systems, Catal. Today. 136 (2008) 128–135. doi:10.1016/j.cattod.2008.01.006.

[66] K. Leistner, A. Nicolle, P. Da Costa, Modelling the kinetics of NO oxidation and NO x storage over platinum, ceria and ceria zirconia, Appl. Catal. B Environ. 111–112 (2012) 415–423. doi:10.1016/j.apcatb.2011.10.029.

[67] D.H. Kim, K. Mudiyanselage, J. Szanyi, J.H. Kwak, H. Zhu, C.H.F. Peden, Effect of K loadings on nitrate formation/decomposition and on NOx storage performance of K-based NOx storage-reduction catalysts, Appl. Catal. B Environ. 142–143 (2013) 472–478. doi:10.1016/j.apcatb.2013.05.063.

[68] Y. Liu, M. Meng, Z. qiang Zou, X. gang Li, Y. qing Zha, In situ DRIFTS investigation on the NOx storage mechanisms over Pt/K/TiO2-ZrO2 catalyst, Catal. Commun. 10 (2008) 173–177. doi:10.1016/j.catcom.2008.08.014.

[69] S.S. Chaugule, A. Yezerets, N.W. Currier, F.H. Ribeiro, W.N. Delgass, “Fast” NOx storage on Pt/BaO/γ-Al2O3 Lean NOx Traps with NO2 + O2 and NO + O2: Effects of Pt, Ba loading, Catal. Today. 151 (2010) 291–303. doi:10.1016/j.cattod.2010.02.024.

[70] P. Kočí, M. Schejbal, J. Trdlička, T. Gregor, M. Kubíček, M. Marek, Transient behaviour of catalytic monolith with NOx storage capacity, Catal. Today. 119 (2007) 64–72. doi:10.1016/j.cattod.2006.08.014.

[71] B.R. Kromer, L. Cao, L. Cumaranatunge, S.S. Mulla, J.L. Ratts, A. Yezerets, N.W. Currier, F.H. Ribeiro, W.N. Delgass, J.M. Caruthers, Modeling of NO oxidation and NOx storage on Pt/BaO/Al2O3 NOx traps, Catal. Today. 136 (2008) 93–103. doi:10.1016/j.cattod.2008.02.013.

[72] A. Güthenke, D. Chatterjee, M. Weibel, N. Waldbüßer, P. Kočí, M. Marek, M. Kubíček, Development and application of a model for a NOx storage and reduction catalyst, Chem. Eng. Sci. 62 (2007) 5357–5363. doi:10.1016/j.ces.2007.01.049.

[73] P. Kočí, F. Plát, J. Štěpánek, M. Kubíček, M. Marek, Dynamics and selectivity of NOx reduction in NOx storage catalytic monolith, Catal. Today. 137 (2008) 253–260. doi:10.1016/j.cattod.2007.11.023.

[74] P. Kočí, F. Plát, J. Štěpánek, Š. Bártová, M. Marek, M. Kubíček, V. Schmeißer, D. Chatterjee, M. Weibel, Global kinetic model for the regeneration of NOx storage catalyst with CO, H2 and C3H6 in the presence of CO2 and H2O, Catal. Today. 147 (2009). doi:10.1016/j.cattod.2009.07.036.

[75] P. Kočí, Š. Bártová, D. Mráček, M. Marek, J.S. Choi, M.Y. Kim, J.A. Pihl, W.P. Partridge, Effective model for prediction of N2O and NH3 formation during the regeneration of NO x storage catalyst, Top. Catal. 56 (2013) 118–124. doi:10.1007/s11244-013-9939-y.

[76] S. Shwan, W. Partridge, J.S. Choi, L. Olsson, Kinetic modeling of NOx storage and reduction using spatially resolved MS measurements, Appl. Catal. B Environ. 147 (2014) 1028–1041. doi:10.1016/j.apcatb.2013.10.023.

[77] J.A. Pihl, J.A. Lewis, T.J. Toops, J.E. Parks, Lean NOx trap chemistry under lean-gasoline exhaust conditions: Impact of high NOx concentrations and high temperature, Top. Catal. 56 (2013) 89–93. doi:10.1007/s11244-013-9934-3.

[78] CLEERS Protocols, (2005). http://www.cleers.org/protocols/1113847174LNTmap_7_18_05.pdf.

[79] M. AL-Harbi, W.S. Epling, The effects of regeneration-phase CO and/or H2 amount on the performance of a NOX storage/reduction catalyst, Appl. Catal. B Environ. 89 (2009) 315–325. doi:10.1016/j.apcatb.2008.12.010.

[80] G. Jacobs, L. Williams, U. Graham, G.A. Thomas, D.E. Sparks, B.H. Davis, Low temperature water-gas shift: In situ DRIFTS-reaction study of ceria surface area on the evolution of formates on Pt/CeO2 fuel processing catalysts for fuel cell applications, Appl. Catal. A Gen. 252 (2003) 107–118.

doi:10.1016/S0926-860X(03)00410-1.

[81] A.A.. Phatak, N.. Koryabkina, S.. Rai, J.L.. Ratts, W.. Ruettinger, R.J.. Farrauto, G.E.. Blau, W.N.. Delgass, F.H.. Ribeiro, Kinetics of the water-gas shift reaction on Pt catalysts supported on alumina and ceria, Catal. Today. 123 (2007) 224–234. doi:10.1016/j.cattod.2007.02.031.

[82] X. Courtois, N. Bion, P. Mar??cot, D. Duprez, Chapter 8 The role of cerium-based oxides used as oxygen storage materials in DeNOx catalysis, Stud. Surf. Sci. Catal. 171 (2007) 235–259. doi:10.1016/S0167-2991(07)80209-6.

[83] Z. shun Zhang, B. bing Chen, X. kui Wang, L. Xu, C. Au, C. Shi, M. Crocker, NOx storage and reduction properties of model manganese-based lean NOx trap catalysts, Appl. Catal. B Environ. 165 (2015) 232–244. doi:10.1016/j.apcatb.2014.10.001.

[84] J. Koop, O. Deutschmann, Modeling and Simulation of NOx Abatement with Storage / Reduction Catalysts for Lean Burn and Diesel Engines, SAE Tech. Pap. 2007-01-1142. 2007 (2007).

[85] H. Abdulhamid, E. Fridell, M. Skoglundh, The reduction phase in NOx storage catalysis: Effect of type of precious metal and reducing agent, Appl. Catal. B Environ. 62 (2006) 319–328. doi:10.1016/j.apcatb.2005.08.014.

[86] J.A. Pihl, J.E. Parks II, C.S. Daw, T.W. Root, Product Selectivity During Regeneration of Lean NOx Trap Catalysts, Sae Tech. Pap. Ser. 2006-01–34 (2006) 776–790. doi:10.4271/2006-01-3441.

[87] W.S. Epling, A. Yezerets, N.W. Currier, The effects of regeneration conditions on NOX and NH3 release from NOX storage/reduction catalysts, Appl. Catal. B Environ. 74 (2007) 117–129. doi:10.1016/j.apcatb.2007.02.003.

[88] J.-S. Choi, W.P. Partridge, J.A. Pihl, M.-Y. Kim, P. Kočí, C.S. Daw, Spatiotemporal distribution of NOx storage and impact on NH3 and N2O selectivities during lean/rich cycling of a Ba-based lean NOx trap catalyst, Catal. Today. 184 (2012) 20–26. doi:10.1016/j.cattod.2011.11.007.

[89] A. Lindholm, N.W. Currier, J. Li, A. Yezerets, L. Olsson, Detailed kinetic modeling of NOx storage and reduction with hydrogen as the reducing agent and in the presence of CO2 and H2O over a Pt/Ba/Al catalyst, J. Catal. 258 (2008) 273–288. doi:10.1016/j.jcat.2008.06.022.

[90] H. Abdulhamid, E. Fridell, M. Skoglundh, Influence of the type of reducing agent (H2, CO, C3H6 and C3H8) on the reduction of stored NOX in a

Pt/BaO/Al2O3 model catalyst, Top. Catal. 30/31 (2004) 161–168. doi:10.1023/B:TOCA.0000029745.87107.b8.

[91] S. Matsumoto, Y. Ikeda, H. Suzuki, M. Ogai, N. Miyoshi, NO(x) storage-reduction catalyst for automotive exhaust with improved tolerance against sulfur poisoning, Appl. Catal. B Environ. 25 (2000) 115–124. doi:10.1016/S0926-3373(99)00124-1.

[92] S. Poulston, R.R. Rajaram, Regeneration of NOx trap catalysts, Catal. Today. 81 (2003) 603–610. doi:10.1016/S0920-5861(03)00158-5.

[93] A. Lindholm, N.W. Currier, E. Fridell, A. Yezerets, L. Olsson, NOx storage and reduction over Pt based catalysts with hydrogen as the reducing agent. Influence of H2O and CO2, Appl. Catal. B Environ. 75 (2007) 78–87. doi:10.1016/j.apcatb.2007.03.008.

[94] U. Elizundia, D. Duraiswami, B. Pereda-Ayo, R. López-Fonseca, J.R. González-Velasco, Controlling the selectivity to N2O over Pt/Ba/Al 2O3 NOX storage/reduction catalysts, Catal. Today. 176 (2011) 324–327. doi:10.1016/j.cattod.2010.11.075.

[95] F. Duprat, Light-off curve of catalytic reaction and kinetics, Chem. Eng. Sci. 57 (2002) 901–911. doi:10.1016/S0009-2509(01)00409-2.

[96] P. Kočí, V. Novák, F. Štěpánek, M. Marek, M. Kubíček, Multi-scale modelling of reaction and transport in porous catalysts, Chem. Eng. Sci. 65 (2010) 412–419. doi:10.1016/j.ces.2009.06.068.

[97] Z. Liu, S.I. Woo, Recent Advances in Catalytic DeNOx Science and Technology, Catal. Rev. Sci. Eng. 48 (2006) 43–89. doi:10.1080/01614940500439891.

[98] K. Ramanathan, C.S. Sharma, Kinetic parameters estimation for three way catalyst modeling, Ind. Eng. Chem. Res. 50 (2011) 9960–9979. doi:10.1021/ie200726j.

[99] S.R. Katare, P.M. Laing, Hydrogen in Diesel Exhaust: Effect on Diesel Oxidation Catalyst Flow Reactor Experiments and Model Predictions, 2 (2009) 605–611. doi:10.4271/2009-01-1268.

[100] C. Millet, S. Benramdhane, A 3WCC Global Kinetic Model : A Calibration Method Using Laboratory Scale and Engine Test Bench Experiments, 2008 (2008).

[101] F. Lafossas, Y. Matsuda, A. Mohammadi, A. Morishima, M. Inoue, M.

Kalogirou, G. Koltsakis, Z. Samaras, Calibration and Validation of a Diesel Oxidation Catalyst Model : from Synthetic Gas Testing to Driving Cycle Applications, Sae Tech. Pap. Ser. 4 (2011). doi:10.4271/2011-01-1244.

[102] C.S. Sampara, E.J. Bissett, M. Chmielewski, D. Assanis, Global kinetics for platinum diesel oxidation catalysts, Ind. Eng. Chem. Res. 46 (2007) 7993–8003. doi:10.1021/ie070642w.

[103] D. Kryl, P. Koc, Kryl - Catalytic converters for automobile diesel engines with adsorption of hydrocarbons on zeolites.pdf, (2005) 9524–9534.

[104] J. Sjöblom, Bridging the gap between lab scale and full scale catalysis experimentation, Top. Catal. 56 (2013) 287–292. doi:10.1007/s11244-013-9968-6.

[105] G.D. Wehinger, T. Eppinger, M. Kraume, Fluidic effects on kinetic parameter estimation in lab-scale catalysis testing - A critical evaluation based on computational fluid dynamics, Chem. Eng. Sci. 111 (2014) 220–230. doi:10.1016/j.ces.2014.02.025.

[106] T. Gu, V. Balakotaiah, Impact of heat and mass dispersion and thermal effects on the scale-up of monolith reactors, Chem. Eng. J. 284 (2016) 513–535. doi:10.1016/j.cej.2015.09.005.

[107] L. Junhui, N.W. Currier, A. Yezerets, H. Chen, H. Hess, S. Mulla, Oxidation State Optimization for Maximum Efficiency of NOx Adsorber Catalysts, in: 16th Directions in Engine-Efficiency and Emissions Research (DEER) Conference, Detroit, MI, 2010.

[108] DieselNet, Worldwide Harmonized Light Vehicles Test Cycle (WLTC), (2017). https://www.dieselnet.com/.

[109] A. Bourane, D. Bianchi, Oxidation of CO on a Pt/Al2O3 catalyst: From the surface elementary steps to light-off tests: V. Experimental and kinetic model for light-off tests in excess of O2, J. Catal. 222 (2004) 499–510. doi:10.1016/j.jcat.2003.11.019.

[110] M. Khosravi, A. Abedi, R.E. Hayes, W.S. Epling, M. Votsmeier, Kinetic modelling of Pt and Pt:Pd diesel oxidation catalysts, Appl. Catal. B Environ. 154–155 (2014) 16–26. doi:10.1016/j.apcatb.2014.02.001.

[111] C.H. Kim, M. Schmid, S.J. Schmieg, J. Tan, W. Li, The Effect of Pt-Pd Ratio on Oxidation Catalysts Under Simulated Diesel Exhaust, Sae. 2011-01–11 (2011) 1–10. doi:10.4271/2011-01-1134.

[112] H. Sharma, A. Mhadeshwar, A detailed microkinetic model for diesel engine emissions oxidation on platinum based diesel oxidation catalysts (DOC), Appl. Catal. B Environ. 127 (2012) 190–204. doi:10.1016/j.apcatb.2012.08.021.

[113] K. Hauff, U. Tuttlies, G. Eigenberger, U. Nieken, A global description of DOC kinetics for catalysts with different platinum loadings and aging status, Appl. Catal. B Environ. 100 (2010) 10–18. doi:10.1016/j.apcatb.2010.07.036.

[114] K.C. Premchand, J.H. Johnson, S.-L. Yang, A.P. Triana, K.J. Baumgard, A Study of the Filtration and Oxidation Characteristics of a Diesel Oxidation Catalyst and a Catalyzed Particulate Filter, in: SAE Tech. Pap., SAE International, 2007. doi:10.4271/2007-01-1123.

[115] D. Chatterjee, T. Burkhardt, T. Rappe, A. Güthenke, M. Weibel, Numerical Simulation of DOC+DPF+SCR systems:DOC Influence on SCR Performance, SAE Int. J. Fuels Lubr. 1 (2008) 440–451. doi:10.4271/2008-01-0867.

[116] S. Salomons, M. Votsmeier, R.E. Hayes, A. Drochner, H. Vogel, J. Gieshof, CO and H2 oxidation on a platinum monolith diesel oxidation catalyst, Catal. Today. 117 (2006) 491–497. doi:10.1016/j.cattod.2006.06.001.

[117] T.C. Watling, M. Ahmadinejad, M. Tutuianu, Å. Johansson, M. a. J. Paterson, Development and Validation of a Pt-Pd Diesel Oxidation Catalyst Model, SAE Int. J. Engines. 5 (2012-01 (2012) 24. doi:10.4271/2012-01-1286.

[118] DieselNet, Diesel Oxidation Catalyst, (2012). https://www.dieselnet.com/.